Parent population of flat-spectrum radio-loud narrow-line Seyfert 1 galaxies

Direttore della scuola: Ch.mo Prof. Giampaolo Piotto
Supervisore: Dr. Stefano Ciroi
Co-supervisore: Dr. Luigi Foschini

Dottorando: Marco Berton

Sommario

Questa tesi si propone di svelare la natura della cosiddetta popolazione madre delle galassie narrow-line Seyfert 1 radio brillanti a spettro piatto (F-NLS1). Queste sorgenti sono una sottoclasse di nuclei galattici attivi che di recente è stata identificata come la terza classe degli AGN con emissione di raggi γ. Esse ospitano un getto relativistico diretto verso l'osservatore. Lo scopo era di comprendere come questi oggetti appaiono quando osservati da una diversa inclinazione. Per studiare ciò ho costruito quattro campioni di candidati, ossia narrow-line Seyfert 1 radio brillanti a spettro ripido (S-NLS1), narrow-line Seyfert 1 radio quiete (RQNLS1), radio-galassie ospitate in una galassia a disco (disk RG) e oggetti compatti a spettro ripido con spettro ad alta eccitazione (CSS/HERG). Per ciascun campione ho calcolato la massa del buco nero e il rapporto di Eddington, per confrontarlo con i valori già noti delle F-NLS1. Ho studiato le differenze fra le narrow-line region delle RQNLS1 e delle NLS1 radio brillanti, per trovare segni di interazione con il getto relativistico. Infine, ho costruito la prima funzione di luminosità delle F-NLS1, per confrontarla con quella dei CSS/HERG. Ho concluso che una F-NLS1, quando osservata ad angoli via via crescenti, appare prima come una S-NLS1 e dopodiché come una disk RG. Entrambe queste sorgenti possono essere incluse nella più vasta classe dei CSS/HERG. In generale quindi le F-NLS1 sono dei CSS/HERG osservate all'interno del loro getto relativistico.

Abstract

The aim of this thesis is to unveil the nature of the so-called parent population of flat-spectrum radio-loud narrow-line Seyfert 1 galaxies (F-NLS1s). These sources are a subclass of active galactic nuclei which was recently identified as the third class of γ-ray emitting AGN. They likely harbor a relativistic jet directed toward the observer. The aim was to understand how do they appear when observed under a different inclination. To study their parent population I built four samples of parent candidates, that is steep-spectrum narrow-line Seyfert 1 galaxies (S-NLS1s), radio-quiet narrow-line Seyfert 1 (RQNLS1s), disk-hosted radio-galaxies (disk RGs) and finally compact steep-spectrum sources with high excitation spectrum (CSS/HERGs). For each sample I calculated the black hole mass and Eddington ratio, to compare them with those of F-NLS1s. I studied the differences in the narrow-line region of RQNLS1s and radio-loud NLS1s, to find traces of interactions with a relativistic jet. Finally, I built the first luminosity function of F-NLS1s, to compare it with that of CSS/HERGs. I concluded that a F-NLS1, when observed at large angles, appears as a S-NLS1s and later as a disk RGs. Both of them can be included in the larger group of CSS/HERGs. In general then F-NLS1s are CSS/HERGs observed inside their relativistic jet.

ii

Contents

List of Figures

List of Tables

Chapter 1

Introduction

1.1 Brief history of Active Galactic Nuclei

With the term active galactic nucleus (AGN) we usually refer to an anomalous emission of energy occurring in the central cubic parsec of a galaxy, that cannot be attributed simply to the stars, gas and dust composing the galaxy itself. This energy can be emitted at all frequencies, and forms the characteristic spectral energy distribution (SED) of the AGN, which is completely different from that of a regular galaxy.

Historically some AGN, as M87 or M104, were already included in the Messier catalogue in 1774, but they were not recognized as a different class of sources until the spectroscopic work by Carl Keenan Seyfert (1943). He performed a study on a sample of six galaxies selected in the Mount Wilson Observatory Catalogue. When compared with regular galaxies, they presented a few peculiarities. All but one were spiral galaxies, their central regions showed a luminosity much higher than the average and, moreover, their spectra showed broad emission lines and also forbidden lines quite similar to those of a HII region. This was quite an unusual feature for a galaxy. These sources later became a separate class of objects, characterized by the semi-stellar nucleus and emission-lines, called **Seyfert galaxies**. A new survey, performed at the Byurakan Observatory in Armenia by Markarian (1963), led to the discovery of many more Seyfert galaxies, and to a new classification system based on the presence of emission lines. Later on they were divided into two distinct classes, Seyfert 1 (Sy1) and Seyfert 2 (Sy2, Khachikian & Weedman 1974). In Sy1 permitted lines are very broad, corresponding to velocities up to 10^4 km s^{-1}, while the forbidden lines correspond to lower velocities, $\leq 10^3$ km s^{-1}. In Sy2, instead, both permitted and forbidden lines have the same width of $\lesssim 10^3$ km s^{-1}. The high velocities measured in Sy1 revealed that, if the material in the nucleus is gravitationally bound, then the central mass must be huge, around 10^8 M$_\odot$ (Woltjer 1959).

With radio surveys in the late 1950s it was discovered that most of the counterpart of radio sources were nearby galaxies, but in a few cases it seemed that counterparts were point-like objects. Their spectra showed strong emission lines, whose wavelengths did not match those of any known element. Marteen Schmidt was the first to understand that those misterious lines were just the Balmer series lines strongly redshifted. This was the first milestone in the understanding of **quasars** (Schmidt 1963). Soon the first hypotheses involving black holes appeared independently in two works by Salpeter (1964) and Zel'dovich (1964), and became widely accepted. The only way to explain such luminosities, that span in a range between $10^{40}-10^{48}$ erg s^{-1}, was the accretion of matter onto a supermassive black hole

(SMBH, Lynden-Bell 1969). In the following years the distinction between Seyfert galaxies and quasars became less and less important. Nowadays it is widely accepted that they are the same phenomenon, but a totally arbitrary distinction remains, with quasars having by definition $M_{B-band} > -23$ (Schmidt & Green 1983). Despite the general understanding that the mechanism of energy production in AGN is the same everywhere, they are usually divided in several classes of objects, according to their observational properties. The next section will provide a short summary of the main AGN categories.

1.2 Zoology

1.2.1 Seyfert galaxies

Seyfert galaxies are the first discovered class of AGN. As previously mentioned, they are separated from regular galaxies by their bright point-like nucleus and by the broad emission lines in their optical spectrum. The latter is given by the overlap of the host galaxy spectrum, where absorption lines are produced, and the nuclear spectrum, where instead the emission lines are originated. The nuclear spectrum is usually less dominant in Seyfert 2 galaxies, while it is much more intense in Seyfert 1 spectra, as shown in Fig. 1.1. Sy1 also exhibit a strong continuum that is interpreted as the non-thermal emission from the accretion disk that surrounds the central black hole. Tipically Seyfert galaxies are weak radio emitters, but in some cases they show a non-thermal component in their SED, which is due to synchrotron emission from a radio jet.

Also some non-active galaxies show a spectrum that is quite similar to that of a Seyfert galaxy. The high ionization lines, such as [O III] $\lambda\lambda 4959,5007$ are in fact also produced in the H II regions, where the gas is ionized by hot and young OB stars. The different ionization mechanism can be revealed using the diagnostic diagrams developed by Veilleux & Osterbrock (1987). The ratios of [N II] ($\lambda\lambda 6548,6583$)/Hα and [O III]($\lambda\lambda 4959,5007$)/Hβ and the lines profiles in fact are different when the ionizing photons come from a non-thermal source, such as an accretion disk, or a black body. Seyfert galaxies have on average both ratios higher than the H II regions, and a larger FWHM of the lines.

The optical spectrum is not the only way to discern between Seyfert 1 and 2, because a similar difference is present in X-rays. Such distinction here is based on the intrinsic absorption measured in the soft band, typically below 5 keV. Such absorption indicates the presence of gas nearby the central engine of the AGN, and it is measured in terms of hydrogen column density. Seyfert 1 tipically show a low absorption, and a power-law spectrum with a soft excess, although some exceptions are known. Conversely, those with high hydrogen column density N_H are optically classified as Seyfert 2, again with known exceptions. From this point of view Seyfert 2 can exhibit very different N_H, and they are often separated into two classes. If $N_H \leq 10^{24}$ cm^{-2}, the X-rays above few keV are not absorbed and the source is called Compton-thin since they are optically thin to the photons Compton up-scattered. For $N_H \geq 1.5 \times 10^{24}$ cm^{-2} only photons above 10-100 keV can go through the absorber, and the source is Compton-thick. When the density is above 10^{25} cm^{-2}, only photons reflected or scattered by warm material are observed. Another feature often visible in X-rays is the Fe K$-\alpha$ line around 6.4 keV. This line is originated by fluorescence, and it can be alternatively narrow or broad, depending on its origin. The iron K$-\alpha$ line is on average stronger in Sy2 than in Sy1 because of the blocking, in the former, of the direct X-ray emission, so that scattered hard X-rays can be observed. This reduces the continuum emission and hence increases the
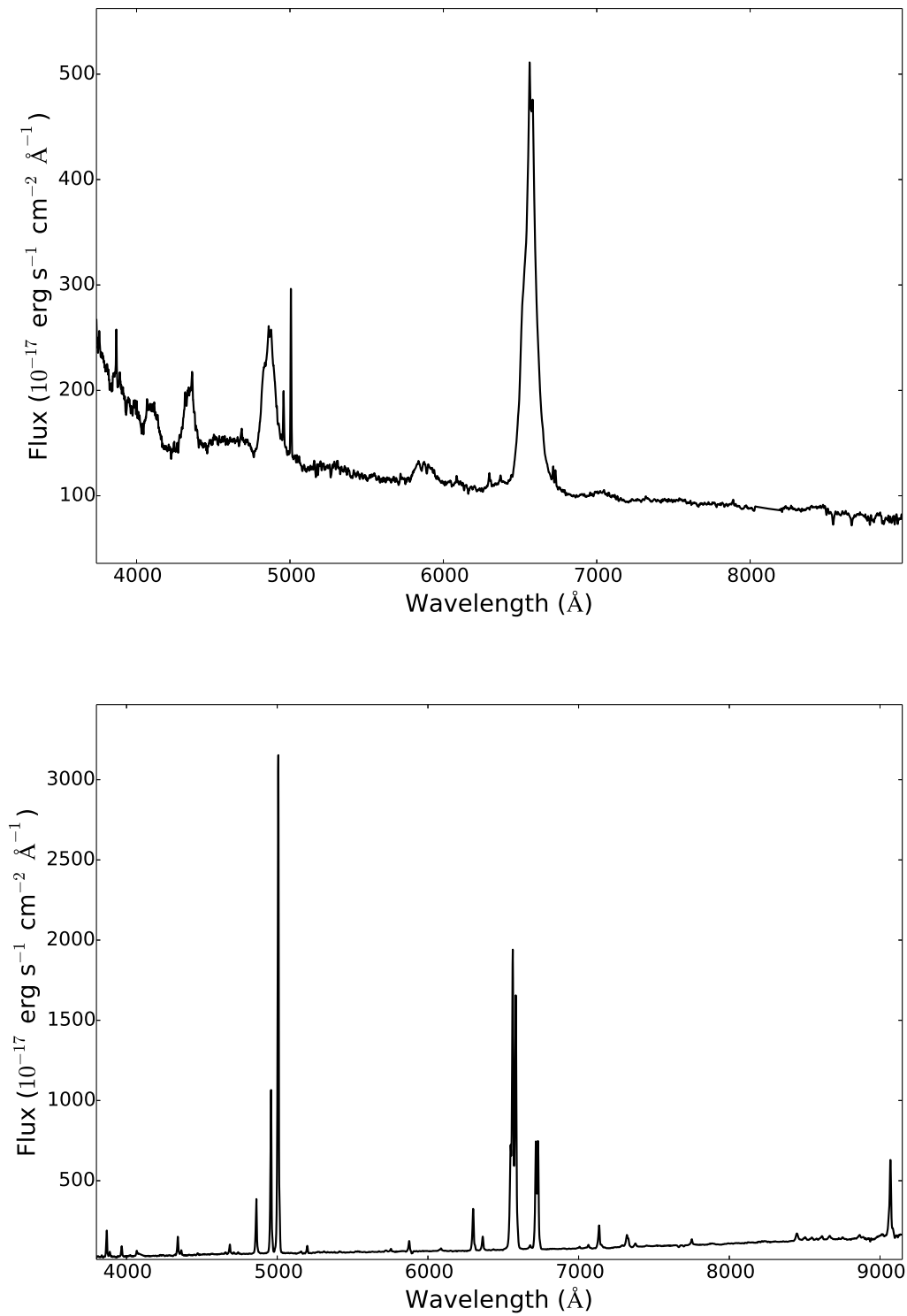
Figure 1.1 Spectra of two examples of Seyfert galaxies. **Top panel:** a Seyfert 1 spectrum. **Bottom panel:** a Seyfert 2 spectrum. Both spectra are derived from the SDSS archive.

equivalent width of the line (van Paradijs & Bleeker 1999).

The transition between type 1 and 2 is obviously shallower than this, with many intermediate objects that lie in between the two principal classes. Some Seyfert galaxies in fact show properties that are somewhat in the middle between type 1 and 2. It was Donald Osterbrock (1981) who introduced the notation Seyfert 1.5, 1.8 and 1.9 to discern between them by the optical spectrum. These intermediate Seyferts in fact usually have two clearly separated components in their permitted lines, a narrow one and a broad one, and they are classified according to the ratio of the components. For instance in those cases where the broad and narrow components of the lines are comparable, a Seyfert is classified as 1.5.

Anyway it must be underlined that the classification of AGN as type 1, 2 or intermediate is not written on the stone. AGN are in fact evolving structure that can change, sometimes quickly. Not only the permitted lines are subject to several variations that occurs on timescales of days, and that are induced by changes in the ionizing continuum, but the whole spectrum can be radically different when observed at different epochs. Several examples can be found, the most recent being the cases of Mrk 590, first classified as a classical Seyfert 1 and now showing a Seyfert 2 spectrum (Denney et al. 2014), and of NGC 2617, that exhibited a dramatically rapid change in its spectrum going from Seyfert 2 to Seyfert 1 (Shappee et al. 2013).

1.2.2   LINERs

Low-Ionization Nuclear Emission-line Regions (LINERs) are the link that connects the H II regions with Seyfert galaxies, and by far the less luminous class of AGN. First identified by Heckman (1980), they show forbidden lines with similar width to those of Seyfert 2, but the ratios between them are quite different. In particular, the ratio of [O III]/Hβ is lower than in Seyfert 2, while the [N II] $\lambda\lambda$6548,6583 is much stronger with respect to Hα. In general all the low-ionization emission lines, [O II] λ3727, [S II] $\lambda\lambda$6716,6731, together with [N II], are stronger, while high ionization lines as [O III] are weaker. LINERs are not universally considered AGN. Some authors think that their emission is due to accretion onto a supermassive black hole (e.g. Heckman 1980), while others assert that the emission is generated by violent star formation activity at high metal abundance (e.g. Terlevich & Melnick 1985). This debate upon their nature was born because LINERs have a weak nuclear emission if compared to the surrounding starlight, the opposite of Seyferts where the nucleus is brighter than the underlying galaxy. Nevertheless also radio and X-ray can be used as discriminator: these sources show indeed a compact flat spectrum radio core and a point-like X-ray emission that H II regions do not have.

1.2.3   Quasars

First discovered in the late 1950s, they are virtually point-like sources at high redshift and the most luminous subclass of AGN. Nowadays these are between the most distant objects ever detected, with the furthest being at $z = 7.085$ (Mortlock et al. 2011). Many of them show in their SED the so-called Big Blue Bump, a feature of thermal origin that is extended from the optical to the X-ray. As previously mentioned, quasars and Seyfert galaxies are the same phenomenon, but despite this until the early 1990s no type 2 quasars were found. The reason of this strange missing was that type 2 AGN have no strong emission lines that can be easily detected at high z, and they also do not exhibit any strong radio emission. Their

discovery occurred in fact neither in optical nor in radio, but instead in the X-rays. Both Seyfert and quasars are strong X-rays emitters, and the launch of the first dedicated satellites (e.g. *ROSAT*, *Chandra*) allowed to detect a large number of type 2 quasars. Right now it is known that the number of type 1 and 2 quasars in the local universe is pretty much the same.

Quasars are often divided in two distinct classes, radio-quiet and radio-loud, according to their so-called **radio-loudness** parameter. Kellermann et al. (1989) defined it as

$$RL = \frac{F_{B-band}}{F_{5\,GHz}} \; ; \tag{1.1}$$

where F_{B-band} is the optical B-band density flux and $F_{5\,GHz}$ is the radio density flux at 5 GHz. This parameter provides an estimate of the amount of non-thermal radiation in the SED, particularly synchrotron, with respect to the optical radiation. If RL > 10 the object is defined as radio-loud, otherwise it is defined as radio-quiet. In this work I also discern between radio-quiet sources, that have at least a measured radio flux at any frequency, and radio-silent objects, that have no detectable radio emission at all. It is really important to remember that radio-loudness is strongly dependent on the way the radio and optical fluxes are measured. If RL is evaluated for a whole galaxy, the optical flux will include also the host galaxy contribution. If instead only the nuclear region is considered, F_{B-band} will be lower and, as a consequence, RL will be higher. Also the radio flux can vary for the very same reason. As proved by Ho & Peng (2001) a radio-quiet source can indeed move to the radio-loud domain when only its nuclear contribution is evaluated. Despite this, the radio-loudness parameter is often useful to separate sources with or without a relativistic jet. The latter is in fact the strongest contributor to radio-emission with its synchrotron radiation (see Sect. 1.4.5). Around 90% of quasars are radio-quiet, and are tipically known as QSOs. They exhibit just a weak sychrotron radio-emission possibly due to supernova remnants or to some really weak jet activity (Ulvestad et al. 2005).

1.2.4 Blazars

Blazars are a particular class of quasars, and they are among the most luminous sources in the Universe. Apart from supernovae and gamma-ray bursts, blazars are also the most violently variable objects known in the Universe in terms of luminosity. Their timescales are of the order of hours, and sometimes even minutes, and in many of them, particularly at radio-frequencies, superluminal motions are observed.

Blazars are divided into two classes, BL Lacertae Objects (BL Lac) and Flat Spectrum Radio Quasars (FSRQs), according to their optical spectral line properties. If the equivalent width of the lines is lower than 5 Å, the source is a BL Lac, otherwise it is a FSRQ. Therefore the optical spectrum of a BL Lac is virtually a featureless power-law continuum, with almost no absorption or emission lines at all. For this reason, it is really difficult to obtain a spectroscopic redshift determination of a BL Lac (Fig. 1.2 bottom panel). FSRQs on the contrary have strong emission lines overlapped with the same power-law continuum. Since these sources are really bright, blazars can be seen at very high redshift. It is not uncommon in the optical spectra of FSRQs to observe the Lyα line − whose restframe wavelenght is 1216 Å, in the UV − and the strong absorptions of the Lyman forest, due to the neutral hydrogen located between the blazar and the Earth (Fig. 1.2 top panel).

Another interesting aspect regarding blazars is their SED. Hystorically FSRQs were radio-selected blazars, while BL Lacs were tipically X-ray selected sources. This division was later
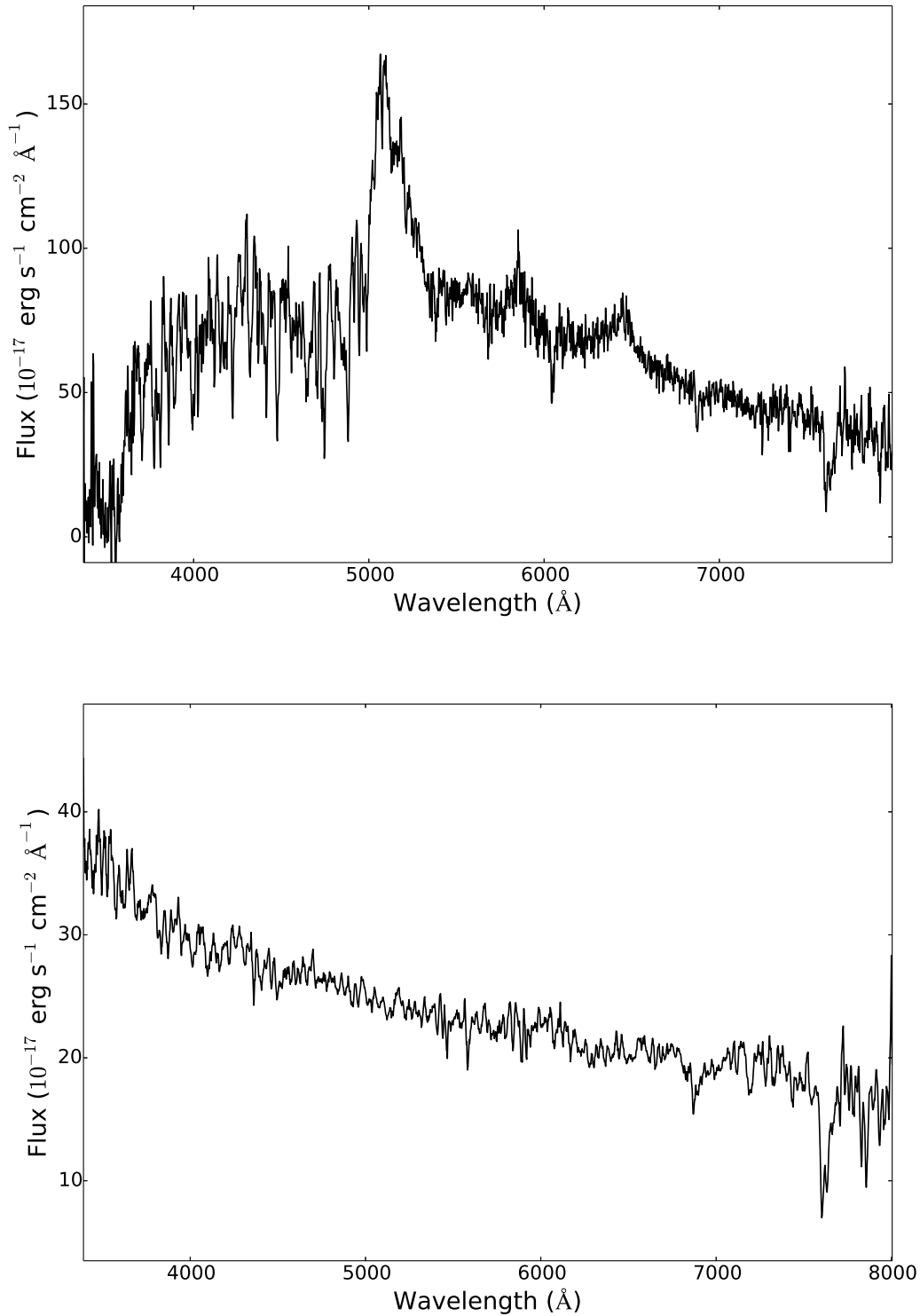
Figure 1.2 **Top panel:** Spectrum of a flat-spectrum radio-quasar. The prominent line is Lyα, with the strong absorptions of the Lyα forest at lower wavelengths. **Bottom panel:** Spectrum of a BL Lacertae object. No strong absorption or emission lines are present. Those at high wavelengths are telluric absorptions of the Earth atmosphere. Both spectra were obtained with the Asiago 1.22m telescope.

overtook by the work by Padovani & Giommi (1995), but it was due to the blazars SED shape. The first component of their SED to be discovered was the low frequency part. Going from lower to higher frequencies the SED rises until it reaches a peak, and then it decreases. The frequency of this first peak increases going from FSRQs to BL Lacs, that indeed are peaked in X-rays. Because of this shape, until the launch of the first γ-ray satellite COS-B, blazars were not expected to be strong high energy emitters. Nevertheless the truth is that the high energy sky, at least outside of the Galactic plane, is dominated by blazars. The SED in fact is double-peaked, with the second peak in the γ-ray domain. After the discovery of this second peak, Sambruna et al. (1996) and later Fossati et al. (1998) divided blazars in different classes according to their bolometric luminosity, and found that they form a sequence going from low to high power in the $\log \nu - \log \nu L_\nu$ plane. High power sources, as FSRQ, have both peaks at relatively low frequencies, while low power sources, as BL Lacs, have both the peaks at higher frequencies.

1.2.5 Radio galaxies

Together with blazars, the strongest radio sources in the extragalactic sky are radio galaxies. These sources usually show a radio-core, a collimated jet, and finally radio-lobes. The radio-core is an unresolved structure that typically overlaps with the optical nucleus. The jet instead is defined as a feature that is at least four times as long as it is wide, and that is separable at high resolution from other extended structures (Bridle 1986). The radio-lobe is finally an extended structure that shows inner substructures, and with a well defined edge beyond which the intensity rapidly falls to zero (Leahy 1993)[1]. Jets can be both one-sided, when only one radio-lobe is visible, or two-sided, when the structure is roughly symmetric and two lobes are visible. The lobes have variable size, but they are typically around 10-100 kpc, and often larger than their host galaxy. Sometimes the lobes show structures known as hot spots: they are the brightest feature in the lobes, with a high surface brightness and a small size.

A key characteristic of radio-galaxies is their radio spectrum: while in blazars the spectrum is almost flat, in radio-galaxies the core has still a flat-spectrum, while the radio-lobes have a steep-spectrum. Hot spots, when present, show a flat-spectrum more similar to that of the core. These objects are often classified depending on the radio luminosity and morphological properties in two classes, known as Fanaroff-Riley classes (Fanaroff & Riley 1974). If the separation between the regions of highest brightness is less than half the total size of the source, the latter is a Fanaroff-Riley Class I (FRI). If instead the separation between the brightest regions is larger than half the size, the source is a Fanaroff-Riley Class II (FRII). In other words, when the brightness is more concentrated in the core and the edges of the radio-lobes are not luminous, the galaxy is a FRI. These objects usually do not show hot spots in their lobes, and their luminosity is lower than a threshold fixed at 10^{32} erg s^{-1} Hz^{-1} sr^{-1} at a frequency of 175 MHz. When the luminosity is above this value, the lobes are usually quite bright, and the source is classified as a FRII radio-galaxy. Usually FRIs are located at low redshift and in clusters, while FRIIs are definitely less common and usually have higher z. It is not clear if this is a selection effect or a real physical difference. Anyway, also the optical spectra are different because in FRII sources there are high ionization lines that are not visible in FRI, that have instead a more LINER-like spectrum.

---

[1] In the following with the term *jet* I refer to the whole structure, core + jet + lobe, unless otherwise specified.

Radio-galaxies are thought to live for a few $\sim 10^7$ years, and their age can be evaluated using the curvature of their radio spectra, caused by the energy loss of the high-energy electrons (Rawlings & Saunders 1991). There are two particular sub-classes of radio-galaxies that reveal a relatively young age, the **Gigahertz-Peaked Spectrum** (GPS) and **Compact Steep Spectrum** (CSS) objects. They are compact and powerful radio-sources with peaks in their radio-spectra, at 1 GHz for GPS and 100 MHz for CSS. These peaks are usually interpreted as synchrotron self-absorption, and they are connected to the linear scale of the source. While GPS sources are entirely confined within the so-called narrow-line region (NLR), CSS are always inside their host galaxy, and they usually exhibit double jets often distorted, a hint of interaction with the galactic medium. Finally, their number density scales with their linear sizes, and this is consistent with an expansion at constant velocity of jets. All these properties seem to reveal that these sources are young and still evolving sources, possibly connected with FRI objects.

1.3   Radiation processes

To understand the observational panorama previously illustrated, it is necessary to introduce a few physical mechanisms that are typically observed in AGN. They are briefly summarized in this section. This treatise is based on the dedicated chapters in few textbooks: Peterson (1997), Boettcher et al. (2012) and Beckmann & Shrader (2012).

1.3.1   Relativistic effects

To distinguish between the macroscopic motion of an emission region and the microscopic motion of a single particle, a few definitions are necessary. Regarding the single particle, its Lorentz factor is defined as

$$\gamma = \frac{1}{\sqrt{1 - \beta^2}} \ , \tag{1.2}$$

where β is the normalized speed of the particle

$$\beta = \frac{v}{c} \quad .$$

For the motion of a whole emission region, instead, the bulk Lorentz factor Γ must be considered. In a particle gas, two different kinds of motion are present. The first one is the simple thermal motion of the particles, and the second is the bulk motion of the gas in a particular direction. These two motions are not necessarily connected. A gas of relativistic particles has a large thermal motion, but in some reference frames it can have a null bulk velocity. Conversely, a bulk motion of the gas at relativistic speed does not necessarily imply a hot gas. In general, the relativistic bulk motion of the gas is driven by the bulk Lorentz factor Γ. The normalized speed of the gas is then

$$\beta_\Gamma = \sqrt{1 - \frac{1}{\Gamma^2}} \ . \tag{1.3}$$

From now on I will use the label "em" to indicate the rest frame of the emission region, and the "ob" label to indicate the stationary observer's frame.

Beaming

Using the Lorentz-invariant scalar products, we can derive the relation that links the energy of a photon E^{em} in its emission rest frame with the observed energy E^{ob} of the same photon observed in our stationary reference system. If θ is the angle between the direction of the emission region motion and the direction of the emitted photon, it is

$$E^{ob} = \frac{E^{em}}{\Gamma(1 - \beta_\Gamma \cos\theta^{ob})} \equiv \delta E^{em} \tag{1.4}$$

It is straightforward that if the emission region is moving toward us along the line of sight, and the photon is emitted in the opposite direction, $\theta^{ob} = \pi$, and $\cos\theta^{ob} = -1$, the observed radiation is decreased since in relativistic motion $\Gamma \gg 1$, and

$$\delta = \frac{1}{\Gamma(1 + \beta_\Gamma)} \approx \frac{1}{2\Gamma} \ll 1 \; .$$

On the contrary, if $\cos\theta^{ob} = 1$, it is

$$\delta = \frac{1}{\Gamma(1 - \beta_\Gamma)} = (1 + \beta_\Gamma)\Gamma \approx 2\Gamma \gg 1 \; .$$

Therefore, a photon emitted along the direction of the motion will be boosted to higher energies. If we derive the same relation in the emission reference frame it must be equivalent to Eqn. 1.4, and therefore we can derive the following relation between θ^{ob} and θ^{em}:

$$\cos\theta^{ob} = \frac{\cos\theta^{em} + \beta_\Gamma}{1 + \beta_\Gamma \cos\theta^{em}} \tag{1.5}$$

When a photon is emitted for $\theta^{em} = \pi/2$, it will be received with an angle $\theta^{ob} = \cos^{-1}(\beta_\Gamma)$. If Γ is large, $\beta_\Gamma \sim 1$, and the angle is small. Therefore using a Taylor expansion we get

$$\beta_\Gamma \sim 1 - \frac{1}{2\Gamma^2}$$

$$\cos\theta^{ob} \sim 1 - \frac{(\theta^{ob})^2}{2} \; .$$

These equations show that photons emitted at $\pi/2$ in the emission frame are received at an angle $\theta^{ob} \sim 1/\Gamma$. If the emission region produces photons isotropically, all those emitted at an angle smaller than $\pi/2$ will be beamed into a cone of opening angle $1/\Gamma$. This phenomenon is known as **relativistic beaming**. It is quite easy to calculate, given a bulk Lorentz factor, the ratio between the sources observed within the beaming cone n_b and those with different inclination n_u. Assuming that the sources are distributed with random inclinations in the sky, this ratio will be proportional to the ratio between the solid angles. If the aperture angle of the cone is α, it is

$$\frac{n_b}{n_u} = \frac{1 - \cos\alpha}{\cos\alpha} \; . \tag{1.6}$$

Since $\alpha \sim 1/\Gamma$, with a Taylor series expansion the equation becomes:

$$\frac{n_b}{n_u} \sim \frac{1 - (1 - \alpha^2/2)}{1 - \alpha^2/2} = \frac{\alpha^2/2}{1 - \alpha^2/2} \sim \frac{1/2\Gamma^2}{1 - (1/2\Gamma^2)} \; .$$

If Γ is large, the second term in the denominator is negligible, and Eq. 1.6 becomes

$$n_u \sim 2\Gamma^2 n_b \; , \tag{1.7}$$

meaning that the number of unbeamed sources is $2\Gamma^2$ times the number of beamed sources. This equation will have strong implications in the following chapters.

Timescales

A direct consequence of Eqn. 1.4 is the shortening of the timescales. Since $E_{ph} = h\nu$, and being ν the inverse of a time interval, we find

$$\frac{\Delta t^{ob}}{\Delta t^{em}} = \frac{\nu^{em}}{\nu^{ob}} = \frac{E^{em}}{E^{ob}} = \frac{1}{\delta} \tag{1.8}$$

Therefore the larger is the Doppler factor of the emission region, the shorter the observed timescales get.

Superluminal motion

The superluminal motion observed in AGN is based on a geometrical effect, and the first model able to explain this phenomenon was derived by Rees (1966). If an emission region moves at relativistic speed $v = c\beta_\Gamma$ forming a small angle θ with the line of sight, we can derive that the apparent motion across the sky which the observer measures is given by

$$v_\perp^{ob} = \frac{v^{em}\sin\theta}{1 - \beta_\Gamma\cos\theta} \; . \tag{1.9}$$

For a given Γ there is a particular angle, called the *superluminal angle* that maximizes the apparent speed, and it is

$$\cos\theta_{sl} = \beta_\Gamma \; .$$

The maximum speed at this angle is

$$v_{sl} = c\sqrt{\Gamma^2 - 1} \; ,$$

and it is clear that in any relativistic case the maximum speed is well above the speed of light. It is worth noting that the measurement of this apparent speed provides a lower limit to the bulk Lorentz factor, and at the same time it fixes an upper limit for the viewing angle.

1.3.2   Synchrotron radiation

Synchrotron radiation occurs when relativistic electrons are accelerated by a magnetic field. Each electron changes direction because of the magnetic force perpendicular to the motion direction, and therefore follows an helical trajectory. The energy of the emitted photons is a function of the electron energy, of the magnetic field strength and of the angle between the electron path and the field. The luminosity emitted from a single particle is given by

$$L_e = \frac{4}{3}\sigma_T\frac{v^2}{c}\gamma^2\frac{B^2}{8\pi} \simeq 1.1 \times 10^{-15}\mathrm{cm^3s^{-1}}\gamma^2 B^2 \; , \tag{1.10}$$

where σ_T is the Thomson cross-section for the electron, and the numerical approximation is valid in the relativistic case where $v \sim c$. In this relativistic case, the emitted photons are

beamed. Therefore, as the particles describe a helical motion, the observer will receive a pulse only when the beaming cone is pointed toward the line of sight. Synchrotron radiation from a single electron is then a pulsed emission. When instead a large number of charged particles are emitting, the resulting spectrum will be a function of the particles energy distribution.

In the astrophysical case, the most common energy distribution of electrons is a power-law. Assuming such electrons distribution with index s, the emitted intensity in an optically thin regime is

$$I_\nu \mathrm{d}\nu \propto \nu^{\frac{1-s}{2}} \mathrm{d}\nu \ .$$

The spectrum is therefore also a power-law of index $\alpha = (1-s)/2$, with a typical astrophysical value of -0.7. This is not true if the gas is optically thick, as at low radio frequencies. In this spectral domain the photons emitted become self-absorbed, and the spectrum follows a power-law with spectral index $+2.5$. At higher frequencies, which in blazars can span even to the X-rays domain, there is an exponential cut-off due to radiation losses. The synchrotron is a mechanism of cooling: high energy electrons rapidly cool down by emitting synchrotron photons, so their energy distibution is cutted-off at high energies. If new high energy electrons are not created, the gas cools down and the cut-off in both the energy distribution and in the spectrum moves toward lower energies. This cut-off can indeed reveal the age of the sources.

A way to discern between thermal emission and synchrotron is that the latter is linearly polarized. For a single electron the polarization can reach 69%, but when a gas of electrons is emitting, the polarization degree has a much lower value, with an upper limit of the order of 10-20% in the case of blazars.

1.3.3 Compton scattering

Inverse Compton

The so-called **inverse Compton (IC)** is the opposite of regular Compton scattering. The latter occurs when a high energy photon interacts with a slowly moving electron, transferring its energy to the particle and decreasing its frequency. When the interaction is between a photon and a highly relativistic electron, the particle transfers its energy to the photon, boosting the photon to higher frequencies. This process, unlike synchrotron, does not generate photons, but simply increases their energy. The equation governing this energy loss of the particle is

$$L = \frac{4}{3}\sigma_T c \beta^2 \gamma^2 U_{rad} \ , \tag{1.11}$$

where U_{rad} is the energy density of the photon field. It is evident that Eqn. 1.11 has the same structure of Eqn. 1.10, except that the magnetic energy density is replaced by the photon energy density. Another analogy with synchrotron is that the spectral shape of the emitted radiation depends on the electron energy distribution.

Self-synchrotron Compton

In the AGN case, the relativistic electrons that transfer their energy to the photon fields are the same producing the synchrotron photons at radio frequency. In the self-synchrotron Compton (SSC) case, the scattered photons are those produced via synchrotron in the same region where the IC occurs. Therefore the spectral shape of IC is the same of synchrotron, but it is shifted at higher energy. A typical radio photon via IC is moved to the X-rays domain,

while an optical photon becomes a γ-ray photon. SSC typically takes place in blazars (and particularly in BL Lacs) relativistic jets, and it is the mechanism that allow the γ-ray emission in these sources.

External Compton

Another phenomenon often occurring in blazars is external Compton (EC). The seed photons in this case are not those produced via synchrotron in the relativistic jet, but instead those produced by some external sources, such as the accretion disk, the Broad Line Region (BLR, see 1.4.3) or the molecular torus. As in SSC, these external photons interact with the relativistic particles in the jet, and they are shifted at higher frequencies. Since the EC photons are produced in lower photon density regions, they have a lower probability to interact with other high energy photons and decaying into an electron-positron couple. Therefore the EC shows less absorptions than the SSC spectrum. This is anyway not true in FSRQs: in these particular sources the photon density in the BLR is very high, therefore absorptions features are often observed in the γ-ray spectrum (Poutanen & Stern 2010).

Compton catastrophe

The intensity of a radio source can be determined by measuring the flux and the angular size of the source. An equivalent temperature can be evaluated, assuming that the source is emitting like a blackbody. If F_ν is the observed flux at wavelength λ and θ the angular size of the source,

$$I_\nu = \frac{F_\nu}{\pi \theta^2} = B_\nu = \frac{2kT_B}{\lambda^2} \tag{1.12}$$

where the second equation uses the Rayleigh-Jeans approximation for low frequencies. T_B is called *brightness temperature*. It has the same behaviour of the synchrotron spectrum, peaking roughly at the same frequency, and decreasing at higher frequencies as $\nu^{-(s+3)/2}$ where, as in the previous Sections, s is the electrons distribution spectral index. Kellermann & Pauliny-Toth (1969) found that the ratio between the inverse Compton luminosity and the synchrotron luminosity is

$$\frac{L_{IC}}{L_s} = \left(\frac{T_B}{T_0}\right)^5 \left[1 + \left(\frac{T_B}{T_0}\right)^5\right] , \tag{1.13}$$

where T_B is the brightness temperature at the synchrotron peak frequency, and $T_0 \sim 10^{12}$K is a threshold temperature. The consequence of this equation is that in the case of $T_B > T_0$ the inverse Compton luminosity rapidly rises: a brightness temperature of 10^{13}K implies an X-ray flux much higher than what is observed (see Tsang & Kirk 2007, and references therein). This phenomenon is called the *Compton catastrophe*. Nevertheless, several sources show a brightness temperature above this threshold, particularly blazars. The most widely accepted solution to this problem is the relativistic beaming: the synchrotron luminosity is enhanced by the beaming, and therefore the brightness temperature appears to be higher than what it actually is. For this reason, an high T_B is considered as a sign of the presence of relativistic beaming and, by consequence, of a relativistic jet.

1.4 Physical structure

In this section I will describe each one of the main components of an AGN, and I will finally describe the Unified Model. As in the previous section, the treatise is mainly based on the textbooks by Peterson (1997), Beckmann & Shrader (2012) and Boettcher et al. (2012).

1.4.1 Black Hole

The AGN is located in the central cubic parsec of a host galaxy. The so-called *central engine* is a supermassive rotating black hole surrounded by an accretion disk and a hot corona. This region is the place of origin of thermal radiation, which is particularly evident in the UV-visible part of the spectrum. This structure appears as a high bump in the $\log \nu - \log (\nu F_\nu)$ plot: for this reason it is known as big blue bump.

The black hole hypothesis is necessary to explain the incredible amount of mass concentrated in the small volume of the nucleus. Such a high density cannot be explained in any other reasonable way. This statement has currently been proved, for example, by the presence of OH or H_2O masers produced in the vicinity of the core. Using the VLBI resolution, these emissions allow to map the gravitational potential of the inner core of some AGN, and therefore to measure the mass producing that potential. There are other ways to do this, such as the reverberation mapping technique (Peterson 2008), or the so-called M-σ relation (Ferrarese & Merritt 2000), which links the SMBH mass with the stellar velocity dispersion in the galactic bulge. All these methods lead to a mass distribution between 10^6 and 10^{10} $M_\odot$ confined in a region not bigger than the Solar System. Therefore, the only possible explanation is the presence of the SMBH. Right now this hypothesis is widely accepted, and it is also clear that almost every galaxy has a SMBH in its nucleus, including SgrA* in the Milky Way. For this reason, it is plausible that the vast majority of galaxies in the Universe can go through one or more phases of AGN any time there is enough gas in the nuclear region to *switch on* the central engine. Even the Milky Way might have been an active galaxy, as suggested by the presence of two polar outflows known as *Fermi bubbles*, which are possibly due to a former episode of nuclear activity (Su et al. 2010).

Anyway, the real central engine is not the black hole itself, because such an object cannot - by definition - emit any kind of radiation (with the only notable exception of the Hawking radiation, which is anyway negligible in every astrophysical case). The true source of energy is instead the infall of matter onto the SMBH, which can convert the gravitational potential energy in electromagnetic radiation. This conversion occurs in an accretion disk by means of magnetohydrodinamical instability, that can generate turbulent motions inside the disk itself (Balbus & Hawley 1991).

1.4.2 Accretion

The most simple mechanism to explain the accretion onto the black hole is under the assumption of spherical symmetry, a process known as *Bondi flow*. In this mechanism the gas does not escape the gravitational well of the black hole even if it has enough energy to do this, because of a purely radial motion. When a deviation from this regime occurs, a part of the gas will flow away from the source, giving origin to important outflows. Nevertheless, such accretion requires that the radial symmetry extends to infinity, and this is clearly impossible. Moreover, the gas will always has angular momentum, which heavily influences the flow. In

particular, its result will be a rotating disk or torus that will accrete onto the black hole only if it loses some of its angular momentum. A way to do this is the **thin α-disk** model Shakura & Sunyaev (1973). The momentum in fact can be redistributed between different regions of the disk via some sort of friction. The inner regions lose angular momentum and move inward, while the outer parts gain the momentum and move outwards. This redistribution of the plasma produces a flattened structure, the thin disk. The cooling of the disk is very efficient until it remains thin, in other words until its thickness is much lower than the radius, otherwise it forms a thick disk or a torus.

An important issue is which kind of friction can effectively transport the angular momentum. For typical condition of disks, the molecular viscosity ν_m derived from the collisions between gas particles, is too low to actually contribute in any way. Defined the Keplerian velocity at radius r as $v_k = \sqrt{GM/r}$, the corresponding Reynolds number $\mathcal{R}_m = v_k r/\nu_m$ is larger than the critical value of 10^3 above which most flows become turbulent. This suggested that the dynamics of disks is driven by turbulent viscosity, $\nu_t \sim \lambda_t v_t$, where λ_t is the largest length scale of the turbulent motion and v_t the corresponding velocity. Of course λ_t must be lower than the disk thickness H and the upper limit for v_t is the sound speed, therefore:

$$\nu_t = \alpha v_s H \ ,$$

where $\alpha \leq 1$ is the parameter giving the name to the disk model. Nevertheless, it is usually accepted that Keplerian disks are actually stable, independently from their Reynolds number, since they satisfy the Rayleigh stability criterion, which requires the angular momentum to increase outwards. This problem has been solved by Balbus & Hawley (1991): in fact the presence of a magnetic field can induce the formation of turbulence because of magnetorotational instability. Therefore the driving mechanism of turbulence in AGN is the magnetic viscosity. Observations in typical astrophysical conditions also allowed to determine that the best fit of $\alpha \approx 0.1 - 0.4$ (King et al. 2007).

The inner edge of the disk is the radius of the innermost stable circular orbit (ISCO) around the black hole r_{ISCO}. Beyond this limit, the gas radially infalls because of the black hole potential. The ISCO radius strongly depends on the metric adopted to study the black hole, and it changes radically between rotating and non-rotating objects. Rotating black holes (Kerr BH) are probably quite common in the astrophysical cases, and they are characterized not only by their mass, as in the non-rotating Schwarzschild case, but also by their dimensionless spin, defined as

$$a = \frac{Jc}{GM^2} \ ,$$

where J is the angular momentum of the BH. In all Kerr black holes the value for a cannot be larger than 0.998 (Thorne 1974), and this case corresponds to the maximally rotating black hole. The radius of the ISCO depends on the spin: for a Schwarzschild BH, where $a = 0$, the r_{ISCO} is equal to 6 times the gravitational radius r_g. In the maximally rotating BH, with $a = 0.998$, the disk can co-rotate with the black hole, giving $r_{ISCO} = 1.24 \ r_g$, or counter-rotate, and $r_{ISCO} = 9r_g$. Both the co-rotating and counter-rotating solutions for the thin disk appear to be stable. Another interesting property of Kerr black holes is that they show a static limit at which a particle counter-rotating with the black hole appear to be static for a distant observer. Inside this limit, the spacetime is dragged in the direction of the black hole rotation, and any counter-rotating orbit, to be stable, would require a velocity larger than c: therefore only co-rotating orbits are allowed in this region. This is the *frame-dragging* or

Lense-Thirring effect. The region where the frame-dragging occurs is known as **ergosphere**, and it allows the existance of test particle trajectories with negative energy. As shown in Sect. 1.4.5, the ergosphere plays a key role in the jet-launching model.

In thin disks the binding energy of the ISCO increases with a, where the highest possible value is reached for $a = 0.998$ and a co-rotating orbit, and it gives the maximum possible value of radiated energy per unit accreted rest mass. If instead a part of this energy is advected onto the black hole along with the flow, and hence lost, the bolometric luminosity of the disk will be lower. The accretion luminosity can therefore be expressed as a function of the η parameter, known as the *energy efficiency parameter*, that is defined as the radiated energy per unit accreted rest mass:

$$L_{acc} = \eta \dot{M} c^2 . \tag{1.14}$$

Of course η must be lower or equal to the binding energy. The nuclear burning inside stars has an efficiency of ~ 0.007. In the case of a black hole, the binding energy highest value is instead ~ 0.42, and the typical value for η is around ~ 0.1, meaning that on average 10% of the accreting mass is converted into energy. The accretion process onto a black hole is in conclusion way more efficient than the thermonuclear reactions.

This huge amount of energy irradiated by the disk generates a powerful radiation pressure on the inflowing gas, and the most important interaction between photons and the ionized hydrogen of plasma is Thomson scattering. The number of scattering is a function of the accretion luminosity, and therefore there is a critical value for L where the radiation pressure equals the gravitational force of the black hole:

$$L_{Edd} = \frac{4\pi G m_p c M}{\sigma_T} \sim 1.3 \times 10^{38} \left(\frac{M}{M_\odot} \right) \text{ erg s}^{-1} , \tag{1.15}$$

where m_p is the proton mass, and σ_T the Thomson scattering cross-section. This luminosity threshold is known as **Eddington limit**. Putting together Eqn. 1.14 and 1.15, it corresponds to the Eddington mass accretion rate, given by:

$$\dot{M}_{Edd} = \frac{4\pi G m_p M}{c \sigma_T \eta} \sim 2.3 \left(\frac{\eta}{0.1} \right)^{-1} \left(\frac{M}{10^8 M_\odot} \right) \text{ M}_\odot \text{ year}^{-1} .$$

This accretion rate provides also a timescale for the lifetime of AGN, of the order of 10^8 years. If the luminosity exceeds this limit, the pressure radiation will blow away a part of the inflowing gas and hence reduce the accretion to a sub-Eddington rate. This is likely to happen in quasars, that have a bolometric luminosity comparable to their Eddington luminosity and therefore have black holes accreting at a rate close to the Eddington limit. A useful tool to test the accretion rate is the **Eddington ratio**, defined as

$$\epsilon = \frac{L_{bol}}{L_{Edd}} \tag{1.16}$$

where L_{bol} is the bolometric luminosity. This ratio is often used to evaluate how fastly a source is accreting with respect to the Eddington luminosity. Of course this cannot be directly related with the real mass accretion unless the η parameter is known.

It can be shown that where the pressure of thin disks becomes dominated by radiation, when $\dot{M} > \dot{M}_{Edd}$ the thin disk model is not valid anymore in the surroundings of the black hole, where the disk height is increased and the structure is torus-shaped. The cooling

becomes then inefficient and the advection of radiation toward the inner regions is favored inside the so-called *trapping radius*. This leads to a decrease of the energy efficiency of the accretion, and hence increases the critical value of $\dot{M}_{Edd}$. The radiation emitted by this torus is highly anisotropic, and is largely directed along the polar axis of the disk. Therefore, even in super-Eddington luminosities the radiation pressure will likely not affect the flow of gas in the equatorial plane. These flows with inefficient cooling are called **Advection Dominated Accretion Flow** (ADAF), and they are quite common in many astrophysical black holes. They in fact occur also when the mass accretion rate is well below $\dot{M}_{Edd}$ and the gas opacity is very low. When this happens the density of the disk is too low to efficiently cool down the gas. The gas energy, as in the Bondi case, is then enough to escape the potential well of the black hole. Strong winds can easily be launched from the disk surface, removing angular momentum, mass and energy from the ADAF disk. For this reason, ADAF are often associated with the formation of jets.

The outer edge of the disk is determined by the equality between the black hole gravity and the self-gravitation of the disk itself. When the latter starts to dominate, the gas splits into fragments and the viscosity that drives it inside the disk plunges near zero. Therefore there must be a way to move the gas from the outer regions of the galaxy to the disk in absence of viscosity. The biggest problem is again the angular momentum that the gas must lose to reach the inner core. A possible mechanism is the gravitational torque, which can occur only in presence of a nonaxisymmetric gravitational potential. This means that bar-driven fueling of the nucleus in spiral galaxies is an efficient way to feed the AGN, and studies show that this may be the reason of the high Eddington ratio in some AGN (Crenshaw et al. 2003). The fact that not all barred spiral galaxies have an AGN in their core suggests that nonaxisymmetric potential must be present on all scales from kpc to pc (Shlosman et al. 1989). Other suggested mechanisms are merging, which could drive a large quantity of gas in the nucleus during the interaction, and also mass loss from stars, which could be important in those elliptical galaxies where the interstellar gas is quite rare.

1.4.3   Broad Line Region

The main observational difference between type 1 and 2 AGN is the width of the strong, permitted lines that characterize the active galaxies spectra. It is commonly believed that these lines are originated in the gas surrounding the black hole and the accretion disk, moving in the so-called **Broad Line Region** (BLR). The most prominent of these permitted lines are that of the hydrogen Balmer series, such as Hα $\lambda6563$, Hβ $\lambda4861$, Hγ $\lambda4340$, the Lyα line $\lambda1216$, and also MgII $\lambda2798$. These lines have a typical FWHM of ~5000 km s^{-1}, but they can span between 500 to over 10^4 km s^{-1}. It often occurs that in the same spectrum different emission lines have different widths, and for example the HeII $\lambda4686$ and HeI $\lambda5876$ are often broader than the Balmer lines. Another important optical spectral feature originating in the BLR is the Fe II multiplets, a blend of many weak broad lines located between 4000 and 5500 Å.

Comparing the BLR spectrum with that of other ionized gases, the inferred temperature is of the order of 10^4 K. At such a temperature the velocity dispersion for the gas due to the thermal motion is just 10 km s^{-1}, and this cannot explain the observed width of the lines, that must therefore be interpreted as the motion of the gas around the central engine. The lower limit to the density can be derived by the absence of broad [O III] forbidden lines in the spectra, which sets the threshold to the value of $\sim10^8$ cm^{-3}. Typical values for the BLR are

indeed higher, tipically between 10^9 and 10^{11} cm^{-3}, and they are a function of the distance from the nucleus.

The BLR is not a uniform region filled with gas, otherwise it would be optically thick (Ferland & Mushotzky 1982), but it is instead organized in clouds (Nenkova et al. 2008a,b) which rapidly rotate around the black hole, giving origin to the Doppler broadening of the permitted lines. These clouds are in local thermodynamical equilibrium: the photoionization induced by the ionizing photons coming from the central engine has the same rate as the recombination. The inner part of the clouds that faces the central engine has a higher ionization degree with respect to the back side; therefore, the high ionization lines, as He II, He I, C IV, must come from this inner part, while the low ionization ones, such as Mg II, Ca II, Fe II, are produced in the back of the clouds. Assuming that the clouds do not shadow each other, and that they are distributed in a spherical shell around the nucleus, it can be derived that their total number is around $\sim 5 \times 10^4$, and their radius is lower than $\sim$400 R$_\odot$ (Peterson 1997). It is anyway worth noting that not all authors agree on the spherical symmetry of the BLR. Several studies in fact hypothize that the latter could have a disk-like shape, or at least a flattened component (Wills & Browne 1986; Vestergaard et al. 2000; Decarli et al. 2008; Pozo Nuñez et al. 2013).

The size of the BLR can be inferred in many ways, for example from the rotation velocity assuming a virialized system. A quite powerful technique is the *reverberation mapping* (Lyutyi & Cherepashchuk 1972; Cherepashchuk & Lyutyi 1973; Blandford & McKee 1982), that is based on the assumption that the size and structure of the BLR can be inferred by observing the response of emission lines to variations of the continuum. A basic assumption here is that the observed continuum is the same ionizing continuum that induces the lines response, and that the dynamical timescale of the BLR is larger than the light travel-time. This response is delayed because of the finite speed of light, and therefore occurs after the light travel-time across the BLR. Since time-lag changes for different lines, the reverberation mapping demonstrates that the BLR is radially stratified as mentioned before.

1.4.4 Narrow Line Region

The optical spectra of AGN always display many forbidden lines with different ionization degrees, usually the most prominent being the [O III] doublet $\lambda\lambda$4959, 5007, [O II] λ3727, [O I] λ6300, [N II] $\lambda\lambda$6548, 6583, [S II] $\lambda\lambda$6716, 6731, and many others. The main condition to produce the forbidden atomic lines is low density, a condition that in the BLR is never satisfied. Therefore, they cannot be produced nearby the central engine, but at larger distances. The narrowness of these lines, with typical velocities between 200 and 900 km s^{-1}, also reveal physical conditions completely different from those of the BLR: all these properties can be explained with the presence of the **Narrow Line Region** (NLR).

This region is located further from the black hole than the BLR: the forbidden lines flux is in fact almost constant over long period of times, indicating that the NLR is quite large, with an order of magnitude of 10^2 pc, but its size also depends from the luminosity of the most prominent lines (Bennert et al. 2004). As said before, the density to produce a forbidden line must be low, between 10^{3-5} cm^{-3}, and this gives a total NLR mass estimated around 10^6 M$_\odot$. As in the BLR, the gas has not a uniform distribution, but is instead organized in small clumps and stratified, with the high ionization lines coming from the innermost regions (Osterbrock 1991). At the same time it appears that also the density increases toward the center, and this could be a sign that the inner part of the NLR is likely directly connected

with the BLR, without any physical boundary between them.

The NLR dynamics does not appear to be correlated with the gravitational potential of the central engine, as in the BLR. The widths of the forbidden lines in fact seem to be affected by the gravitational field of the stars (Nelson & Whittle 1996), and this is particularly true for the low ionization lines, as [O II], [N II] and [S II] that are produced at large distances from the nucleus. Since the NLR structure is often spatially resolved, it is possible to observe the distribution of the clumps with increasing distance from the center. Its geometry is not spherical, but instead axisymmetric, and the axis coincides with the radio axis in radio-loud sources with extended emission. In particular, the presence of jets seems to influence the shape of the spectral line, because the gas is accelerated by the radio-emitting plasma. This increases the forbidden lines widths (Peterson 1997). In the case of jet-dominated AGN, instead, this is not true anymore, since a strong jet component reduces the lines equivalent width (Foschini 2012a).

Images obtained with [O III] $\lambda5007$ filters often reveal the presence of the ionization cones (Pogge 1988), a symmetric biconical structure with quite sharp and linear edges. The apex of these cones are often not visible because of strong obscuration in the center. The lines ratios reveal that inside the cones the ionization is produced directly from the AGN continuum, while beyond their edge the ionization is mostly due to stars. The presence of these cones reveals that the ionizing continuum is strongly anisotropic, at least on kpc scales. A possible explanation to this phenomenon is the presence of the molecular torus, that is predicted in the Unified Model (see Sect. 1.4.6). This torus in fact obscures the ionizing photons emitted on the equatorial plane of the accretion disk, allowing only the radiation perpendicular to the disk to escape. In this way, only the clouds located above and below the disk are ionized by the AGN continuum, producing the cones. It is finally important to notice that the ionization cones, in a disk galaxy, are not necessarily perpendicular to the galactic plane. If this were true, in a face-on host-galaxy we would always see the nuclear regions, because the line of sight would be free from obscuration, and the source would always appear as a type-1 AGN. But since the cones symmetry axis is not aligned with that of the galaxy, the AGN type is not dependent from the host galaxy inclination, even if in general type-1 sources tend to avoid edge-on hosts (LaMassa et al. 2012).

1.4.5   Jets

As previously mentioned, another fundamental feature in many AGN is the jet. They are powerful relativistic collimated outflows of matter and energy usually thought to be fueled by an accretion process onto a relativistic object, the SMBH in the AGN case. Jets are not observed only in AGN, but also in less energetic sources such as X-ray binaries or proto-stars, and they are also associated with γ-ray Bursts, so to a massive star collapse. They are able to transport energy and momentum from the central source to distant locations, where they are dissipated in hot spots and in radio lobes surrounding the jet and the spots themselves. The scale of these objects can be very different: in AGN, a jet can be even a few Mpc long, but jets extended just for few parsecs are quite common in many objects (see Hada et al. 2013, for the nuclear jet in the low luminosity AGN M104).

The first discovery of such structures is due to Curtis (1918), when the jet from the elliptical galaxy M87 was observed in optical. At that time, nobody understood its nature, but later observations, carried on with more powerful tools such as the Very Long Baseline Interferometer (VLBI), showed that compact high-temperature radio-cores were present in

AGN, and also that many galaxies have a complex extended radio emission made of the nuclear component, jets, the hot spots and radio lobes.

The primary emission mechanism of jets is synchrotron radiation, with a typical radio spectral index of -0.7. The other fundamental emission is the inverse Compton scattering, that is largely dominant at high energies and that produces the second peak in blazars SED. The composition of jets is still under debate, but the hypothesis usually accepted is the leptonic model (Mastichiadis & Kirk 1997), even if the hadronic model can not be completely ruled out. The double-peaked SED might be interpreted in terms of cooling of the relativistic electrons (Ghisellini et al. 1998). A strong jet in fact has a higher photon density, and the electrons are cooled more efficiently by the photon field they produce via synchrotron. The latter will therefore show a cutoff at lower frequencies, and the inverse Compton branch will dominate the SED. For low power jets, there are few photons in the surrounding medium, and the electrons cooling occurs only via SSC. The SSC photons reach very high energies, so both the peaks will be shifted at larger frequencies. These two different mechanisms are usually associated with the two classical flavors of blazars: FSRQs have high-power jets, while BL Lacs are instead low-power sources.

What is probably the most challenging problem in understanding jets is their formation. A fundamental role is played by magnetic fields: by means of their interaction with the ionized matter they lead to the collimation of the bipolar outflows along the rotation axis of the black hole. A widely diffuse theory regarding jets formation is the Blandford-Znajek (BZ) mechanism (Blandford & Znajek 1977), that involves the properties of rotating Kerr black holes. As previously mentioned, in these objects there is a region, the ergosphere, where orbits corresponding to negative total energy exist. The ergosphere is located outside the event horizon, and it has a radius of $2r_g$ on the equatorial plane, while its radius in the polar direction is the same as the event horizon. Based on the ergosphere properties, Penrose (1969) built an ideal mechanism to extract energy from the black hole. If a particle enters the ergosphere, and then inside of it splits in two, the trajectory can lead one half on a negative energy orbit and then inside the black hole with energy $E_1 < 0$. The other particle goes back to infinity with energy $E_2 > 0$. The energy conservation requires that the initial energy $E_{in} = E_1 + E_2$, therefore $E_2 > E_{in}$. Even if some rest-mass energy has been lost in the black hole, there is a net gain of energy at infinity. This energy gain is at expenses of the rotational energy of the black hole, which slows down when the negative energy particle is captured. Nevertheless, this thought experiment is of little practical interest because the breakdown of the two particles inside the ergosphere must happen with relative velocity of at least $c/2$. It is hard to imagine an astrophysical process that produces such large relative velocities.

Nevertheless, an electromagnetic equivalent of the Penrose mechanism exists: it is the BZ mechanism. The rotating black hole, if placed in a magnetic field generated by a disk, can induce the generation of plasma outflows and inflows. The inflow, as in the Penrose mechanism, carries into the black hole a negative electromagnetic energy, that corresponds to an extraction of energy and to an outflow, that is the jet. This can happen only if a magnetic field is threaded to the black hole, allowing a magnetic extraction of the spin energy.

Another possibility is that the jet is powered by the production of gravitational energy in the accreting disk. The spinning disk can push away the outer layers of plasma, forming a strong centrifugally driven wind. The latter, at large distances from the black hole, is collimated by the magnetic field into a pair of anti-parallel jets moving perpendicular to the disk. In the inner region, a magnetically dominated corona is formed, and this can extract angular momentum from the disk allowing matter to be accreted. The latter is the so-called

Blandford-Payne (BP) mechanism, that works only in presence of a strong disk (Blandford & Payne 1982). It is worth noting that the BP mechanism requires that a particular criterium is met. The magnetic field in the accretion disk has tipically two components. The first one is produced by the circular electric current produced by the disk rotation, and is toroidally shaped. The other is instead produced by plasma flares, and is poloidal. The BP is active only if the angle between the poloidal component of the magnetic field and the accretion disk is less than $60°$. In this case, at large distances from the disk, the toroidal component of the magnetic field becomes important and collimates the outflow into a pair of anti-parallel jets moving perpendicular to the disk. Even when the jet is not fully developed, a jet-base can be formed by the disk. The jet-base is a pressure-driven structure that, through a longitudinal pressure gradient, leads to a modest but significant acceleration perpendicularly to the disk, with a typical $\gamma = 2 - 3$. This model is enough to explain the non-thermal emission in some low-power AGN, but of course is too weak for typical radio-loud sources (Falcke & Biermann 1999).

Unlike the BP mechanism, the BZ can work also on weak disks − the original paper of Blandford & Znajek did not even consider any disk − and in particular in presence of ADAF. For this reason, the BZ mechanism is usually associated with BL Lacs, while BP can occur in FSRQ. Anyhow several hybrid models of jet launching were developed during the years (see Foschini 2011a, and references therein), and a definitive answer has yet to come.

Since jets are highly relativistic features, they display all those relativistic effects described in the previous sections. Blazars, in particular, are thought to be AGN in which the line of sight falls inside the jet, or within few degrees from the jet axis. The relativistic effects allow to explain the superluminal motion, the dramatically short variability timescales, and also the high luminosity observed in these sources. The synchrotron photons of the jet form the power-law continuum extended from radio to X-rays. In FSRQs a strong disk generates a large number of ionizing photons, which later form the emission lines observed in the optical domain. In BL Lacs, instead, the disk is weaker, and it can produce only very weak emission lines (Stocke et al. 2011). The weak absorption lines coming from the host galaxy are instead often observed, always overlapped with the synchrotron power-law. But how does a blazar appear when observed at larger inclinations? The latter is known as the **parent population** problem. Because of the relativistic beaming, there should be $2\Gamma^2$ sources in which the line of sight falls outside of the jet. The answer to this problem comes from the Unified Model.

1.4.6   Unified Model

In the Unified Model, the different classes of AGN are substantially the same phenomenon observed under different viewing conditions. The unification of AGN is based on the presence of the so-called molecular torus, a dusty structure that surrounds the central engine and the BLR on the same plane of the accretion disk. This torus can absorb the radiation, and therefore hide the innermost regions. If this is true, the light of the BLR can escape in a direction where the absorbing material is not present, and then it can be scattered toward the observer by the medium. Therefore the BLR must be visible in polarized light. The first hint of the torus presence was suggested by Keel (1980), and a strong proof of this was given by Antonucci & Miller (1985), who observed the broad Balmer lines in polarized light coming from the Seyfert 2 galaxy NGC 1068. At the same time the narrow forbidden lines show almost no polarization at all, pointing out that the NLR is observed directly. It is anyway important to underline that not all Seyfert 2 appear to have a BLR in polarized light: these
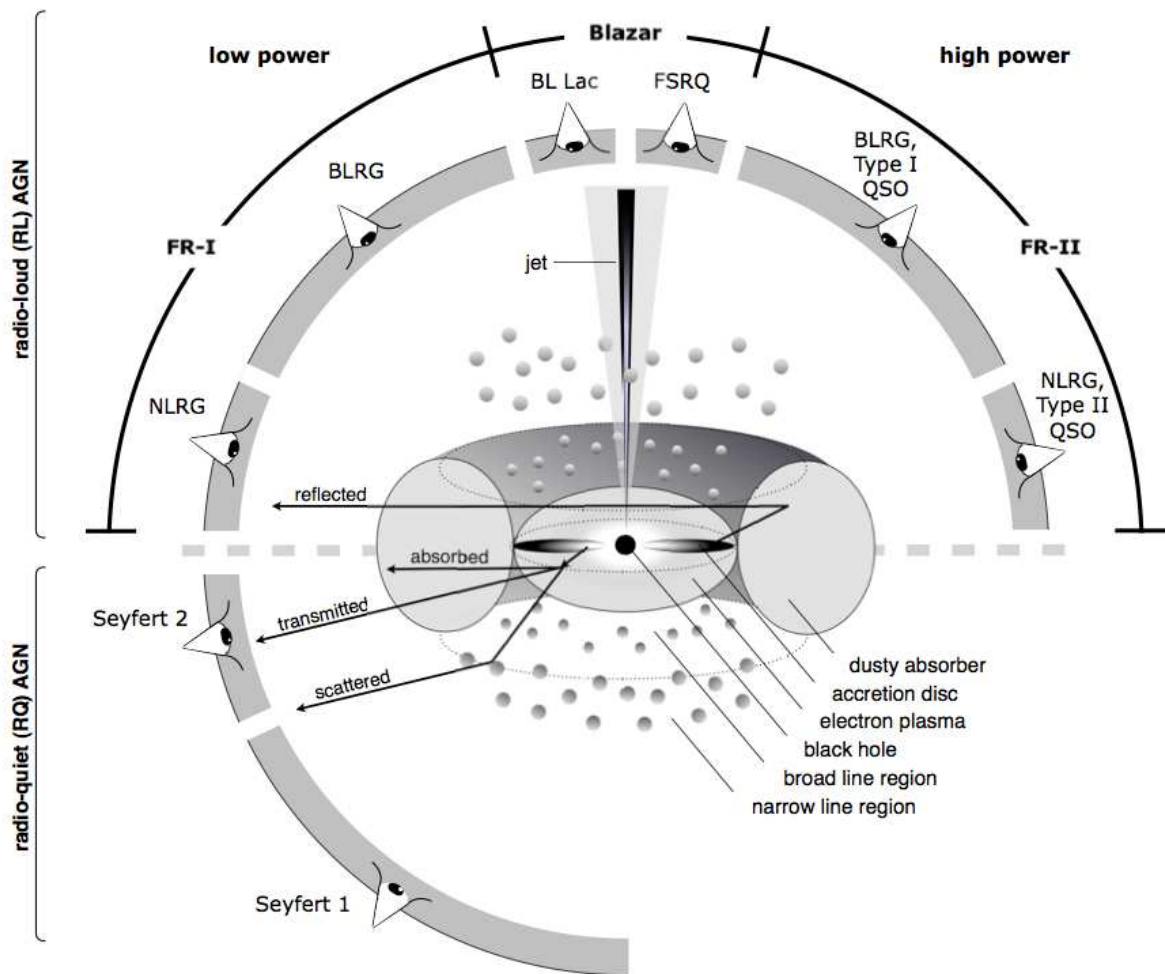
Figure 1.3 Schematic Unified Model of radio-quiet and radio-loud AGN. Figure from Beckmann & Shrader (2012).

objects, often known as true-Seyfert 2, are one of the challenges that the orientation model have yet to face.

It is important to underline that the torus cannot be considered as a monolithic, doughnut-shaped structure that surrounds the BLR. In fact to sustain its geometrical thickness, the vertical velocity dispersion must be so large that the corresponding temperature would sublimate the dust grains (Barvainis 1987). Therefore the torus must be formed by several dusty clumps with a low temperature (Krolik & Begelman 1988), and it can be considered as a natural continuation of the BLR clouds beyond the dust sublimation limit, or it could even be directly connected with the accretion disk (Kawaguchi & Mori 2010). The clumpy torus model can explain also the changing-look AGN as NGC 2617: when the line of sight goes through a *hole* in the clumps, the nucleus becomes directly visible and the AGN turns from a Sy2 to a Sy1 (Elitzur 2012).

Also radio-loudness RL plays a fundamental role in the Unified Model. There is a dichotomy between radio-loud and radio-quiet AGN, where the latters do not seem to raise a relativistic jet. Even if in the past a correlation between the radio luminosity and the black hole mass (Franceschini et al. 1998), or an anticorrelation between Eddington ratio and radio-loudness (Ho 2002) were found, the solution to the jet launching problem is not so simple. Recently it has been suggested that the dividing line is set by the relative spin of the black hole with respect to the accretion disk: if the black hole has a really different spin than the accretion disk, the interaction is strong, and thus a strong jet is formed (Garofalo et al. 2010). Nevertheless, the black hole spin is really difficult to estimate, and its actual relation with the radio-loudness is not resolutive yet.

For blazars the problem of the parent population was solved by Urry & Padovani (1995), where a connection between blazars and radio-galaxies was suggested. In particular, the physical properties of these sources revealed that there is a link between FRII galaxies and FSRQs, and between FRIs and BL Lacs. The first are high power sources, and when the source accretes with an high enough rate, it can produce jets powerful enough to generate hot-spots in the radio-lobes (Kozieł-Wierzbowska & Stasińska 2011). On the contrary, BL Lacs and FRIs have low power jets, and this also causes a more pronounced symmetry in the jets. The luminosity functions of these two classes confirm this scenario: once removed the relativistic beaming from blazars, their functions are the same of radio-galaxies. In summary, at least for now, the Unified Model is that summarized in Fig. 1.3. The upper part of the scheme unifies radio-loud sources, while the bottom part is for radio-quiet AGN. Both models are a function of the observation angle only.

Nevertheless, there is another class of sources not included in the previously described scenario. For many years they represented a challenge for this model, and their true nature is under debate even today: they are **narrow-line Seyfert 1 galaxies (NLS1s)**.

Chapter 2

Narrow-line Seyfert 1

2.1 Brief history

The first sign of the existance of NLS1s was found by Davidson & Kinman (1978): they noticed for the first time that the permitted lines in Mrk 359 were particularly narrow, around 500 km s^{-1}. This width is comparable to those of a typical Seyfert 2, but the object was definitely a type-1 AGN. Several sources with similar properties were discovered in the following years, until Osterbrock & Pogge (1985) provided the first "official" classification of this new class of AGN.

A typical spectrum of NLS1 is shown in Fig. 2.1. They have lines where the FWHM of the broad component is larger than the width of the forbbidden lines, but lower than 2000 km s^{-1} (Goodrich 1989), and the ratio between the fluxes of [O III] λ5007 and Hβ is lower than 3. Moreover, strong Fe II multiplets are visible, that tend to anticorrelate with the width of the Balmer lines (Boroson & Green 1992). In the X-ray band they often present a steep spectrum, much steeper than those of regular Seyferts, and they are also strongly variable (Boller et al. 1996). Such spectra are quite complex, and they show signs of partial covering, cold and ionized absorption and also reflection (Wang et al. 1996; Komossa & Meerschweinchen 2000; Gallo 2006).

One of the main physical difference between NLS1s and other Seyfert galaxies is the systematically lower black hole mass (10^{6-8} M$_\odot$). The mass can be determined both using the reverberation mapping (Peterson et al. 2000), and from stellar velocity dispersion or bulge luminosity (Botte et al. 2004, 2005), but any method always provide a low mass. Even when some inclination effect is considered, for instance measuring the second order momentum of the Hβ line (Peterson et al. 2004; Collin et al. 2006), the mass slightly increases, but it remains in agreement with the typical values oberved in regular Seyfert population.

A consequence of the low BH mass is the high Eddington ratio. This is straightforward from Eqn. 1.16: since the bolometric luminosity of NLS1s is comparable to that of the other Seyferts, the black hole mass inevitably lead to a higher ϵ. This could be a sign that the black hole is efficiently accreting material, closely to the Eddington limit. This high accretion rate often induces radiation-pressure driven outflows (Proga et al. 2000). These features are particularly evident in the [O III] $\lambda\lambda$4959,5007 lines (Zamanov et al. 2002; Komossa et al. 2006). In several cases in fact these lines exhibit a strong blue component, known as *blue wings*, and in some exceptional objects both the [O III] lines are shifted toward lower wavelengths by few $\sim$100 km s^{-1}. Anyway, the origin of these so-called *blue outliers* is still
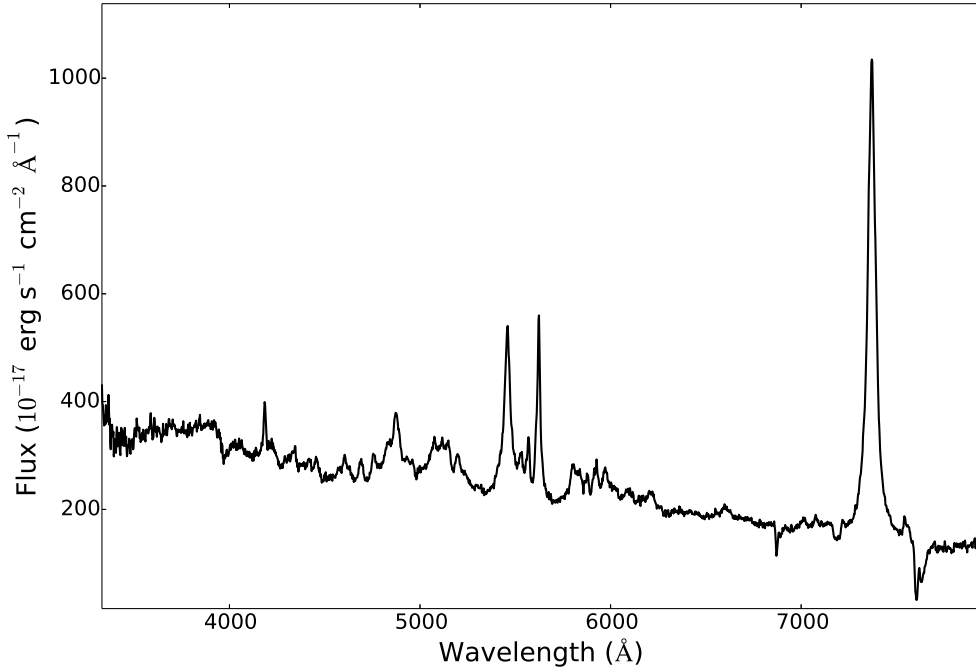
Figure 2.1 Optical spectrum of a narrow-line Seyfert 1. The spectrum was obtained with the Asiago 1.22m telescope.

under debate.

Studies on the host galaxy of NLS1s showed that they are quite often hosted in barred spiral galaxies (Crenshaw et al. 2003), particularly in those with a pseudobulges (Mathur et al. 2012). This might be an indication of secular evolution (Orban de Xivry et al. 2011): these structure in fact form when a galaxy does not interact with others via merging. The only mechanism that affects the galaxy evolution is then the evolution of stellar populations. NLS1s seem to be located in the low-mass tail of the Kaspi relation between bulge luminosity and black hole mass (Botte et al. 2005): this may be an indication of their nature. It is in fact possible that NLS1s are just an evolutionary phase of a Seyfert galaxy. They may be young objects, still gas rich, highly accreting and not interacting with their environment (Grupe 2000; Mathur 2000). Nevertheless, this is not the only possible explanation on the nature of NLS1s. Some authors in fact believe that in presence of a flattened BLR (Decarli et al. 2008; Pozo Nuñez et al. 2013) the lack of Doppler broadening would produce the narrow permitted lines, and make a regular Seyfert 1 appear as a NLS1. An observational hint for this model was obtained by Calderone et al. (2013). They claimed that using the AGN continuum between 1000 and 5000Å, they could constrain the accretion disk model under the assumption of thin disk, and then calculate the black hole mass. This method, which was anyway not tested on previously known sources, lead to systematically larger masses, closer to those of blazars, but the assumption of α-disk in all NLS1s is not so straighforward.

2.2 Radio-loud NLS1s

As shown before, radio-loudness plays a key role in the Unified Model. During the first years of study, NLS1s seemed definitely to belong to the radio-quiet population. Most of them in fact do not show any sign of radio emission, but in 1986 a first object violating this paradigm was discovered (Remillard et al. 1986). The galaxy PKS $0558 - 504$ was a radio-loud source, and later it was identified as a NLS1. Many objects similar to this were discovered in the following years, and in particular Komossa et al. (2006) showed that 7% of these sources are radio-loud. These radio-loud NLS1s (RLNLS1) are usually very compact radio sources, and they show some properties that closely remind those of blazars, such as high brightness temperature and also often a flat radio spectrum (Yuan et al. 2008). Nevertheless, a high brightness temperature is not necessarily associated with relativistic beamed jets. As shown by Tsang & Kirk (2007) a monoenergetic distribution of electrons can in fact reach a much higher temperature (10^{14} K) without necessarily undergoing the Compton catastrophe.

The real breakthough came with the launch of *Fermi Gamma-ray Space Telescope.* In 2009 the source known as PMN J0948+0022, whose optical spectrum was definitely that of a NLS1, was identified as a γ-ray emitter (Abdo et al. 2009a,b). This confirmed the presence of a relativistic beamed jet propagating from its inner core. In the following years, several other similar sources were discovered, revealing the existance of a new class of γ-ray emitting AGN besides blazars and radio-galaxies (Abdo et al. 2009b; Foschini et al. 2010). Nevertheless, as previously pointed out, the observational characteristics of NLS1s are different from those of blazars. The BH mass is in average two orders of magnitude lower, and the Eddington ratio is large, usually comparable to that of the most powerful quasars. Moreover blazars are usually hosted in early type hosts (Blandford & Rees 1978), while NLS1s are commonly, even if not solely, hosted in spiral galaxies. The jet power in this class of sources is moreover partially overlapped with that of BL Lacs but, once the power is rescaled for BH mass, their values are roughly comparable (Foschini et al. 2015). This result provides an interesting application in the unification of relativistic jets at all scales (Foschini 2014).

The γ-ray emission in NLS1s, until now, has tipically been detected in flat-spectrum radio-loud NLS1s (F-NLS1s), with only two exceptions in B3 1441+476 and RX J2314.9+2243, both steep-spectrum radio-loud NLS1s (S-NLS1, Komossa et al. 2015; Liao et al. 2015). Recently Foschini et al. (2015) studied the observational and physical properties of a sample of 42 F-NLS1s, the largest known to date. In their sample, 7 sources were γ-ray emitters (with one more later identified, D'Ammando et al. 2015), 22 have a flat radio-spectrum, while the others have no measured spectral index, and are assumed to be *bona fide* F-NLS1s. That investigation showed that, althought RLNLS1s show peculiar observational differences with respect to other radio-loud AGN, the physical properties of these souces reveal that RNLS1s are the low-mass tail of jetted-AGN.

This lower black hole mass implies that the observed jet luminosity is lower than that of quasars, and similar to that of BL Lacs. But if their jet power is similar, the reason why the detection of RLNLS1s is more difficult than that of BL Lacs is not immediately clear. BL Lacs are tipically more luminous in X-rays, because the synchrotron peaks in this spectral range, and X-ray surveys indeed found many BL Lacs (Padovani & Giommi 1995). In γ-rays, the characteristics of *Fermi*/LAT favour hard sources at low fluxes, again increasing the detection of BL Lacs instead of RLNLS1s. In radio, both of these sources are quite weak, but Giroletti et al. (2012) noted that BL Lacs have extended radio emission, which is almost entirely missing in RLNLS1s (e.g. Doi et al. 2012). A possible reason for this, suggested by

Doi et al. (2012), is that in case of RLNLS1s the jet has low kinetic power because of the small mass and because it has to propagate in a gas-rich environment. In BL Lacs, instead, the jet power is slightly larger and develops in a more rarefied medium. Another possibility is to invoke the young age of NLS1s (Mathur 2000; Mathur et al. 2012) and, indeed, many authors made the hypothesis of a link with GPS/CSS sources, which in turn are believed to be very young radio galaxies (Oshlack et al. 2001; Komossa et al. 2006; Gallo 2006; Yuan et al. 2008; Caccianiga et al. 2014). Another option was suggested by Gu & Chen (2010): the jet activity could be intermittent, as observed in other Seyferts (e.g. Brunthaler et al. 2005; Mundell et al. 2009). Therefore, as the technological improvement of radio surveys allows better monitoring of these sources, the rate of detection should increase (see Chap. 6).

The intermittent jet should not be confused with the outburst/flare activity as observed in blazars. In the case of RLNLS1s, the periods of activity/inactivity might be separated by dramatic changes in flux. This indicates a jet with a continuous background of emitted radiation, with superimposed outbursts and flares, as new blobs are ejected. The more dramatic changes of three-to-four orders of magnitudes observed in RLNLS1s suggests that the central engine changes its level of activity significantly: not only the jet, but also the corona seems to be strongly reduced. Czerny et al. (2009) proposed a radiative instability in the accretion disk to explain the intermittent activity in young radio sources. RLNLS1s have all accretion luminosities sufficiently high to be in the radiation-pressure dominated regime where Czerny's theory applies (Moderski & Sikora 1996; Ghosh & Abramowicz 1997; Foschini 2011a). The timescale of the active phase in the case of low-mass AGN could be very small, of the order of tens-to-hundreds of years (Czerny et al. 2009). Therefore, the low kinetic power of the jet due to the small mass of the central black hole, the short periods of activity, and a frustrating nearby environment rich in interstellar gas and photons, are the sufficient ingredients to explain the lack of extended radio relics. As suggested by Doi et al. (2012), such structures might appear only in the sources with largest black hole masses, which in turn might be in the final stages of their cosmological evolution before changing into broad-line AGN.

Another possibility is the aborted jet model proposed by Ghisellini et al. (2004), which in turn could also explain the difference between radio-loud and radio-quiet AGN. In this case, the jet has insufficient power to escape from the central black hole gravitational potential and falls back. The spectral characteristics in the X-ray band could be an index generally steeper than usual for Seyfert (that is $\alpha_x \sim 1$), large equivalent-width fluorescent iron lines, and a "steeper when brighter" behaviour of the light curves. 1H 0323+342 might be a good candidate, being also the only with a detected Fe Kα line. However, the X-ray flux and spectral index values by Foschini et al. (2015) do not reveal any significant trend. They also note that high-flux periods have both harder and steeper indices. They suggest that a jet might be sometimes aborted ("steeper when brighter") or launched ("harder when brighter"), but the mechanism causing this is not known yet.

The arise of this new class of γ-ray sources inevitably leads to ask how do they look like when randomly oriented. As shown before, the parent population of the two classes of blazars is radio-galaxies with steep radio-spectrum and radio-lobes. If the same occurs for F-NLS1s, from simple geometrical considerations the parent sources must be $2\Gamma^2$ times the number of beamed objects (see Sect. 1.3.1 and Urry & Padovani 1995). By taking into account a typical bulk Lorentz factor of $\sim$10 (e.g. Abdo et al. 2009b), if we consider only the 7 confirmed γ-ray sources, the parent population should count $\sim$1400 objects. If instead only the 21 sources with measured flat-spectrum are considered, the parent sources are $\sim$4800. Finally, considering the whole sample of 42 RLNLS1s, the parent population increases to $\sim$9600. These objects,

though, are missing. In fact detailed VLBI studies performed by many authors (Doi et al. 2006, 2007, 2011, 2012, 2015; Abdo et al. 2009a; Gu & Chen 2010; Gliozzi et al. 2010; Richards & Lister 2015) found just a handful of RLNLS1s with the jet seen at large angles. A clear example of the problem emerges by studying the complete sample of RLNLS1s studied by Yuan et al. (2008). It consists of 23 sources, 13 of them with flat spectrum and only 6 of them with a steep spectrum. The remaining 4 sources have no measured spectral index. Even if we consider these 4 as *bona fide* steep spectrum RLNLS1s, it is clear from these numbers that something is missing.

In order to explain the nature of the parent sources, Foschini (2011b, 2012b) proposed three options: S-NLS1s, radio-quiet NLS1s (RQNLS1s) and broad line/narrow line radio-galaxies (BLRGs/NLRGs). The first option, as mentioned before, is not numerically adequate to represent the whole parent population. A second option that could fill the gap is that the parent population is made of RQNLS1s. As mentioned before, many authors suggest that NLS1s are really young objects still growing. If this is true, when the jet is present they could have not developed extended radio-lobes yet, and also be very collimated. Therefore, when observed at large angles, they would become almost invisible for the present day observatories. Signs of non-thermal radiation possibly coming from relativistic jets in radio-quiet NLS1 have indeed been found (Giroletti & Panessa 2009; Tarchi et al. 2011; Doi et al. 2013; Schönell et al. 2014), and a few have also elongated radio-structures in their inner core (Moran 2000). A third hypothesis is based on a different assumption about the true nature of NLS1s. As mentioned before, some authors (Decarli et al. 2008; Risaliti et al. 2011; Shen & Ho 2014) believe that NLS1s can be due to an orientation effect of a disk-like shaped BLR. Therefore, when observed pole-on, there is no Doppler broadening and the FWHM of the permitted lines is then narrower than in a regular Seyfert 1. On the contrary, when observed edge-on, the lines are as broad as usual. In this way, a NLS1 with a beamed jet observed at a different angle would become a regular Seyfert galaxy (type-1 or 2 as always depending from the obscuration) but, because of its radio emission, it would be classified as a Broad or Narrow Line Radio Galaxy. Since NLS1s seem always to be hosted in disk galaxies, the BLRG/NLRG should also be hosted in a disk galaxy (both spiral and lenticular). Further support to this Doppler-lacking scenario comes from the detailed analysis of line profiles performed by Kollatschny & Zetzl (2011). They state that there is a correlation between radio-loudness and rotational velocity in the BLR. Therefore, since highly rotating sources have a flattened BLR, the line profiles can be strongly influenced by the inclination.

The main goal of this work is to investigate this parent population problem. I performed a large study in order to understand which one of the previously mentioned hypotheses is the best match for the parent population of F-NLS1s. To do this, I first calculated black hole masses and accretion rates for three sample of candidates, comparing them with the Foschini et al. (2015) sample. Then I investigated the incidence of blue wings and blue outliers among radio-quiet and radio-loud NLS1s, in order to understand the dynamics of their NLR and to find out if the difference between these two populations is only due to orientation. Finally, I built the radio luminosity function of CSS/HERGs, and compared it with that of the F-NLS1s population. Throughout this work, I adopt a standard ΛCDM cosmology, with a Hubble constant $H_0 = 70$ km s^{-1} Mpc^{-1}, and $\Omega_\Lambda = 0.73$ (Komatsu et al. 2011).

Chapter 3

Black hole masses and accretion rates

3.1 Introduction

This chapter was published as a paper in Astronomy & Astrophysics Issue n°578, p.28. In this work I studied the mass and Eddington ratio distribution of the three samples of parent population candidates, comparing them by means of the Kolmogorov-Smirnov test with the F-NLS1s population analyzed by Foschini et al. (2015), where I also calculated these values for the largest to date sample of beamed RLNLS1s.

3.2 Sample selection

To check the three different hypotheses about the parent population of F-NLS1s, I created three samples and one control sample. To improve the otherwise small number statistics, I chose to add every source I found in the literature, at the expense of having incomplete samples. Since my aim is to use the Hβ and [O III] λ5007 Å lines to estimate the BH mass and the Eddington ratio, I limited my study to objects with an optical spectrum that I could analyze.

I calculated the radio-loudness for each source as in Eq. 1.1. For 22 of them the only radio flux available was at 1.4 GHz, therefore I extrapolated their 5 GHz flux in approximation of a typical synchrotron steep spectrum with spectral index $\alpha = 0.7$ ($F_\nu \propto \nu^{-\alpha}$). The B-band magnitude, when possible, was derived directly from the optical spectrum. I convolved it with a B-filter template using the IRAF task `imarith` and then I calculated the integrated flux using `tintegrate`. Otherwise, I retrieved the B magnitude from NED[1] and SIMBAD[2] archives.

RLNLS1s: The first group consists of 18 NLS1s with a steep radio spectral index $\alpha > 0.5$ and a radio-loudness $R > 10$. This is done in analogy with what done by Foschini et al. (2015), whose sample included all those sources with $\alpha < 0.5$ and those with unknown spectral index. The sample was selected by using all the sources found in previous surveys (Zhou & Wang 2002; Wadadekar 2004; Komossa et al. 2006; Whalen et al. 2006; Yuan et al. 2008) and from

---

[1]http://ned.ipac.caltech.edu
[2]http://simbad.u-strasbg.fr/simbad/

individual studies (Gliozzi et al. 2010; Tarchi et al. 2011; Caccianiga et al. 2014). All the sources are classified as NLS1s according to their FWHM(Hβ) < 2000 km s^{-1}, their ratio [O III]/H$\beta < 3$, and the presence of Fe II multiplets. The only outlier, J1413$-$0312, is described in Sect. 3.7.

RQNLS1s: The second group, 25 radio-quiet - but not radio-silent[3] - NLS1s with $R < 10$, includes all the sources detected at 1.4 GHz by an early release of the FIRST VLA survey (Becker et al. 1995), as reported by Wadadekar (2004). In their work, they crossed the FIRST data with the Véron-Cetty et al. (2001) catalog, detecting 774 AGN. For each of those sources, I searched in the literature for its classification. Then I confirmed all the classifications by analyzing the optical spectra derived in SDSS DR9, or by observing the sources with the Asiago 1.22m telescope.

BLRG/NLRG: The third group, 16 disk-hosted radio galaxies (RGs), was selected from data available in the literature. To confirm the host galaxy nature, I cross-checked the classifications found in the HyperLeda database[4] (Paturel et al. 2003) with what I found in the literature. I kept only sources with a confirmed classification. For a description on specific objects, see Sect. 3.7.

As control sample I chose to use the flux-limited sample of 2 Jy RGs defined by Inskip et al. (2010). Their 43 sources have a flux density F$_{2.7GHz} > 2$ Jy and a declination $\delta < 10°$. 12% of them are found to be hosted in disk galaxy in that same work, and therefore I included them in the third group. The others are objects hosted by elliptical galaxies. I obtained an optical spectrum for 11 of them, and used these as control sample (see Sect. 3.3). The samples are listed in Tables 3.1, 3.2, 3.3 and 3.4. Finally I used the sample of F-NLS1s shown in Table 1 by Foschini et al. (2015) to compare the physical properties of my candidate parent sources with those of the beamed population.

3.3 Data analysis

The primary sources for the optical spectra were the Sloan Digital Sky Survey (SDSS) Data Release 9 and the NED archive. For all sources with a declination higher than -15°, an apparent magnitude lower than 18 and no published spectrum, I obtained a spectrum using the 1.22m telescope of the Asiago Astrophysical Observatory (Italy). In one case, J0559$-$5026, I converted the optical spectrum from Remillard et al. (1986) into an analyzable FITS format using the `digitizer` software[5]. The sources of the spectra are reported in Tables 3.1–3.4.

The subsequent data reduction was performed using the standard tasks of `IRAF v.2.14.1`. I collected the long-slit spectra at the Asiago 1.22m telescope during 30 observing nights between April 2013 and September 2014. During the whole Ph.D., I spent over 120 observing nights in Asiago, getting spectra of several different targets (not only AGN, e.g. see Ochner et al. 2015), with both the 1.22m and the 1.82m Asiago telescope. For my observations I used the Boller & Chivens spectrograph with a 300 mm^{-1} grating, which is ideal to cover a large spectral range (see Tab. 3.5) having also a good instrumental resolution, R $\sim$ 700. The latter is defined as

$$R = \frac{\lambda}{\Delta\lambda} \,, \tag{3.1}$$

---

[3]I highlight again that throughout this work with the term radio-quiet NLS1s I always refer to radio-emitting sources with $R < 10$. Sources with no detected radio-emission are instead labelled as radio-silent.

[4]http://leda.univ-lyon1.fr

[5]http://digitizer.sourceforge.net/

Table 3.1 Steep-spectrum radio-loud NLS1s sample. (1) Short name of the object; (2) alias from NED; (3) right ascension in J2000; (4) declination in J2000; (5) redshift; (6) column density of hydrogen, in units of 10^{21} cm^{-2} (Kalberla et al. 2005); (7) radio-loudness; (8) source of the optical spectrum: S for SDSS DR9, A for Asiago telescope, T for Telescopio Nazionale Galileo, P for PDF, N for NED.

Name	Alias NED	R.A.	Dec.	z	nH	RL	Source
J0146−0040	2MASX J01464481−0040426	01h46m44.8s	−00d40m43s	0.083	0.291	13	S
J0559−5026	PKS 0558−504	05h59m47.4s	−50d26m52s	0.137	0.346	26	P
J0806+7248	RGB J0806+728	08h06m38.9s	+72d48m20s	0.098	0.299	82	A
J0850+4626	SDSS J085001.17+462600.5	08h50m01.2s	+46d26m01s	0.524	0.267	272	S
J0952−0136	Mrk 1239	09h52m19.1s	−01d36m43s	0.020	0.341	16	A
J1034+3938	KUG 1031+398	10h34m38.6s	+39d38m28s	0.042	0.114	33	S
J1200−0046	SDSS J120014.08−004638.7	12h00m14.1s	−00d46m39s	0.179	0.210	172	S
J1302+1624	Mrk 783	13h02m58.8s	+16d24m27s	0.067	0.188	23	A
J1305+5116	SDSS J130522.74+511640.2	13h05m22.7s	+51d16m40s	0.788	0.094	73	S
J1413−0312	NGC 5506	14h13m14.9s	−03d12m27s	0.006	0.509	483	A
J1432+3014	SDSS J143244.91+301435.3	14h32m44.9s	+30d14m35s	0.355	0.120	577	S
J1435+3131	SDSS J143509.49+313147.8	14h35m09.5s	+31d31m48s	0.502	0.113	6998	S
J1443+4725	SDSS J144318.56+472556.7	14h43m18.5s	+47d25m57s	0.706	0.146	1331	S
J1450+5919	SDSS J145041.93+591936.9	14h50m41.9s	+59d19m37s	0.202	0.081	30	S
J1703+4540	SDSS J170330.38+454047.1	17h03m30.4s	+45d40m47s	0.060	0.253	151	A
J1713+3523	FBQS J1713+3523	17h13m04.5s	+35d23m33s	0.083	0.246	73	S
J1722+5654	SDSS J172206.03+565451.6	17h22m06.0s	+56d54m52s	0.426	0.209	429	S
J2314+2243	RX J2314.9+2243	23h14m55.7s	+22d43m25s	0.169	0.653	17	A

Table 3.2 Radio-quiet NLS1s sample. Columns as in Table 3.1.

Name	Alias NED	R.A.	Dec.	z	nH	RL	Source
J0044+1921	RGB J0044+193	00h44m59.1s	+19d21m41s	0.181	0.316	5.6	A
J0632+6340	UGC 3478	06h32m47.2s	+63d40m25s	0.013	0.676	<10	T
J0752+2617	RX J0752.7+2617	07h52m45.6s	+26d17m36s	0.082	0.340	1.6	S
J0754+3920	B3 0754+394	07h58m00.0s	+39d20m29s	0.096	0.512	3.0	A
J0913+3658	RX J0913.2+3658	09h13m13.7s	+36d58m17s	0.107	0.147	2.9	S
J0925+5217	Mrk 110	09h25m12.9s	+52d17m11s	0.035	0.131	2.0	A
J0926+1244	Mrk 705	09h26m03.3s	+12d44m04s	0.029	0.357	2.4	A
J0948+5029	Mrk 124	09h48m42.6s	+50d29m31s	0.056	0.115	6.1	S
J0957+2444	RX J0957.1+2433	09h57m07.2s	+24d33m16s	0.082	0.320	1.6	S
J1016+4210	RX J1016.7+4210	10h16m45.1s	+42d10m25s	0.056	0.112	0.9	S
J1025+5140	Mrk 142	10h25m31.3s	+51d40m35s	0.045	0.129	0.3	S
J1121+5351	SBS 1118+541	11h21m08.6s	+53d51m21s	0.103	0.095	1.9	S
J1203+4431	NGC 4051	12h03m09.6s	+44d31m53s	0.002	0.114	3.1	A
J1209+3217	RX J1209.7+3217	12h09m45.2s	+32d17m01s	0.144	0.134	4.2	S
J1215+5242	SBS 1213+549A	12h15m49.4s	+54d42m24s	0.150	0.155	4.0	S
J1218+2948	Mrk 766	12h18m26.5s	+29d48m46s	0.013	0.188	7.6	A
J1242+3317	WAS 61	12h42m10.6s	+33d17m03s	0.044	0.143	4.1	S
J1246+0222	PG 1244+026	12h46m35.2s	+02d22m09s	0.048	0.168	1.3	S
J1337+2423	IRAS 13349+2438	13h37m18.7s	+24d23m03s	0.108	0.100	4.0	A
J1355+5612	SBS 1353+564	13h55m16.5s	+56d12m45s	0.122	0.100	7.9	S
J1402+2159	RX J1402.5+2159	14h02m34.4s	+21d59m52s	0.066	0.195	1.7	A
J1536+5433	Mrk 486	15h36m38.3s	+54d33m33s	0.039	0.144	0.5	A
J1537+4942	SBS 1536+498	15h37m32.6s	+49d42m48s	0.280	0.169	9.6	S
J1555+1911	Mrk 291	15h55m07.9s	+19d11m33s	0.035	0.285	1.9	S
J1559+3501	Mrk 493	15h59m09.6s	+35d01m47s	0.031	0.213	3.8	A

and I evaluated it by measuring the average width of the reference lamp lines. Its value is inversely proportional to the slit aperture, that corresponded to 4.25" on the sky plane, a

Table 3.3 Radio galaxies with a disk host sample. Columns as in Table 3.1. Sources from the sample by Inskip et al. (2010) are marked with an asterisk.

Name	Alias NED	R.A.	Dec.	z	nH	RL	Source
J0010+1058	Mrk 1501	00h10m31.0s	+10d58m30s	0.089	0.574	315	A
J0150−0725	F 01475−0740	01h50m02.7s	−07d25m48s	0.018	0.203	1121	A
J0316+4119	IC 310	03h16m43.0s	+41d19m30s	0.019	1.240	298	S
J0407+0342	3C 105*	04h07m16.5s	+03d42m26s	0.089	1.090	115258	N
J0433+0521	3C 120*	04h33m11.1s	+05d21m16s	0.033	1.020	2181	A
J0552−0727	NGC 2110	05h52m11.4s	−07d27m22s	0.008	1.620	5372	A
J0725+2957	B2 0722+30	07h25m37.3s	+29d57m15s	0.019	0.590	242	A
J1140+1743	NGC 3801	11h40m16.9s	+17d43m41s	0.011	0.209	4101	S
J1252+5634	3C 277.1	12h52m26.3s	+56d34m20s	0.320	0.080	12646	S
J1312+3515	PG 1309+355	13h12m17.8s	+35d15m21s	0.183	0.100	40	S
J1324+3622	NGC 5141	13h24m51.4s	+36d22m43s	0.017	0.101	564	S
J1352+3126	UGC 8782	13h52m17.8s	+31d26m46s	0.045	0.126	21185	S
J1409−0302	SDSS J140948.85−030232.5	14h09m48.8s	−03d02m33s	0.137	0.463	60	S
J1449+6316	3C 305	14h49m21.6s	+63d16m14s	0.042	0.138	2994	S
J1550+1120	SDSS J155043.59+112047.4	15h50m43.6s	+11d20m47s	0.436	0.351	5397	S
J1704+6044	3C 351	17h04m41.4s	+60d44m31s	0.372	0.169	2584	A

Table 3.4 Control sample: radio galaxies with an elliptical host. Columns as in Table 3.1.

Name	Alias NED	R.A.	Dec.	z	nH	RL	Source
J0037−0109	3C 15	00h37m04.1s	−01d09m08s	0.073	0.223	1005	N
J0038−0207	3C 17	00h38m20.5s	−02d07m41s	0.220	0.285	63550	N
J0040+1003	3C 18	00h40m50.5s	+10d03m23s	0.188	0.556	2376	N
J0057−0123	3C 29	00h57m34.9s	−01d23m28s	0.045	0.328	1237	N
J0327+0233	3C 88	03h27m54.2s	+02d33m42s	0.030	0.809	14646	N
J0808−1027	3C 195	08h08m53.6s	−10d27m40s	0.109	0.760	11905	N
J0947+0725	3C 227	09h47m45.1s	+07d25m20s	0.086	0.204	9909	A
J1602+0157	3C 327	16h02m27.4s	+01d57m56s	0.105	0.576	16692	A
J1952+0230	3C 403	19h52m15.8s	+02d30m24s	0.059	1.130	16963	N
J2223−0206	3C 445	22h23m49.5s	−02d06m13s	0.056	0.484	3407	N
J2316+0405	3C 459	23h16m35.2s	+04d05m18s	0.220	0.550	11382	N

good compromise for obtaining the nuclear spectrum for nearby objects and the whole galaxy spectrum for high-redshift sources. The slit was always oriented at PA= 90°. The exposure time and the rest frame spectral coverage for each object is reported in Table 3.5. I split observations into exposures of 600 s, 1200 s or 1800 s each, to avoid a strong contamination by cosmic rays and light pollution.

I performed the whole reduction procedure using the fast reduction procedure `asgred`, specifically created for Asiago 1.22m telescope spectra. In the pre-reduction I used overscan instead of bias, and NeHgAr or HeFeAr lamps were used for the wavelength calibration. The lamps were always obtained immediately after two exposures: this avoids a large shift in the line position due to the small deformations of the focal plane induced by the telescope motion. As flux calibration reference, I observed a standard star with a similar altitude, hence airmass, to the scientific target. For the standard star observations, the slit covered 13.6" on the sky plane, to avoid any flux loss due to the seeing. After the flux calibration and the sky subtraction, I extracted monodimensional spectra for each object using the `apall` task of IRAF, and later combined them with `scombine` taking their median (e.g., see Fig. 3.1, or the spectra in the Appendix). The combination of at least three spectra using their median
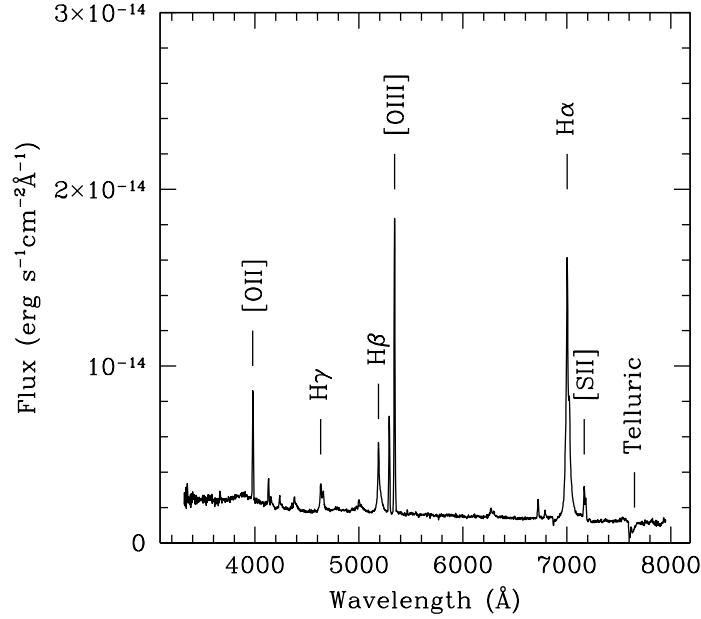
Figure 3.1 Spectrum of RLNLS1 J1302+1624 obtained with the Asiago Astrophysical Observatory 1.22m telescope.

allowed me to avoid an automatical subtraction of cosmic rays, along with the improvement of the S/N ratio.

In one case, J0632+6340, I obtained the optical spectrum in October 2005 using the 3.58m Telescopio Nazionale Galileo (TNG), with the DOLORES camera (device optimized for the low resolution). I used the MR-B Grm2 grism with a 1.1" slit with a resolution R $\sim$ 2100. The exposure time was 6100 s, and a He lamp was used to perform the wavelength calibration. The whole procedure is described in my master degree thesis (Berton 2010).

All the flux calibrated spectra were first corrected for Galactic absorption using the nH values reported in Kalberla et al. (2005), and were then corrected for redshift. The host galaxy contribution is negligible in many objects; in fact, for sources with redshift $z > 0.1$, the host component is lower than 10% of the whole spectrum (Letawe et al. 2007). In closer objects I examined the spectra for signs of stellar absorptions. In most cases the AGN continuum and lines were still much stronger than those coming from the host, particularly for type 1 objects, and the host subtraction had no influence on the line profiles, so I continued the analysis without subtracting its contribution, as done by Foschini et al. (2015). In type 2 or intermediate objects the absorptions were often clearly visible, and I subtracted an adequate host galaxy template (Kinney et al. 1996), according to the morphological classification and spectral shape of each object.

I focused my analysis on the Hβ region, between 4000 and 5500 Å: when the Fe II multiplets were present, I subtracted them using the online software[6] developed by Kovačević et al. (2010) and Shapovalova et al. (2012). This software provides a best-fit model that reproduces the iron multiplets in the Hβ region for each object as function of gas temperature, Doppler

---

[6]http://servo.aob.rs/Fe II_AGN/

broadening, and shift of the Fe II lines. The whole procedure is described with more detail in Sect. 4.3.3. An example of a template is shown in Fig. 3.2. I then proceeded in two different ways for type 1 AGN and intermediate or type 2 objects.

- **Sy1:** In this first case, I decomposed the Hβ line into three Gaussian components with the task `ngaussfit` of `IRAF`, one to reproduce the narrow component, and two more for the broad component. The center of the narrow component was always free to vary, and as suggested in Véron-Cetty et al. (2001), I fixed its flux to 1/10 of that of [O III] $\lambda 5007$, the mean value for Seyfert galaxies, and its FWHM to that of [O III]. Nevertheless, these parameters did not always provide a satisfactory result in fitting the line profile: the gas in which the [O III] originates is often turbulent, as indicated by the recurring presence of blue wings in the line profile, and the line global width can lead to an overestimate of the narrow component. For this reason I used the core component of the [O III] line as a reference, and I let the permitted narrow component width vary freely below the core width. Moreover, when the fit result was clearly incorrect, I also let the narrow component flux vary freely. In some cases I fitted the line with only two Gaussians, one broad and one narrow, because of an irregular Hβ profile. Once I obtained the best fit, I subtracted the narrow component and measured the line dispersion σ, defined as the second-order momentum of the broad component (see next Section). The use of σ instead of the FWHM gives better results for low-contrast lines, and also a lower uncertainty (Peterson 2011). I did not correct for the instrumental resolution, because even in the narrowest Hβ the effect of this correction is negligible.

- **Sy2/Sy-intermediate:** In the other sources I followed the same initial steps, but because of the obscuration due to the molecular torus, I could not use the Hβ broad line. Another way to determine the BH mass is to exploit its relation with the stellar velocity dispersion. However, in my objects the stellar absorption lines are almost invisible in the nuclear spectra, so I could not directly derive σ_*, and I used the forbidden lines instead. Low-ionization lines, such as [N II], are probably more suitable for this purpose, but they are not always present in the spectra because of the redshift, so I focused on the [O III] $\lambda\lambda 4959, 5007$ lines. I decomposed them using two Gaussians each, the first one representing a core component, and the second one representing the secondary (often blueshifted) component. To reduce the number of free parameters, I fixed both FWHMs to be the same in the two lines, and the flux of the $\lambda 4959$ line to be one-third of the $\lambda 5007$ line, as predicted by the theory. In objects where the $\lambda 4959$ line was dominated by noise I did not use any constraints and focused on obtaining a good fit to the $\lambda 5007$ line alone. Finally, in those cases where the FWHM of the core component was above the instrumental resolution limit, I measured it and corrected it for the instrumental resolution. This final correction was performed simply by quadratic subtracting the instrumental resolution from the measured resolution.

3.4 Mass and accretion rate

As shown above, for all the NLS1s and the type 1 objects, I calculated the σ of the broad component as the following. After the decomposition of Hβ with three Gaussians, I subtracted

Name	Exposure time (s)	Spectral coverage (Å)
J0010+1058	4800	2960−7280
J0044+1921	9600	2900−6700
J0150−0725	2400	3590−7760
J0433+0521	3600	3120−7680
J0552−0727	2400	3160−7840
J0725+2957	4800	3360−7750
J0754+3920	4800	2900−7200
J0806+7248	4800	2940−7220
J0925+5217	2400	3220−7780
J0926+1244	4800	3210−7680
J0947+0725	4800	3150−7270
J0952−0136	4800	3130−7750
J1203+4431	2400	3230−7940
J1218+2948	13200	3420−7860
J1302+1624	3600	3050−7450
J1337+2423	4800	3120−7180
J1402+2159	4800	3030−7460
J1413−0312	2400	3210−7890
J1536+5433	2400	3210−7760
J1559+3501	3600	3130−7720
J1602+0157	4800	2930−7200
J1703+4540	1200	3220−7450
J1704+6044	4800	2440−5800
J2314+2243	7200	2820−6760
J2345−0449	4800	3170−7340

Table 3.5 Observational details for Asiago optical spectra. (1) Object name; (2) exposure time in seconds; (3) rest frame spectral coverage (Å).

the narrowest component to obtain the broad profile. Then I evaluated numerically the ratio:

$$\sigma_{H\beta}^2 = \frac{\int \lambda^2 F(\lambda)\mathrm{d}\lambda}{\int F(\lambda)\mathrm{d}\lambda} - \left(\frac{\int \lambda F(\lambda)\mathrm{d}\lambda}{\int F(\lambda)\mathrm{d}\lambda} \right)^2 , \tag{3.2}$$

where $F(\lambda)$ is the emission line profile. Then I calculated the black hole mass under the hypothesis of a virialized system according to

$$M_{BH} = f \left(\frac{R_{\mathrm{BLR}}\sigma_{\mathrm{H}\beta}^2}{G} \right) , \tag{3.3}$$

where R_{BLR} is the radius of the BLR, G is the gravitational constant, and f is the scaling factor (Peterson et al. 2004) which, as suggested by Collin et al. (2006), I assumed to be 3.85. This value, as pointed out in their work, is not dependent on the inclination of the BLR, so it can be used in all my NLS1s samples. The same value was also used by Foschini et al. (2015), hence the results for F-NLS1s are directly comparable with mine. To find the BLR size, I used the relation developed by Greene et al. (2010) that links it to the Hβ luminosity,

$$\log \left(\frac{R_{\mathrm{BLR}}}{10 \text{ l.d.}} \right) = 0.85 + 0.53 \log \left(\frac{L(\mathrm{H}\beta)}{10^{43}\mathrm{erg} \text{ s}^{-1}} \right) . \tag{3.4}$$

By using an emission line to determine the BLR radius, I avoid the possible jet contamination that can affect the continuum luminosity at 5100 Å that is often used in many other studies.
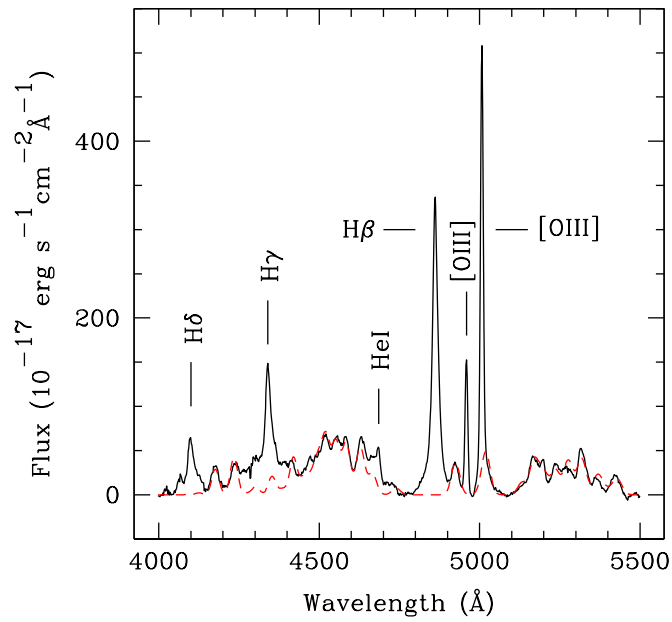
Figure 3.2 Spectrum of J0632+6340 (solid black line) obtained with the TNG, redshift corrected and continuum subtracted, with a Fe II template obtained from the online software (dashed red line).
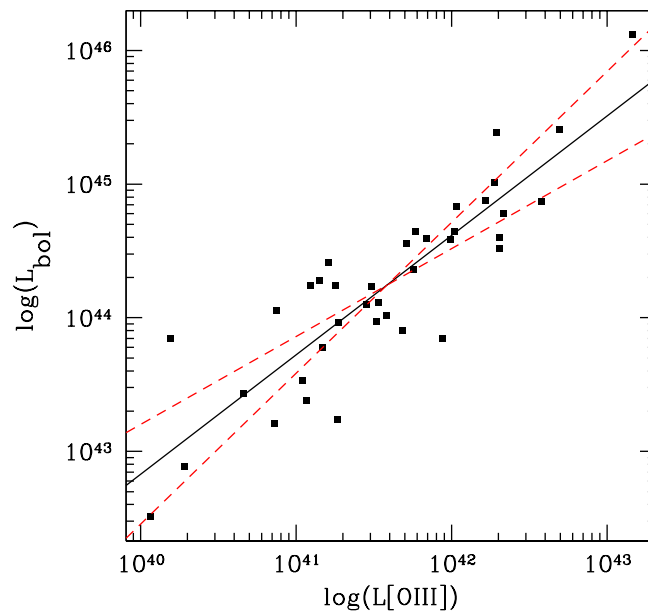
Figure 3.3 Relation between the [O III] $\lambda 5007$Å luminosity and the bolometric luminosity. The black solid line is the best fit, the red dashed lines are the highest and lowest slope lines.

The BLR size also provides a way to estimate the disk luminosity: assuming a photoionization regime,

$$\frac{R_{\text{BLR}}}{10^{17}\text{cm}} = \sqrt{\frac{L_{\text{disk}}}{10^{45}\text{erg s}^{-1}}} \tag{3.5}$$

(Koratkar & Gaskell 1991; Ghisellini & Tavecchio 2009). Under the reasonable hypothesis that the bolometric luminosity is comparable with the disk luminosity, I can estimate the Eddington ratio.

This second method, as already mentioned, is based on the [O III] $\lambda5007$Å line. As shown by Nelson & Whittle (1996) there is a relationship between the [O III] line width and the stellar velocity dispersion σ_* of the galaxy bulge. This relation was also investigated in the work by Greene & Ho (2005a), and they found that the estimates improve when the core component of [O III] is used instead of the whole FWHM. When both components had a FWHM higher than the instrumental resolution, I focused solely on the core component after decomposing the [O III] lines. In contrast, when one of the components was unresolved, I measured the FWHM of the entire line. These cases correspond to

$$\sigma_* = \frac{\text{FWHM}^c_{[\text{O III}]}}{2.35} \text{ and} \tag{3.6}$$

$$\sigma_* = \frac{\text{FWHM}_{[\text{O III}]}}{1.34 \times 2.35} . \tag{3.7}$$

As is widely known, σ_* is correlated with the black hole mass in the $M_{BH} - \sigma_*$ relation (Ferrarese & Merritt 2000). To estimate the masses, I used the revised relation found by Ho & Kim (2014):

$$\log\left(\frac{M_{\text{BH}}}{M_\odot}\right) = 8.49 + 4.38\log\left(\frac{\sigma_*}{200\,\text{km s}^{-1}}\right) . \tag{3.8}$$

The best way to obtain the bolometric luminosity for obscured sources is still debated; although it is commonly accepted that there is a relation between the [O III] line luminosity and the bolometric luminosity (i.e. Heckman et al. 2004; Wang & Zhang 2007; Lamastra et al. 2009; Risaliti et al. 2011), quantitatively it is still uncertain. I therefore decided to calculate a new normalization of the relation using my sample of type 1 objects. As previously explained, I derived the bolometric luminosity of NLS1s from the Hβ luminosity, and I measured the [O III] luminosity separately. As shown in Fig. 3.3, the correlation is evident. To find the best-fit line I used the least-squares method, which led to the following relation:

$$\log\left(\frac{L_{\text{bol}}}{\text{erg s}^{-1}}\right) = (7.54 \pm 9.07) + (0.88 \pm 0.22)\log\left(\frac{L_{[\text{O III}]}}{\text{erg s}^{-1}}\right) . \tag{3.9}$$

The dispersion in this relation is 0.2 dex. Under the assumption that the unified model is valid (Antonucci 1993), this relation can be used for type 2 or intermediate AGN, even if it was obtained from type 1 objects. I did not correct my data for intrinsic absorption of the galaxies, therefore the bolometric luminosity and the Eddington ratios might be underestimated and should be considered as lower limits.

3.5 Discussion

My results are displayed in Tables 3.6 and 3.7. I compared my findings with the sample of F-NLS1s studied by Foschini et al. (2015), and all of them are shown together in Figs. 3.4, 3.5

and 3.6. The masses of the Foschini et al. (2015) paper were calculated by me, following the same steps I described before for type 1 sources. I expect that the flat- and steep-spectrum populations have a similar mass distributions, and they both should be different from that of the control sample of elliptical radio-galaxies.

The mass and accretion luminosity values for both NLS1s samples roughly agree with previous results found in the literature (see Järvelä et al. 2015). The Eddington ratio ϵ is quite different only in J1413−0312, as discussed in Sect. 3.7. The two samples have similar distributions. The average mass value for RQ sources is 2.8×10^7 $M_\odot$, and a median of 1.6×10^7 $M_\odot$, while S-NLS1s have an average mass of 4.5×10^7 $M_\odot$ and a median of 2.3×10^7 $M_\odot$. For both samples the dispersion is 0.8 dex. These two results are quite similar to the average value of 6.2×10^7 $M_\odot$ found for F-NLS1s (Foschini et al. 2015). The difference between the average and median of the two samples is due to the presence of a few high-mass objects in the distributions.

The samples of radio-galaxies have different mass distributions that strongly depend on whether the host galaxy is a disk or an elliptical, and this is particularly evident in the histogram of Fig. 3.5. This can be understood in the context of the $M_{BH} - \sigma_*$ relation. The stellar velocity dispersion in disk-galaxy bulges is systematically lower than that in elliptical galaxies, and inevitably leads to a lower BH mass. Disk RGs have average and median masses of 3.8×10^8 and 1.1×10^8 $M_\odot$, with a dispersion of 0.8 dex. For elliptical RGs, instead, average and median masses are 1.8×10^9 and 1.4×10^9 $M_\odot$, with a dispersion of 1.2 dex. These values, as expected, are an order of magnitude higher than the others.

The Eddington ratio is on average lower in RGs than in NLS1s. This may be due both to a real physical effect and to an underestimate of the bolometric luminosity (see Sect. 3.4). Despite this, there are a few disk-hosted RGs for which ϵ is similar to that of NLS1s. A few ellipticals also have a relatively high ϵ, in analogy with the high-mass/high-Eddington ratio typical of FSRQs. The remaining elliptical galaxies are instead located at low ϵ, in a similar way to the BL Lacs (Ghisellini et al. 2010).

3.5.1 Kolmogorov-Smirnov test

The best way to define the relations between the different population is to determine their luminosity function. This cannot be done in this case, since my samples are statistically incomplete. For this reason, I decided to perform a two-sample Kolmogorov-Smirnov (K-S) test to verify the compatibility between the different populations of BH masses. The aim of this non-parametric test is to verify the probability that a null hypothesis is true. In this case the null hypothesis is that the two mass distributions originate from the same population. Given two samples of n and m elements, the test evaluates the strongest deviation D_n between their cumulative distributions and weights it by multiplying it for a corrective factor, $\sqrt{\frac{nm}{n+m}}$, which accounts for the number of sources in each sample. When the product

$$\mathcal{P} = D_n \sqrt{\frac{nm}{n+m}} \ , \tag{3.10}$$

has a lower value than a fixed threshold, the two distributions are assumed to be generated by the same population. Since I work with incomplete samples that can have a large intrinsic scatter, I decided to fix the rejection of the null hypothesis at a 99.5% confidence level, corresponding to a threshold of $\mathcal{P} = 1.73$. To provide additional evidence for my results, I

Name	$\log \mathrm{L}_{H\beta}$	$\log \mathrm{L}_{[OIII]}$	$\log \mathrm{M}_{BH}$	$\log \mathrm{L}_{bol}$	$\log \epsilon$
RLNLS1s					
J0146−0040	41.79	−	7.35	44.25	-1.22
J0559−5026	42.74	−	7.41	45.25	-0.28
J0806+7248	41.41	−	6.68	43.84	-0.96
J0850+4626	42.30	−	7.65	44.78	-1.00
J0952−0136	41.41	−	7.02	43.84	-1.30
J1034+3938	40.95	−	6.30	43.38	-1.05
J1200−0046	42.09	−	7.31	44.56	-0.85
J1302+1624	42.05	−	7.36	44.52	-0.96
J1305+5116	43.56	−	8.47	46.12	-0.47
J1413−0312	−	40.62	8.07	43.30	-2.91
J1432+3014	42.38	−	7.49	44.87	-0.74
J1435+3131	42.16	−	7.48	44.64	-0.96
J1443+4725	42.52	−	7.36	45.01	-0.47
J1450+5919	41.67	−	6.99	44.11	-1.00
J1703+4540	40.30	−	6.49	43.68	-0.96
J1713+3523	41.11	−	7.13	43.53	-1.70
J1722+5654	42.39	−	7.60	44.88	-0.82
J2314+2243	42.79	−	7.95	45.30	-0.77
RQNLS1s					
J0044+1921	42.01	−	7.15	44.48	-0.80
J0632+6340	40.48	−	6.53	42.89	-1.70
J0752+2617	41.83	−	7.27	44.28	-1.10
J0754+3920	42.89	−	8.15	45.41	-0.85
J0913+3658	41.53	−	7.08	43.98	-1.22
J0925+5217	42.11	−	7.56	44.59	-1.10
J0926+1244	41.53	−	7.28	43.97	-1.40
J0948+5029	41.58	−	7.03	44.02	-1.15
J0957+2433	41.65	−	6.89	44.10	-0.89
J1016+4210	41.79	−	7.34	44.25	-1.22
J1025+5140	41.61	−	7.19	44.05	-1.22
J1121+5351	42.34	−	7.64	44.83	-0.92
J1203+4431	40.15	−	5.85	42.51	-1.40
J1209+3217	42.17	−	7.44	44.65	-0.89
J1215+5242	42.12	−	7.75	44.59	-1.30
J1218+2948	40.85	−	6.78	43.24	-1.70
J1242+3317	41.46	−	7.37	43.90	-1.52
J1246+0222	41.34	−	7.05	43.90	-1.40
J1337+2423	42.87	−	8.13	45.46	-0.85
J1355+5612	42.13	−	7.39	44.60	-0.89
J1402+2159	41.78	−	7.19	44.23	-1.05
J1536+5433	41.95	−	7.42	44.42	-1.10
J1537+4942	42.00	−	7.18	44.36	-0.92
J1555+1911	40.78	−	6.63	43.20	-1.52
J1559+3501	41.04	−	6.43	43.43	-1.10

Table 3.6 Mass and accretion luminosity estimated for NLS1s. Columns: (1) Name of the source; (2) logarithm of the Hβ luminosity; (3) logarithm of the [O III] λ5007 Å luminosity; (4) logarithm of the black hole mass; (5) logarithm of the bolometric luminosity; (6) logarithm of the Eddington ratio.

Name	$\log \mathrm{L}_{H\beta}$	$\log \mathrm{L}_{[OIII]}$	$\log \mathrm{M}_{BH}$	$\log \mathrm{L}_{bol}$	$\log \epsilon$
Disk RGs					
J0010+1058	42.42	–	8.15	44.91	-1.40
J0150−0725	–	40.40	8.08	43.10	-3.10
J0316+4119	–	39.28	7.47	42.15	-3.40
J0407+0342	–	41.09	9.50	43.70	-3.92
J0433+0521	42.19	–	7.68	44.66	-1.15
J0552−0727	–	40.65	7.63	43.33	-2.41
J0725+2957	–	39.87	6.74	42.63	-2.22
J1140+1743	–	38.48	8.89	41.30	-5.68
J1252+5634	–	42.94	8.68	45.32	-1.52
J1312+3515	43.01	–	8.54	45.54	-1.10
J1324+3622	–	39.54	7.81	42.32	-3.70
J1352+3126	–	39.89	8.01	42.64	-3.52
J1409−0302	–	40.31	8.78	43.01	-4.00
J1449+6316	–	41.10	8.03	43.72	-2.43
J1550+1120	–	43.04	7.22	45.42	0.08
J1704+6044	–	43.04	7.94	45.41	-0.64
Elliptical RGs					
J0037−0109	–	41.54	9.67	44.09	-3.70
J0038−0207	–	39.67	9.45	44.50	-3.06
J0040+1003	–	43.47	9.32	45.80	-1.64
J0057−0123	–	41.05	9.03	43.67	-3.48
J0327+0233	–	39.97	9.50	42.71	-4.89
J0808−1027	–	42.14	8.58	44.63	-2.07
J0947+0725	–	41.90	7.63	44.41	-1.33
J1602+0157	–	42.22	8.50	44.69	-1.92
J1952+0230	–	41.61	9.16	44.16	-3.11
J2223−0206	–	42.51	9.39	44.95	-2.56
J2316+0405	–	42.02	9.07	44.52	-2.66

Table 3.7 Mass and accretion luminosity estimated for radio-galaxies. Columns as in table 3.6.

Test 1	n	Test 2	m	$\mathcal{P}$
F-NLS1s	42	Elliptical RGs	11	2.83
F-NLS1s	42	S-NLS1s	18	1.35
F-NLS1s	42	RQNLS1s	25	1.82
F-NLS1s	42	Disk RGs	16	1.55
Yuan F-NLS1s	16	Yuan S-NLS1s	7	0.66
Yuan F-NLS1s	16	RQNLS1s	25	1.47
RQNLS1s	25	S-NLS1s	18	0.90
Disk RGs	16	Elliptical RGs	11	1.81
F-NLS1s	42	Pseudobulge RGs	16	0.95
Zhou RL	47	Zhou RQ	104	1.63

Table 3.8 Two-sample Kolmogorov-Smirnov test results for BH masses. Columns: (1) First tested population; (2) number of sources n in the first population; (3) second tested population; (4) number of sources m in the second population; (5) the product $\mathcal{P}$ of Eq. 3.10.

performed the test on the complete samples from the literature when possible. The results of the test are summarized in Tab. 3.8, while the cumulative distributions of the samples used in the K-S test are shown in Fig. 3.6.

First of all, the K-S test between the F-NLS1s sample and the control sample of elliptical RGs reveals that their mass distributions are completely incompatible. The $\mathcal{P}$ value of 2.83 is by far higher than the fixed threshold. This expected outcome might be a sign that incomplete
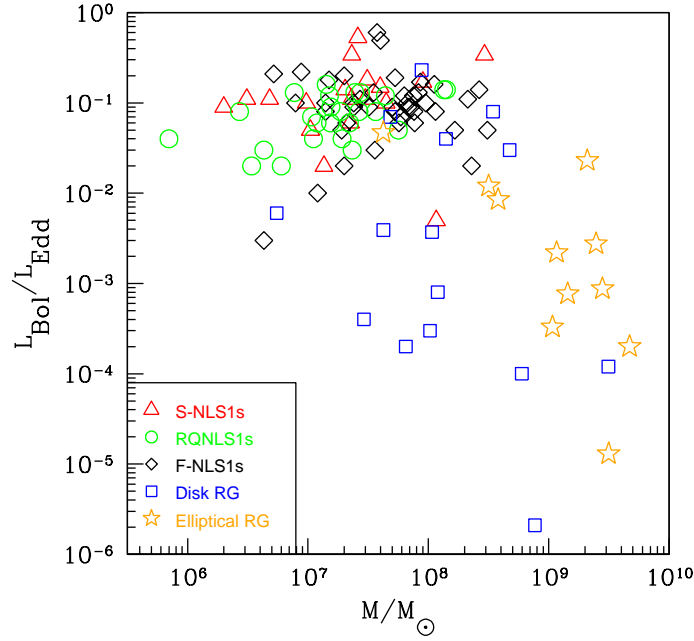
Figure 3.4 BH mass vs Eddington ratio. Red triangles are S-NLS1s, green circles are RQNLS1s, blue empty squares are disk-hosted BLRGs and NLRGs, and orange stars are elliptical RGs. In black I plot the sample of F-NLS1s from Foschini et al. (2015).

samples can also provide useful indications on the nature of these sources.

To compare flat- and steep-spectrum NLS1s, I first tested my two incomplete samples, which yielded a $\mathcal{P} = 1.35$. This result agrees with my expectation, since it suggests that the two mass distributions are the same. To provide additional confirmation of this outcome, I tested the null hypothesis on the Yuan et al. (2008) flux-limited sample. As mentioned in the introduction, this includes 13 flat radio spectrum and 6 steep-spectrum sources. Four other objects have unknown spectral indices. To preserve the ratio between the two groups, I therefore randomly included three of them in the flat-spectrum and one in the steep-spectrum sample. The new result for $\mathcal{P}$ from these complete samples, 0.66, strengthens the previous result, and it allows to conclude that F-NLS1s and S-NLS1s originate from the same population.

A second test was performed between the F-NLS1s and RQNLS1s. This time $\mathcal{P}$ is 1.82, which is higher than the threshold. This suggests that the two populations are intrinsically different, but when the K-S is performed between the Yuan et al. (2008) flat-spectrum sample and the RQ sample, the result points in the opposite direction. The value of 1.47 leads to conclude that the two distributions originate from the same population. This difference in the deviation between the complete and incomplete distributions suggests a selection effect due to the incompleteness of my F-NLS1s sample. For instance, the redshift distributions of the complete and incomplete samples are quite different, since the flat-spectrum objects are on average located farther away from Earth than the radio-quiet sources. Moreover, both the histogram of Fig. 3.5 and the cumulative distribution for F-NLS1s in Fig. 3.6 show that F-NLS1s masses are highly concentrated between $10^{7.5-8}$ $M_\odot$, and this might be interpreted
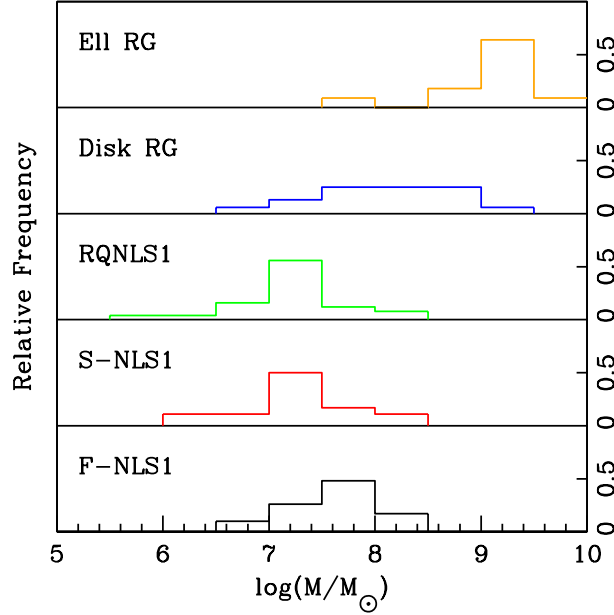
Figure 3.5 Mass distribution of the samples. From bottom to top: (1) In black, flat-spectrum radio-loud NLS1s from Foschini et al. (2015); (2) in red, steep-spectrum radio-loud NLS1s; (3) in green, radio-quiet NLS1s; (4) in blue, disk-hosted BLRGs and NLRGs; (5) in orange, elliptical RGs.

as a sign that a selection effect is also present in the flat-spectrum sample.

To further investigate this problem in depth, I performed a test on a larger complete sample of 2011 NLS1s derived by Zhou et al. (2006). The mass values they found are not directly comparable with mine because they used a different method to derive them. For this reason, I instead cross-matched their sample with the FIRST survey (Becker et al. 1995), finding all the radio-emitting sources. Then I split the resulting sample of 151 sources according to their radio-loudness, calculated as in my work. I finally compared the masses they found for the resulting samples of radio-quiet and radio-loud sources. I did not divide the radio-loud sample into steep- and flat-spectrum objects since, as shown before, they can be considered as part of the same population. The K-S test result is somewhat in the middle between my previous results, with a $\mathcal{P}$ of 1.63. This value is again below the rejection threshold, but it is higher than my result between complete samples. This might indicate that the radio-quietis actually different from the radio-loud population, but this conclusion is not so straightforward. These ambiguous results cause me to consider the K-S test as inconclusive for RQNLS1s.

The third test between F-NLS1s and disk RGs provides a $\mathcal{P}$ of 1.55. This is a really interesting result because it appears to relate NLS1s with sources that are usually considered a different class of AGN. At the same time the test indicates that disk RGs have a different mass distribution than elliptical RGs, since the $\mathcal{P} = 1.81$ is above the fixed threshold. Unfortunately, the disk RGs sample has no complete subsamples that I might have used to provide further confirmation of these results.
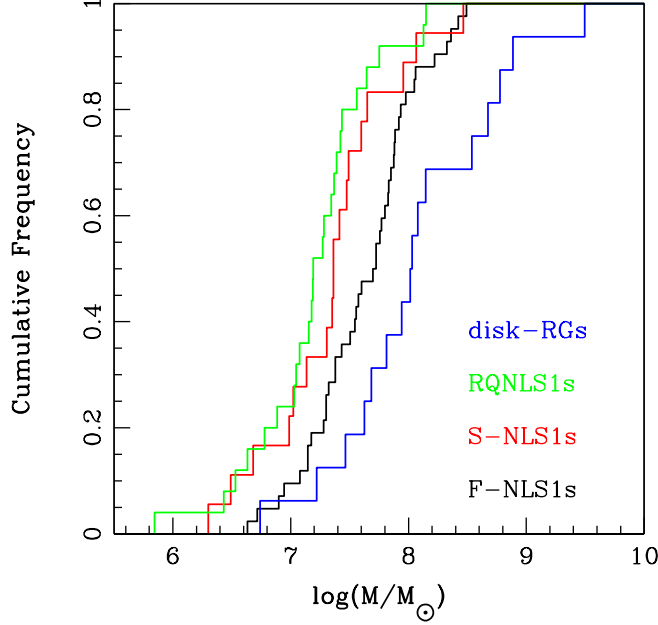
Figure 3.6 Cumulative distributions of the samples. (1) In black, flat-spectrum radio-loud NLS1s from Foschini et al. (2015); (2) In red, steep-spectrum radio-loud NLS1s; (3) in green, radio-quiet NLS1s; (4) in blue, disk-hosted BLRGs and NLRGs.

3.5.2 Resulting scenario

Steep-spectrum radio-loud NLS1s. The result for incomplete samples can be considered conclusive, and the complete samples provide further confirmation with an even more definitive outcome. Both of them reveal that flat- and steep-spectrum RLNLS1s originated from the same population. The different numerical result between complete and incomplete samples is probably due to a selection effect. Fig. 3.6, for instance, shows the distributions of the incomplete samples, and those of F-NLS1s and S-NLS1s are similar, but do not overlap systematically. The reason for this is that the flat-spectrum sample has many more sources at high z, while sources at low z are much more common in the steep-spectrum sample. The use of the Yuan et al. (2008) sample allowed me instead to compare sources with the same z distribution. This shows that the two mass distributions become closer, confirming the high compatibility of the two samples. Another hint that flat- and steep-spectrum RLNLS1s are related is given by Fig. 3.4. The samples almost entirely overlap in the plot because they not only have a similar mass distribution, but they also show similar distributions of ϵ, indicating that their accretion mechanism might be the same.

In conclusion, the resulting compatibility between the distributions of flat- and steep-spectrum sources in the two samples reveals that they originate from the same population. This occurs in analogy with what is observed for blazars and RGs, and explained in Sect. 1.4.6: when a flat-spectrum source is observed under a large inclination angle i, the radio-lobe emission starts to dominate the emission of the core, and the radio-spectrum becomes steep. The steep-spectrum sources therefore are misaligned F-NLS1s, and as expected they are parent sources. Nevertheless, as mentioned in the introduction, there are too few of them to

explain the nature of the whole parent population.

Radio-quiet NLS1s. As mentioned in the previous section, the K-S test on the radio-quiet sample cannot be considered conclusive because of its contradictory results. In particular, the result of the test between the radio-quiet sources and the F-NLS1s incomplete sample shows that they are not compatible. This result is also visible in Figs. 3.4 and 3.6. RQNLS1s are concentrated at lower masses than the Foschini et al. (2015) sample, so the two populations appear to be distinct. The cumulative distribution of RQNLS1s is also systematically higher than that of S-NLS1s, and this is a sign that radio-quiet sources are less similar to the beamed population than to the steep-spectrum population. When the two complete samples are compared instead, the data seem to indicate a higher compatibility between these two classes of sources, even if their redshift distributions are still quite different and therefore a selection effect might still be present. The large Zhou et al. (2006) sample of RQNLS1s and RLNLS1s reveals a slightly lower compatibility, but it does not indicate a clear separation between the samples. Therefore the result is not yet conclusive.

A possible explanation for this ambiguity is that all the radio-quiet samples are contaminated by sources that affect the results because they actually harbor a relativistic jet. It is true that radio-quiet sources can also exhibit jets, because radio-loudness is not an absolute parameter. As shown by Ho & Peng (2001), its value is strongly affected by the host galaxy contribution. Many sources can move from the radio-quiet to the radio-loud domain, depending on how their optical magnitude is measured, and also depending on which corrections are applied. That some RQNLS1s show an elongated structure or other signs that seem to reveal the presence of jets, indicates that at least some of them can be part of the parent population. In this context, the case of J0952−0136 (Mrk 1239) is indicative of this problem. While, according to my measurement, this source is slighly radio-loud, in the work by Doi et al. (2015) it is considered radio-quiet, and it exhibits a FRI-like pair of relativistic jets, therefore it must be part of the parent population.

Moreover, the mass distributions of the radio-quiet sample and of the steep-spectrum sample are very similar, with a $\mathcal{P} = 0.90$. The mathematical reason of this result is evident in Fig. 3.6: since their cumulative distributions are pretty close, they may originate from the same population. Therefore, if steep-spectrum radio-loud and radio-quiet sources really are the same class of objects, the latter might also be related to F-NLS1s. In conclusion at present it is neither correct to exclude the presence of jets in these sources a priori just because of their radio-quietness, nor is it correct to rule them out of the parent population. A detailed investigation is needed using new generation instruments, such as JVLA or SKA, to understand how often jets are present and if their presence can allow me to include RQNLS1s in the parent population and hence increase the low number of parent sources (see Chapter 6). A study on the radio luminosity function of the different populations will also provide useful results to solve this problem (see Chapter 5).

Disk-hosted RGs. As pointed out before, the K-S test seems to confirm the relation between F-NLS1s and disk RGs, revealing also that they are closer to the beamed sample than to elliptical RGs. As mentioned in Sect. 2.1, this can be interpreted in the frame of the unified model. If the BLR has a flattened component, the radio jet is probably perpendicular to it (La Mura et al. 2009). When the observing angle i is large enough, the rotational effect of the BLR clouds can broaden the permitted lines because of the Doppler effect and cause the NLS1 to appear as a BLRG. Then, when i is even larger and the line of sight intercepts the molecular torus, the nuclear regions are obscured and the source appears as an NLRG. Nevertheless, this scenario is unlikely to account for all the sources, since they show a high-

mass tail that no NLS1s sample has, and this is more similar to the mass distribution of elliptical RGs. A possible solution to this problem can be seen in Fig. 3.4. Disk RGs are somewhat similar to a "bridge" connecting the low-mass and high-accretion region occupied by NLS1s to the high-mass and low-accretion where the BL Lac-like elliptical RGs are located. Some of these sources may simply be genuine Seyfert 1 or Seyfert 2 galaxies with jets viewed at large angle, while some of them might instead belong to F-NLS1s parent population and therefore be just a misaligned NLS1 with Doppler-broadened lines. In Fig. 3.4 they show a very wide distribution of Eddington ratios that might be due to intrinsic differences between the objects of the sample. Some of them almost overlap with the NLS1s distribution, while others have a lower ϵ, more similar to slowly accreting sources such as regular Seyferts.

There is another interesting possibility regarding disk RGs that involves the nature of their bulges. It is not known a priori what their bulges look like, and in particular whether they are regular bulges or pseudobulges. The majority of low-redshift NLS1s are hosted in disk galaxies with a pseudobulge (Deo et al. 2006; Mathur et al. 2012), therefore it is reasonable to assume that their parent population shares the same characteristic. Ho & Kim (2014) developed a $M_{BH} - \sigma_*$ relation that can be used to calculate the BH mass in presence of a pseudobulge. Its only difference to Eq. 3.8 is the different zero-point, which is 7.91 instead of 8.49. Therefore, under this pseudobulge hypothesis, the logarithmic masses of Table 3.7 would be decreased by a factor 0.58, and all the mass distributions would be shifted by the same value. I tested this hypothesis by increasing the number of sources with a hypothetical pseudobulge in the disk RGs sample. The resulting $\mathcal{P}$ continues to decrease until it reaches the lowest value of 0.95 in the most extreme case of a pseudobulge in all sources. This might be a sign that a better match for the parent population of the Foschini et al. (2015) sample is not simply disk RGs, but more precisely, disk RGs with a pseudobulge.

In conclusion, some disk-hosted BLRGs/NLRGs, in particular those having a pseudobulge, might belong to F-NLS1s parent population. Including them in this group might help to explain the low number of parent sources. Nevertheless, their total number and the fraction of pseudobulges among them are still unknown. The host galaxy has been studied in quite a few objects, meaning that there are many sources of this type yet to be classified. Therefore a statistical study on this class of objects is needed to determine whether their population is large enough to completely fill the gap among the parent sources.

3.6 Summary

I tried to unveil the nature of the parent population of flat-spectrum radio-loud NLS1s. To do this, I analyzed the optical spectra of three samples of parent population candidates, steep-spectrum radio-loud NLS1s, radio-quiet NLS1s, and disk-hosted RGs, and of a control sample of elliptical RGs. In particular I focused on the Hβ and [O III] $\lambda 5007$, for type 1, type 2 and intermediate sources, to determine the BH mass and the Eddington ratio of each object. The NLS1s are all concentrated in the low-mass/high-accretion region, while elliptical radio-galaxies have systematically higher BH masses and typically lower Eddington ratios. Disk RGs instead span a wide interval of masses and Eddington ratios.

I performed a Kolmogorov-Smirnov test on all the samples to compare their BH mass cumulative distributions with that of the F-NLS1s population. Since my samples are statistically incomplete, these results must be taken with care, but some conclusions appear to be confirmed. In particular, the control sample has a completely different mass distribution

from all the other samples. The test showed that S-NLS1s have the same mass distribution as F-NLS1s and are, as expected, the best candidates for the parent population. Disk RGs are good candidates, and even if some of them might be genuine Seyfert galaxies, data suggest that those with a low-mass and high Eddington ratio and possibly a pseudobulge might be included in the parent population. Therefore the following scenario seems to emerge: when the inclination angle i increases, a beamed NLS1 appears first as a steep-spectrum NLS1. Then, with a further increase of i, the rotation of a flattened component in the BLR broadens the lines because of Doppler effect, and a disk-hosted BLRG appears. When finally the line of sight intercepts the molecular torus, the source turns into a type 2 AGN, and it appears as a disk-hosted NLRG.

My results are inconclusive on the connection between F-NLS1s and RQNLS1s, which must also be studied at radio frequencies to determine under which conditions they can develop jets. Statistical studies on larger complete samples are also needed to understand whether the number of parent sources can reach its theoretical value when the other classes of objects are included in the parent population along with S-NLS1s.

3.7   Notes on individual objects

J0010+1058
This Seyfert 1 galaxy has a σ of the Hβ broad component ~ 2300 km s^{-1} and showed several flaring episodes and superluminal motion in VLBI observations that can be explained with the presence of a relativistic jet (Brunthaler et al. 2000, 2005). Taylor et al. (1996) found that an exponential disk fits the NIR surface brightness of the source, while Surace et al. (2001) found a single tidal arm with high star formation extended 22 kpc to the north.
J0150−0725
This is a Seyfert 2 galaxy with a possible S0 host (McKernan et al. 2010). It has a strong radio emission but is unresolved on VLA scale (Thean et al. 2000). It has a flat FIR-to-radio spectrum, indicative of a strong nonthermal component (Heisler & Vader 1995).
J0316+4119
This is a Seyfert 2 radio galaxy in a lenticular host (Paturel et al. 2003). It was detected at very high energy, as reported by Neronov et al. (2010) and also by Kadler et al. (2012). It seems to be a low-luminosity FR I galaxy with an angle between the jet axis and the line of sight of $\theta \lesssim 38°$.
J0407+0342
This is a Seyfert 2 galaxy. According to Inskip et al. (2010), the host galaxy has both a bulge and a disk component, with the first being the brighter of the two. In radio the source has a typical FR II morphology, with a weak core and bright hot spots (Cohen et al. 1999). Its spectrum, retrieved in the NED archive and derived from the Low Resolution Spectrograph at TNG, has a spectral resolution of 20Å, therefore the [O III] line was not resolved.
J0433+0521
This is a Seyfert 1 galaxy with a low Hβ broad component, ~ 1500 km s^{-1}. It has a confirmed FR I morphology, with jets whose total extent exceeds 760 kpc (Walker et al. 1987). There is an optical jet in the same apparent direction as the radio jet (Barway et al. 2005). The host galaxy was analyzed by Inskip et al. (2010), and they found that it is better reproduced with a disk+bulge model, plus a nuclear point source that contributes 33% to the total flux.
J0552−0727

This is a Seyfert 2 galaxy, hosted in an SAB0 according to the RC3 catalog. HST imaging spectroscopy of the source revealed a jet-like region of [O III] emission extended for 1" (Mulchaey et al. 1994). It has a radio source consisting of a compact core with a flat spectrum and symmetric jets (Mundell et al. 2000).

J0725+2957

This is a Seyfert 2 galaxy with strong absorption lines in the optical spectrum. It is associated with a disk galaxy, particularly an S0, the only source in the B2 sample of this kind. The radio emission originates in two symmetric jets that form an angle of ∼45° with the Galactic disk (Capetti et al. 2000).

J1140+1743

This is a Seyfert 2 galaxy hosted in an S0 with a large-scale dust lane (Noel-Storr et al. 2003). Its spectrum is extremely red, with weak emission lines. I cannot exclude that the AGN is in its last phase before reaching a quiescent state (Hota et al. 2012). The source has symmetric jets, and it appears to be forming a disk.

J1252+5634

This is an Seyfert 1.5 galaxy hosted in a spiral galaxy with large tidal arms. It is a compact steep-spectrum object with a triple structure (O'Dea 1998) that shows emission-line gas aligned with the radio source (Hamilton et al. 2002). The gas structure forms a double shell-like morphology, with one lobe brighter and better defined than the other (Axon et al. 2000).

J1312+3515

This is a Seyfert 1 galaxy with a Hβ broad component $\sigma \sim 2530$ km s^{-1}, and it is hosted in a spiral galaxy (Hamilton et al. 2002). It was classified by Kellermann et al. (1989) as a flat-spectrum radio-intermediate QSO because of a relatively low radio-loudness, in agreement with my result.

J1324+3622

This is a Seyfert 2 galaxy with weak emission lines and a red spectrum. It is hosted by a S0 galaxy with a strong nuclear dust lane. Its radio morphology is that of a FR I radio galaxy with twin jets resolved on VLA scales (Noel-Storr et al. 2003).

J1352+3126

This is a Seyfert 2 galaxy whose optical spectrum increases toward longer wavelengths. It is a postmerger object, with the merged object being consistent with a late-type spiral galaxy. The radio source is also known as 3C 293, and it exhibits a one-sided jet. The latter shows emissions in optical, NIR, and UV and has a FR II structure (Floyd et al. 2006).

J1409−0302

Also known as Speca, this is an AGN, possibly a Seyfert 2 galaxy, hosted by a spiral galaxy that shows signs of recent episodes of star formation. The radio source has three pairs of lobes, probably produced by an intermittent radio jet activity from the AGN (Hota et al. 2011)

J1413−0312

Based to its optical spectrum, this source would be classified as a Seyfert 2 galaxy, with no broad component in the permitted lines and no sign of Fe II. Nevertheless, on the basis of its IR spectrum, Nagar et al. (2002) classified it as a NLS1, and I included it in the S-NLS1s sample. Since its Hβ line shows no sign of a broad component, I determined its physical properties using the technique for type 2 AGN. My results show that the source has a bolometric luminosity lower than the other NLS1s, and as a consequence a lower Eddington ratio. Its BH mass is not significantly different from the others. This discrepancy can be due to the strong absorption that affects the optical spectra of this object, which might lead to

an underestimation of the bolometric luminosity. When this parameter is estimated from a different spectral range, its value appears to be higher (Soldi et al. 2011).

J1449+6316

This is a Seyfert 2 galaxy. Its host has a disturbed morphology, and shows isophotal twists and two spiral arms, with a thin dust lane that crosses the nuclear region. The radio source has an FR I morphology with double-sided jets (Jackson et al. 2003).

J1550+1120

This is a Seyfert 1.5 galaxy, with a strongly asymmetric Hβ profile because of a strongly redshifted broad component. The host galaxy appears to have large tidal arms and a surface brightness profile well represented with an exponential profile (Hamilton et al. 2002). It also has jets, whose outer lobes show multiple bright spots (Rector et al. 1995).

J1704+6044

This is a Seyfert 1.5 galaxy with a very large Hβ broad component. The host galaxy is a spiral that contains a ring that surrounds an off-center bulge (Hamilton et al. 2002). The radio source is very steep and lobe-dominated; the two lobes are asymmetric, and one of them appears to be stopped by a dense environment (Goodlet et al. 2004).

Chapter 4

[O III] lines properties

4.1 Introduction

In this chapter I investigated the parent population problem from a different point of view. The previous study on masses and accretion rates did not provide a sure answer in the relation between radio-quiet and radio-loud NLS1s. Therefore I examined the [O III] lines profile of two complete samples of radio-emitting NLS1s, and focused my attention on the NLR of the two classes of sources.

To investigate this problem, and in particular the relation between radio-quiet and radio-loud NLS1s, I focused on the properties of the [O III] $\lambda\lambda$ 4959,5007 lines. In AGN with high Eddington ratio, such as NLS1s, powerful outflows can be generated by the radiation pressure coming from the accretion disk (Proga et al. 2000). The outflows have often been connected with the presence of an asymmetry in the [O III] lines (Greene & Ho 2005a). These lines indeed show two distinct components. The first one is the line core, which has typically the same redshift as the whole galaxy. The second component has instead a usually higher FWHM than the first one, and it is almost systematically blueshifted. This so-called *blue wing* has been directly associated with a gas outflow in the inner Narrow Line Region (NLR). This is not the only peculiarity of the [O III] lines: in some cases both of them show a blueshift with respect to their restframe wavelength. Those sources that exhibit this feature are known as *blue outliers*. According to previous studies, they occur between ~4% and 16% in NLS1s, depending on the definition (Zamanov et al. 2002; Komossa et al. 2008).

The generation mechanism of the [O III] shift is not well understood. A common hypothesis is that, as blue wings, the shift is induced by the strong winds generated by the high Eddington ratio. Nonetheless a different mechanism that can produce these blue outliers is a relativistic jet (Tadhunter et al. 2001; Komossa et al. 2008; Nesvadba et al. 2008). Typically the NLR axis and the extended radio-emission are aligned, a sign that a connection exists between these two features, and this is confirmed by the larger widths of narrow lines in AGN where a non-thermal radio jet is harbored, possibly due to an acceleration of the gas by the relativistic plasma (Pedlar et al. 1985; Peterson 1997). The jet can indeed release part of its energy into thermal energy of the surrounding gas. Anyway the efficiency of this process is not well determined yet. Recent simulations (Wagner & Bicknell 2011; Wagner et al. 2012) showed that the efficiency is a function of the jet power, and that only powerful jets can affect the gas kinematics in the NLR, hence originating a blue outlier.

The aim of this work is to investigate the incidence of blue wings and blue outliers in two

samples of radio-quiet and radio-loud NLS1s to determine whether a relativistic jet might be harbored also by RQNLS1s. I investigate the [O III] lines properties and the radio luminosity of the two samples, to understand if the mechanism powering the lines shift and asymmetry is the same. This chapter was submitted as a paper to Astronomy & Astrophysics.

4.2   Samples selection

4.2.1   RQNLS1s

The samples I used in the previous chapter were definitely too small to perform a statistical study, so I decided to enlarge them as much as I could. To have a uniformly selected sample of RQNLS1s which is not contaminated by any spurious source, I decided to use the sample created in the work by Cracco et al. (submitted) I co-authored. This sample was drawn from SDSS DR7 (Abazajian et al. 2009), selecting only emission-line objects with a redshift between 0.02 and 0.35. These limits allowed to keep within the spectral range both the [O II]$\lambda 3727$ line and [S II]$\lambda\lambda$ 6717, 6731. They selected only sources with a FWHM between 800 and 3000 km s^{-1}. The lower limit is based on the measurements of type 2 and intermediate type AGN performed by Vaona et al. (2012). The upper limit is instead large enough to avoid loss of sources due to measurements error. The final selection criterion was a S/N > 3 in the [O I]λ 6300 line. On the resulting sample they then applied the criteria of NLS1s, FWHM(Hβ) < 2000 km s^{-1} and ratio [O III]/Hβ < 3, obtaining 296 sources. They continued with a further selection by cross-matching the NLS1s sample with the FIRST survey (Becker et al. 1995), and looking for radio-sources within a radius of 5 arcsec from the SDSS coordinates. In this way they found 68 sources with an associated radio counterpart at 1.4 GHz. For each one they calculated then radio-loudness. To obtain the B-band flux they convolved the spectra with a B-filter template, measuring the integrated-flux, while to derive the 5 GHz flux they assumed a spectral index of $\alpha_\nu = 0.5$ (F$_\nu \propto \nu^{-\alpha_\nu}$, Yuan et al. 2008). In this way they found 9 RLNLS1s, that I will include in my second sample, and 59 RQNLS1s. To further increase the number of sources, I decided to add also the RQNLS1s from the previous chapter which were not already included in their sample because of the selection criteria, and which had a suitable spectra to analyze. My RQNLS1s sample in conclusion is made of 68 RQNLS1s.

RLNLS1s

For the RLNLS1s sample, besides the 9 sources I already found with the previous selection, I decided to use all the sources analyzed by Foschini et al. (2015) and in the previous chapter for which an optical spectrum was available in SDSS DR12, in the NED archive[1], or observable with the Asiago 1.22m telescope (Sect. 4.3.1). All the objects were classified as NLS1s using the same spectral criteria specified before. Moreover, they all have a radio-loudness parameter RL > 10. This sample includes both sources with a steep and flat radio-spectrum, and also 26 without a measured spectral index. Anyway, as I found in the previous chapter, steep-spectrum RLNLS1s are likely part of the parent population of flat-spectrum RLNLS1s, therefore they are the same kind of sources observed under a different angle. My aim is to characterize RLNLS1s as a whole, so I decided to include all of them in my sample regardless of their spectral index. My sample is then made of 56 RLNLS1s.

---

[1]http://ned.ipac.caltech.edu
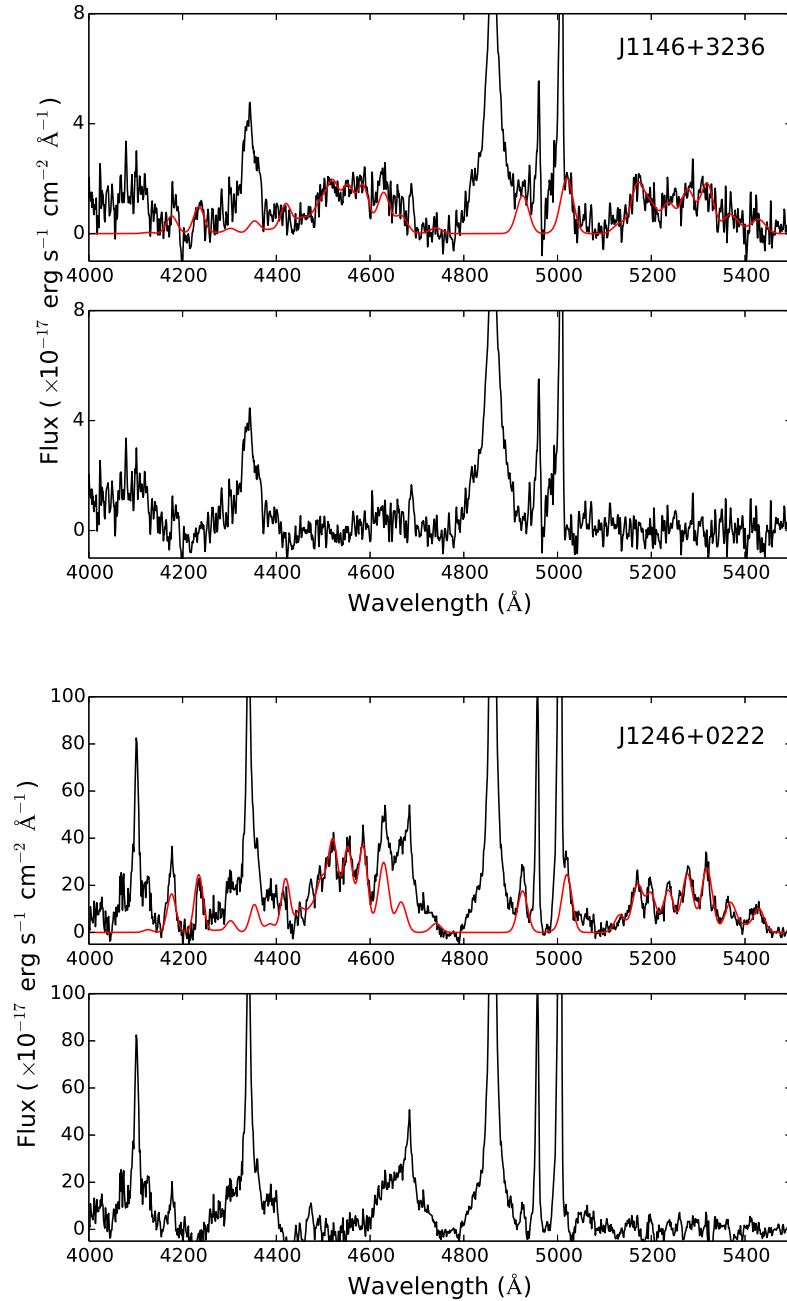
Figure 4.1 Hβ region of J1146+3236 (top 2 panels) and J1246+0222 (bottom 2 panels). The spectra have a S/N ratio of 10 and 40 in the 5100Å continuum, respectively. In the first panel of each source the black solid line is the spectrum corrected for Galactic absorption, redshift and continuum subtracted; the red solid line is the Fe II template. In the second panel of each source the black solid line is the spectrum with Fe II subtracted.

Table 4.1 Observational details for non-SDSS optical spectra. Columns: (1) Short name; (2) exposure time in seconds; (3) spectral resolution R; (4) Source of spectra: A for Asiago 1.22m telescope, T for *Telescopio Nazionale Galileo*, N for NED archive.

Name	Exposure time (s)	R	Source
J0324+3410	3600	700	A
J0632+6340	6100	2100	T
J0706+3901	480	723	N
J0713+3820	600	963	N
J0806+7248	4800	700	A
J0952+0136	4800	700	A
J0925+5217	6000	1400	A
J1203+4431	2400	1400	A
J1218+2948	3600	1400	A
J1337+2423	4800	700	A
J1536+5433	2400	700	A
J1555+1911	7200	1400	A

4.3   Data analysis

4.3.1   Data source

112 out of 124 optical spectra were extracted from the SDSS DR12. They have a resolution R $\sim$ 1700, and their wavelength calibration error is $\sim$2 km s^{-1} (Abazajian et al. 2009). 5 radio-quiet sources and 1 radio-loud were not included in SDSS, so I observed them with the Asiago 1.22m telescope. Moreover, 3 sources, J1218+2948, J1555+1911 and J1337+2423 are in the SDSS archive, but in the first two cases the optical spectra were not taken on nucleus so they show just the host galaxy contribution, while the last one was taken outside the galaxy, and its spetrum is just pure noise. For this reason, I decided to reobserve them with the Asiago telescope. These 9 spectra were obtained between 2014 January and 2015 March, using a Boller & Chivens spectrograph with a 300 mm^{-1} grating. The spectral resolution is between $\sim$700 and $\sim$1400, depending on the seeing conditions. I divided my observations in frames of 1200 s each, to decrease the contamination from cosmic rays and light pollution. All these spectra were reduced using the standard `IRAF v.2.14.1` tasks, using HeFeAr lamp for wavelength calibration and overscan in place of bias. The wavelength calibration error, evaluated on the HeFeAr lamp, is on average $\sim$20 km s^{-1}. Two more spectra were derived from the NED archive. Finally, one was obtained in October 2005 using the 3.58 m Telescopio Nazionale *Galileo* (TNG), with the DOLORES camera (device optimized for the low resolution). I used the MR-B Grm2 grism and a slit of 1.1", with an He lamp for wavelength calibration. Sources for non-SDSS spectra, exposure times and resolution are summarized in Tab. 4.1.

4.3.2   Preliminary correction

All the spectra were corrected for Galactic absorption, using the column density values reported by Kalberla et al. (2005). I then corrected for redshift. According to Komossa et al. (2008), the best method to perform this last procedure is to use as reference the stellar absorptions lines − that are not visible in my NLS1s spectra − or altenatively low ionization lines as [S II]$\lambda\lambda$6716,6731 and [O II] λ3727. Nevertheless [S II] is not visible in the spectra of RLNLS1s when $z \gtrsim 0.35$. The [O II] is instead present in 114 spectra, while it is not

visible in the remaining 11, 6 radio-loud and 5 radio-quiet. Anyway I decided to use it as reference. This line is actually a doublet, but the two lines are not resolved in any of my spectra, therefore I fitted its profile with a single Gaussian using an automatic procedure developed in `Python`. To determine the error on its position I used a MonteCarlo method. Since the fit was performed with only one Gaussian, the typical error is low, and of the same order of the wavelength calibration of SDSS spectra, ~ 2 km s^{-1}.

In those cases where the [O II] line was not present, I used the narrow component of Hβ line (Hβ_n) to determine the redshift, as in Zamanov et al. (2002) and Marziani et al. (2003). I reproduced the line profile using an automatic procedure which performs the fit using alternatively two or three Gaussians, one for the narrow and one or two for the broad component. The number of Gaussians was decided by the software according to the reduced chi-squared, χ^2_ν, of the fit. I did not use any constrain on position, intensity or width of the components. The typical error in the Hβ_n position, calculated again with a MonteCarlo method, is ~ 0.1 Å for two Gaussians, and ~ 0.5 Å for three Gaussians, corresponding to ~ 10 and ~ 30 km s^{-1}, respectively. Because of these relatively large uncertainties, I decided not to use the Hβ line as reference in all of my sources, but only when the [O II] was not present.

4.3.3 Fe II subtraction

After these preliminary corrections, I focused on the [O III] region fitting, where I removed the power-law continuum of the AGN. I neglected the host galaxy component since, as shown in Section 3.3, all the spectra of NLS1s are clearly dominated by the AGN, showing no signs of stellar contribution. I then removed the Fe II multiplets using the online software[2] developed by Kovačević et al. (2010) and Shapovalova et al. (2012). This template reproduces 65 FeII emission lines between 4000 and 5500Å, divided into 5 line groups, fitting each line with a single Gaussian. The required input parameters are Doppler width, shift in velocity of the Gaussians, intensity of each group of multiplets, and excitation temperature. I chose the input parameters after a preliminary measure on the spectra. For the Doppler width, in particular, I used as a first approximation the FWHM of Hβ, since both Fe II and Hβ are emitted mostly within the BLR. The online software creates a model that can be directly subtracted to the spectrum. The quality of the result was estimated by checking whether the residuals were comparable to the noise of the spectrum. The flux error, estimated by measuring the same model with different values of noise, is about $\sim 10\%$ for a S/N = 20 in the 5100Å continuum, and $\sim 20\%$ for a S/N = 10. Typical values of S/N are ~ 15 for RLNLS1s, and above ~ 20 for RQNLS1s. I can then assume an average error of $\sim 15\%$ for RLNLS1s, and of less 10% for RQNLS1s. An example of Fe II subtraction for different S/N ratios is shown in Fig. 4.1.

4.3.4 Hβ line

After the Fe II subtraction I continued with the fitting of Hβ. This line is crucial for evaluate the properties of the central engine in each NLS1s. As mentioned before, I decomposed it using alternatively two or three Gaussians as previously described. I then calculated the black hole mass, the bolometric luminosity and the Eddington ratio for each source. To do this, I followed the steps described in the previous chapter. Just to remind the basic concepts, my calculations are performed under the hypothesis of virialized system. As a proxy for the rotational velocity I used the second-order momentum of broad Hβ instead that the FWHM,

---

[2]http://servo.aob.rs/FeII_AGN/
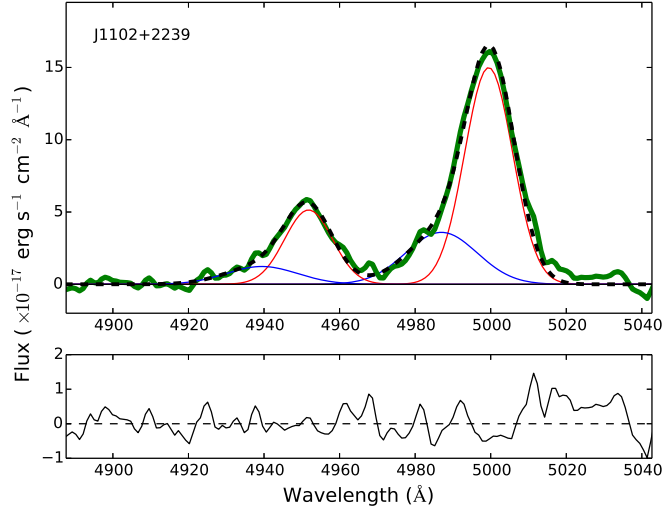
Figure 4.2 [O III] lines fitting with the automatic procedure in J1102+2239. **Top panel:** the thick green line is the original spectrum, continuum and Fe II subtracted. The blue and red solid lines represent the blue wing and the core component, respectively. The black dashed line is the sum of the resulting fit. **Bottom panel:** residuals of the fitting procedure.

because it is believed to be less affected by inclination and BLR geometry (Peterson 2011). To estimate the BLR radius, I exploited its relation with Hβ luminosity obtained by Greene et al. (2010) (see Section 3.4). My results, shown in Tables 4.4 and 4.5, are in very good agreement with those found by Foschini et al. (2015) and in Tables 3.6 and 3.7.

4.3.5   [O III] lines

The final step is the [O III] lines fitting. To reproduce their profile I used 4 Gaussians, 2 for each line. The first Gaussian is the blue wing, while the second is the core component. In all cases I fixed the flux ratio between each component of the λ4959 and λ5007 lines using its theoretical value of 1/3. I used the λ4959 line in order to verify the validity of the fit in the λ5007 line. When λ4959 had an amplitude lower than 3 times the RMS of the continuum at 5100 Å, I fitted just the λ5007 line. The fitting procedure was performed by using an automatic procedure which also allows me to estimate the errors on each parameter via MonteCarlo method. Each procedure was repeated 100 times. An example of [O III] lines automatic fitting is shown in Fig. 4.2.

In 14 sources, 11 radio-loud and 3 radio-quiet, I were not able to fit the [O III] lines with both the core and the wing. This occurs when the line has a too low S/N (4 cases, all radio-loud), or when it was already well reproduced by a single Gaussian (10 cases, 7 radio-loud, 3 radio-quiet). In those cases I only measured the peak position of the line, its core width and its flux. I measured the peak wavelength of each gaussian component, its FWHM, and the total flux of the λ5007 line. An example of fit is shown in Fig.4.1. Finally all the FWHM values were corrected for instrumental resolution, which was $\sim$167 km s^{-1} for SDSS spectra, and that specified in Tab. 4.1 for the other spectra. All of my results and their errors are shown in Tables 4.6 and 4.7 for radio-quiet and radio-loud sources, respectively.
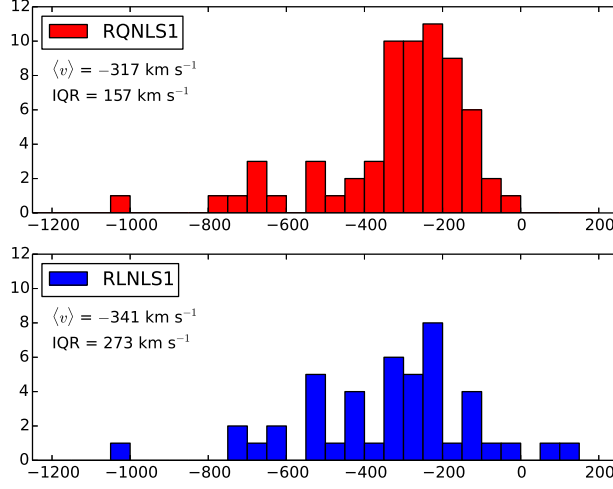
Figure 4.3 Histogram showing the velocity shift of the blue wings with respect to the core component. The negative velocity is due to the approaching gas. In top panel the RQNLS1s sample, in bottom panel the RLNLS1s sample. In each panel the average velocity and the IQR are shown.

Table 4.2 Correlation coefficients between the wing velocity and other quantities. (1) Tested sample; (2) Tested quantity ; (3) Pearson r coefficient; (4) Pearson p-value.

Sample	Q1	r	p-value
RQ non-outliers	FWHM_c	-0.5	8×10^{-6}
RL non-outliers	FWHM_c	-0.5	1×10^{-3}
RQ+RL non-outliers	FWHM_c	-0.5	2×10^{-8}
RQ outliers	FWHM_c	0.4	6×10^{-1}
RL outliers	FWHM_c	-0.2	6×10^{-1}
RQ+RL outliers	FWHM_c	0.1	8×10^{-1}
RQ non-outliers	FWHM_w	-0.2	8×10^{-2}
RL non-outliers	FWHM_w	-0.2	2×10^{-1}
RQ+RL non-outliers	FWHM_w	-0.2	2×10^{-2}
RQ outliers	FWHM_w	0.5	5×10^{-1}
RL outliers	FWHM_w	0.1	9×10^{-1}
RQ+RL outliers	FWHM_w	0.2	4×10^{-1}
RQ	Eddington	-0.1	7×10^{-1}
RL	Eddington	-0.2	3×10^{-1}
RQ	L_{bol}	-0.3	2×10^{-2}
RL	L_{bol}	-0.3	3×10^{-2}
RQ	L_{rad}	-0.3	2×10^{-2}
RL	L_{rad}	-0.1	7×10^{-1}
RQ	M_{BH}	-0.3	7×10^{-3}
RL	M_{BH}	-0.2	1×10^{-1}

4.4 Results

4.4.1 Blue wings

The blue wing is represented by the lower wavelength peaked Gaussian in both the [O III] lines. In 4 radio-loud sources neither the $\lambda4959$ nor the $\lambda5007$ lines could be modeled with
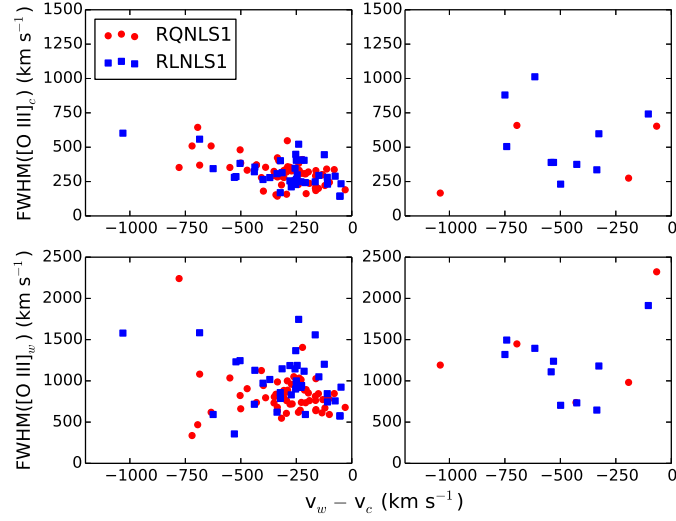
Figure 4.4 In top panels the velocity of the wing against FWHM of the core component for both samples, regular sources in the left and outliers in the right. In bottom panels the velocity of the wing against FWHM of the wing for both samples, as before. RQNLS1s are red circles, RLNLS1s are blue squares.

two Gaussians because the lines were too weak, while in 7 radio-loud and 3 radio-quiet sources the [O III] appears to have only a core component. In all the other cases I decomposed one or both the lines as previously explained, finding a blue wing in 108/110 cases, and a red wing instead only in 2 sources, both radio-loud.

Fig. 4.3 shows that the two distributions of the blue wing velocity are pretty similar. To test them I performed an Anderson-Darling (A-D) test (Hou et al. 2009). Such test is more sensitive than K-S to deviations in the tail of cumulative distributions. The null hypothesis is that the two distributions are drawn by the same population. The rejection of the null hypothesis throughout this work is fixed to a p-value below 0.05. The resulting p-value of the test is 0.33, therefore the null hypothesis cannot be rejected. Their average velocities, also indicated in Fig. 4.3, are quite close, with a slightly larger value among RLNLS1s. The interquartile range (IQR) of the radio-loud sample though is almost double than that of RQNLS1s, meaning that the velocity distribution in the radio-loud sample has a much larger intrinsic scatter.

I tested the correlation between the velocity of the wing and the FWHM of the core and wing component, respectively. The results are summarized in Tab. 4.2. Those sources where it was not possible to separate core and wing are not considered. At the beginning I did not find any correlation between these quantities. I then decided to test the separately these correlations for regular sources and outliers, all shown in Fig. 4.4. As in Xiao et al. (2011), I found a moderate but significant anticorrelation (Pearson r = -0.5, p-value = 4×10^{-8}) between the core component of [O III] and the wing velocity in the non-outliers sources, while I found no correlation (r = 0.1, p-value = 8×10^{-1}) among the outliers. Conversely I did not find a correlation between the wing FWHM and its velocity. These results, in particular the correlation among core FWHM and wing velocity, might be explained if a gas where a turbulent outflow is generated is turbulent itself. This gas would then show a high core FWHM due to this turbulence.
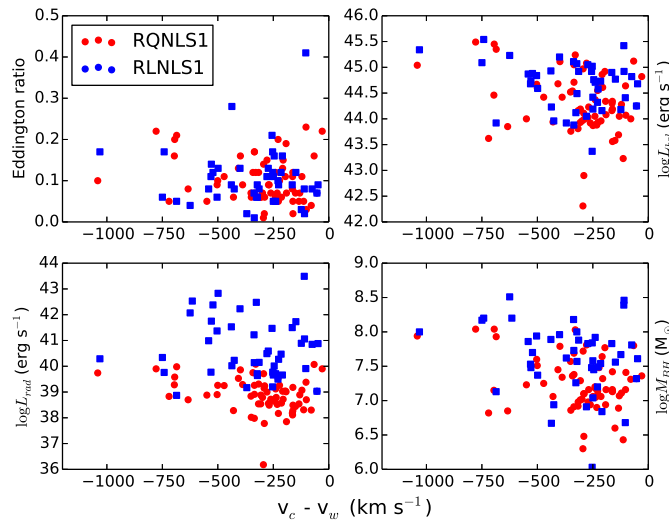
Figure 4.5 Correlations between the absolute value of the [O III] wing component velocity, in abscissa, and other quantities. **Top left:** Eddington ratio; **Top right:** logarithm of the bolometric luminosity (erg s^{-1}); **Bottom left:** logarithm of radio luminosity at 1.4 GHz (erg s^{-1}); **Bottom right:** logarithm of the black hole mass (M$_\odot$). RQNLS1s are red circles, RLNLS1s are blue squares.

The blue wings are thought to originate in outflows induced by the high Eddington ratio (Whittle 1985; Komossa et al. 2008). For this reason I looked for a correlation between the velocity of the wing and the Eddington ratio. I also tested the correlation with the black hole mass and the bolometric luminosity, since these quantities are directly related with the Eddington ratio, and with the radio luminosity which, if a jet is present, may have some effect on the gas velocity. The results are shown in Fig. 4.5, and it is already evident even at a visual inspection that no correlation is present among these quantities. The only significant, but very weak, trend is between the wing velocity and the black hole mass in RQNLS1s only ($r = 0.3$, p-value $= 7\times10^{-3}$). In this case blue outliers and regular sources seem to behave in the same way, since the exclusion of outliers does not change significantly my results.

4.4.2 Blue outliers

As mentioned in the introduction, few NLS1s show a blueshift of the [O III] lines. These kind of sources are called blue outliers, and a few examples are shown in Fig. 5.3. To look for them I calculated the distance between the measured peak of the $\lambda5007$ core component and its restframe wavelength (5006.843 Å), converted into velocity. As in Komossa et al. (2008), I defined an object as a blue outlier when this velocity is $v_{[OIII]} \leq -150$ km s^{-1}. I also defined an object as red outlier when the [O III] line is shifted toward higher wavelengths of the same quantity. Fig. 4.7 shows the distributions of the $\lambda5007$ line velocity shift, the IQR and the average shift values for each sample. The larger IQR in the radio-loud velocity distribution is strictly connected with the number of outliers. In the radio-quiet sample I found only 1 red and 3 blue outliers ($\sim6\%$), while in the radio-loud there are 13 blue outliers and 3 red outliers ($\sim29\%$).

Both in the radio-quiet and radio-loud samples the majority of sources have a typical velocity between -50 and 50 km s^{-1}(41/68 in RQNLS1s, 21/56 in RLNLS1). RLNLS1s show
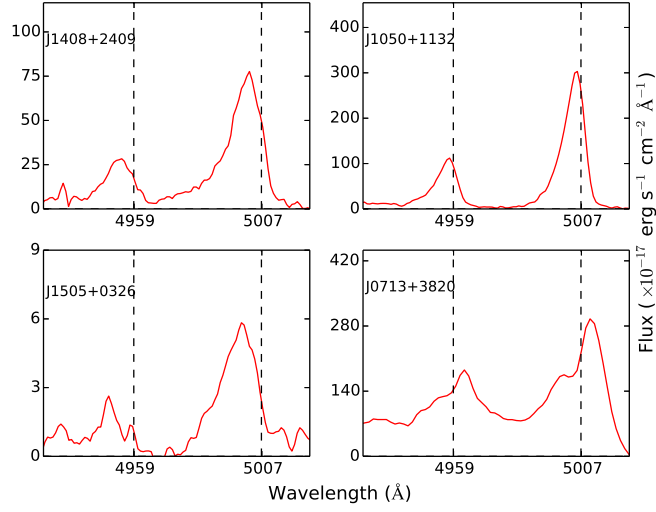
Figure 4.6 Four examples of blue and red outliers in my samples, continuum and Fe II subtracted. The vertical dashed lines are the restframe position of [O III] $\lambda4959$ and $\lambda5007$. Those in the two upper panels are RQNLS1s, while those in the bottom panels are RLNLS1s.
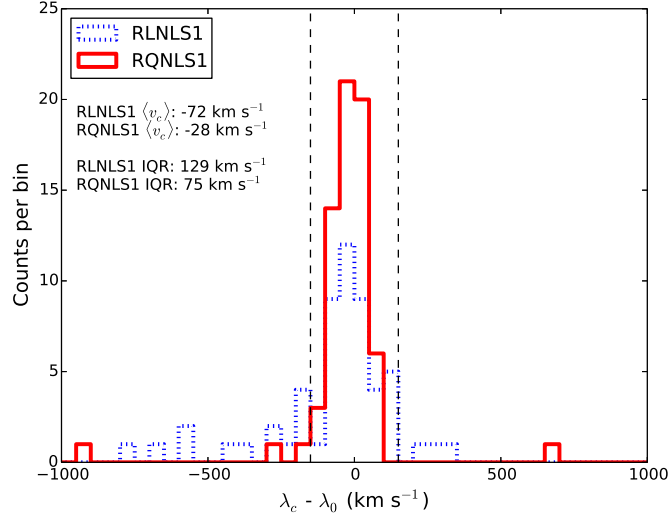
Figure 4.7 Histogram of the peak position of the $\lambda5007$ line in the two samples with respect to [O II]. Binning of 50 km s^{-1}. The dashed vertical lines are the limits of 150 km s^{-1} for blue and red outliers. The red solid line is the RQNLS1s sample, the blue dotted line is the RLNLS1s sample. The values are the IQR, the average shift and the standard deviation, all in km s^{-1}.

a few more redshifted sources, and in general they appear to be distributed over a larger interval of velocities. This is shown by the IQR of the distributions, which is 129 km s^{-1} for RLNLS1s and 75 km s^{-1} in RQNLS1s. RQNLS1s have hence a narrower distribution, and this suggests that the gas is slightly more perturbed in RLNLS1s. I performed an A-D test, finding a p-value of 0.04 which allows me to reject the null hypothesis. This result can be
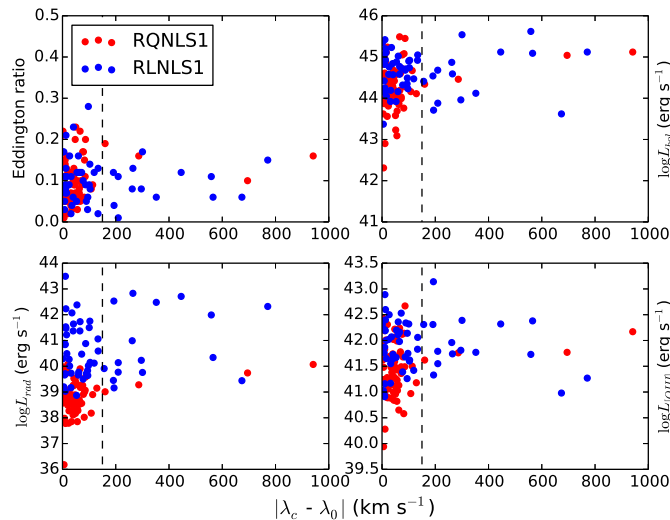
Figure 4.8 Correlations between the absolute value of [O III] velocity shift, in abscissa, and other quantities. **Top left:** Eddington ratio; **Top right:** logarithm of the bolometric luminosity (erg s^{-1}); **Bottom left:** logarithm of radio luminosity at 1.4 GHz (erg s^{-1}); **Bottom right:** logarithm of the [O III] luminosity. The dashed vertical line is the limit for outliers. RQNLS1s are red circles, RLNLS1s are blue squares.

interpreted as a sign that the two distributions are originated via different mechanisms.

The number of outliers is inevitably affected by error measurements. As mentioned before, I calculated the error on both the [O III] line core position and on the [O II] line via MonteCarlo method. By considering both of these errors, all 4 sources in the RQNLS1s sample are still outliers. In RLNLS1s instead the numbers vary between 13 (11 blue, 2 red) and 17 (13-4). The number of outliers is then systematically larger in the radio-loud sample. It is worth noting that the null hypothesis of the A-D test cannot be rejected when only 13 outliers are present in the radio-loud sample (p-value 0.15). Conversely when 17 outliers are considered in the radio-loud sample, the null hypothesis is rejected with a higher confidence level (p-value 4×10^{-3}).

I finally investigated the presence of a correlation between blue outliers and Eddington ratio, to understand whether the shift of [O III] is directly connected with the high accretion rate of NLS1s. This correlation was first found by Marziani et al. (2003) and later confirmed by Bian et al. (2005). Nevertheless, in agreement with Aoki et al. (2005), I did not find any correlation between the Eddington ratio and the blue outliers (see Fig. 4.8). I also tested the correlation between the blue outliers and other significant quantities that might in some way affect the gas kinematics, such as the bolometric luminosity, the radio luminosity and the [O III] luminosity. In particular, a high bolometric luminosity might affect the gas by means of the radiation pressure. In a similar way, the radio luminosity is linked with the relativistic jets properties: if the jet is present they might be connected in some way with the outliers velocity. Finally, a high [O III] luminosity can be connected to the gas dynamics. Again, though, I did not find any significant result, with the lowest p-value being 0.01 in RQNLS1s between the core shift and the radio luminosity ($r = 0.3$).

Nevertheless, I investigated the same correlations considering only the outliers, and I found that, while the radio-loud outliers have the same behavior of the whole sample, radio-quiet
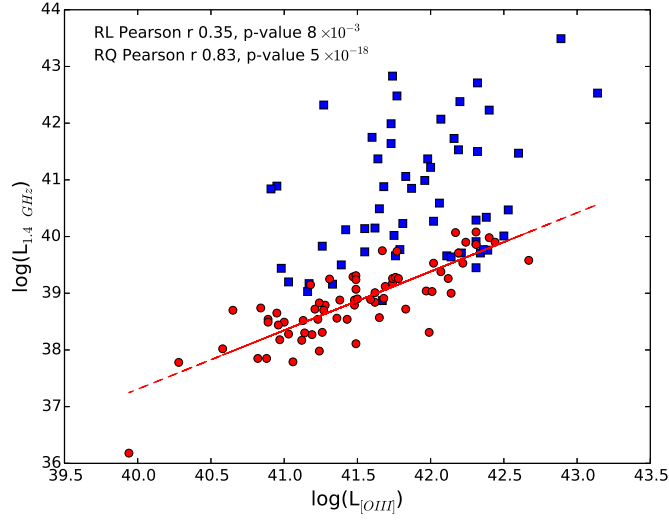
Figure 4.9 [O III] luminosity vs radio luminosity at 1.4 GHz. The solid red line is the best-fit for RQNLS1s. Correlation coefficients for both samples are also shown.

outliers, although they are rare, seem to follow a different trend. In particular, I found a very strong and significant correlation between the radio luminosity and the [O III] core shift ($r = 0.99$, p-value $= 4 \times 10^{-3}$). An equally strong correlation, though less significant, can be found with the bolometric luminosity ($r = 0.98$, p-value $= 0.02$). It is then possible that the radio luminosity has some impact in the formation of outliers not among radio-loud sources ($r = 0.3$, p-value $= 0.32$), but only in RQNLS1s. It is finally worth noting that in RQNLS1s there are no outliers below a radio luminosity of 10^{39} erg s^{-1}, even if 56% of radio-quiet sources lies below that threshold.

4.4.3   Radio vs [O III]

As done for the first time by de Bruyn & Wilson (1978), I searched for a correlation between the luminosity of [O III] and the radio luminosity at 1.4 GHz extracted from FIRST survey. The result is shown in Fig.4.9. It is evident that RQ and RL sources form two distinct populations in the plot. RQNLS1s show a strong correlation between these two quantities ($r = 0.8$, p-value $= 5 \times 10^{-18}$), while in RLNLS1s there is only a trend ($r = 0.4$, p-value $= 8 \times 10^{-3}$). The lack of a strong correlation among radio-loud sources is due to the very large scatter in radio luminosity. The linear best fit relation for the radio-quiet sample can be expressed as

$$\log L_{1.4\,GHz} = (-4.18 \pm 0.47) + (1.04 \pm 0.01) \log L_{[OIII]} \, , \qquad (4.1)$$

with a scatter of 0.2 *dex*. It is worth noting that some radio-loud sources seem to lie close to this relation, and are completely overlapped with the radio-quiet sample.

The [O III] luminosity interval in which my samples are located are different, as confirmed by a K-S test (p-value $= 2 \times 10^{-4}$). This difference is likely to be a selection effect due to the different redshift distributions of my samples. Fig. 4.9 shows how those sources with high radio luminosity, hence visible at high z, also have a high [O III] luminosity. Such line then is particularly bright in radio-loud sources. In NLS1s the [O III] line flux must be, by definition,
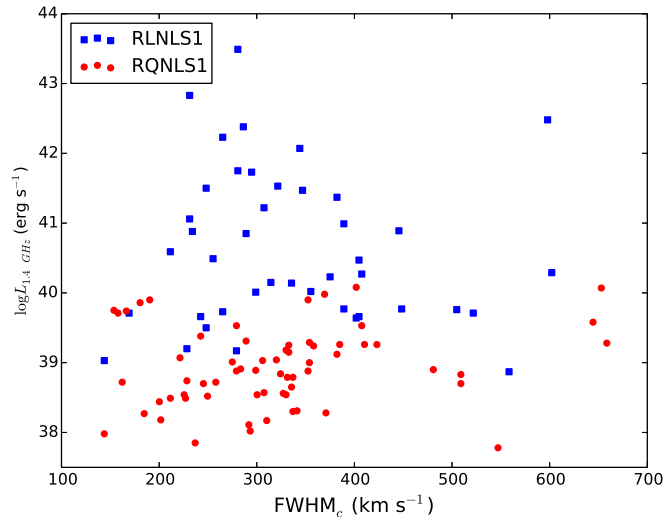
Figure 4.10 FWHM of [O III]$_c$ (in km s^{-1}) against radio luminosity at 1.4 GHz (in erg s^{-1}). RQNLS1s are red circles, RLNLS1s are blue squares.

of the same order of magnitude of Hβ, so the latter must be equally bright. These strong optical lines allow an easier classification of NLS1s: radio-loud NLS1s are more likely to be identified as such in a large survey. This likely induces a selection effect. I indeed expect that at high redshift the relative number of detected RLNLS1s with respect to RQNLS1s increases for this very reason.

It must be highlighted that the number of blue and red outliers might be larger in RLNLS1s because they are tipically at larger redshift. The difference between the samples would therefore be due to evolution, and not to the relativistic jet. Anyway, if this was true, among RLNLS1s I should observe outliers only at high redshift, but exactly half of the outliers are located below z=0.35, which is the upper limit for my radio-quiet sample. Hence the redshift seems not to have a significant incidence on the outliers presence. The same is true for bolometric luminosity and [O III] luminosity which, as shown before, are both not correlated with the shift of [O III], therefore my results might be interpreted as a true physical difference in the NLR of my two samples.

As found for the first time by Pedlar et al. (1985), and recently confirmed by Mullaney et al. (2013), the radio-luminosity has an effect on the [O III] line profile. Therefore I searched for a correlation between the FWHM of the core component of [O III] and the radio luminosity at 1.4 GHz, neglecting those sources in which I could not separate the core and wing components. I did not find such correlation, as shown in Fig. 4.10, with $r = 0.0$, p-value $= 0.8$ in RLNLS1s, and $r = 0.2$ and p-value $= 0.2$ among RQNLS1s.

4.4.4 Ratio [O III]/Hβ

I finally measured the ratio between the [O III] $\lambda5007$ line and the whole Hβ flux, also known as the R5007 parameter. Since the broad Hβ line is formed in the inner part of the BLR (Greene & Ho 2005b), this ratio is a useful tool to evaluate whether the jet/gas interaction is different in BLR and NLR. The histogram with the results is shown in Fig. 4.11. The average
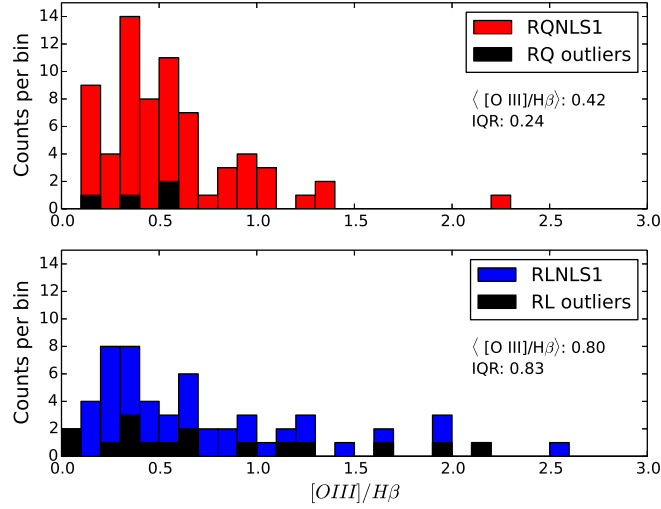
Figure 4.11 Histogram of the distribution of ratio R5007 between [O III] and Hβ. The ratio for blue outliers is indicated by the black histogram. In the top panel the RQNLS1s sample, in the bottom panel the RLNLS1s sample. Binning of 0.1.

of this ratio for radio-quiet sources is 0.42 with an IQR of 0.24, while for radio-loud is 0.80 with IQR 0.83. The difference is not significant, in fact both the K-S and the A-D tests do not reject the null-hypothesis (p-values 0.23 and 0.09, respectively). I also investigated the ratio in the blue outliers, also shown in Fig. 4.11. In the radio-quiet sample all the sources have a R5007 below 0.6, being systematically located in the low ratio region of the histogram, while among radio-loud sources the results are distributed over a larger interval. The mean ratio for radio-quiet blue outliers is 0.42 with IQR 0.24, while in radio-loud the mean is 0.80 with IQR 0.82. Finally, I searched for a correlation between the R5007 and the wing velocity. A fast might indeed be connected with a reduction of the covering factor in the gas clouds, which translates in a reduction of the equivalent width, and of the flux, in the [O III] lines (Ludwig et al. 2012). I found such correlation only in the radio-loud outliers, as shown in Fig. 4.12. While in radio-quiet outliers r = -0.4 and p-value = 0.55, among radio-loud the Pearson coefficient is r = -0.8, with a p-value = 5×10^{-3}. The fastest wings, in radio-loud sources, are therefore found in sources with a low R5007.

4.5   Discussion

4.5.1   Origin of the radio emission

A first clear separation between radio-quiet and radio-loud objects is shown in Fig.4.9. The two population are well separated in the plot, both in radio, by construction, and in [O III] luminosity, as confirmed by the K-S test. Nonetheless, as previously mentioned, the [O III] luminosity difference is likely a selection effect. Conversely, the radio emission is so different that probably has a different origin in the two classes. In the radio-loud sample is likely to be the radio-jet, together with the radio emission coming from the accretion disk, the corona and a strong starburst component (Caccianiga et al. 2015). In radio-quiet sources instead the
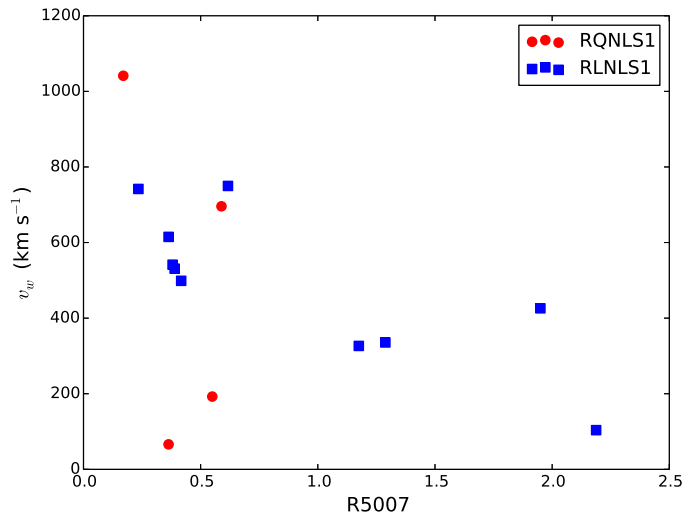
Figure 4.12 Distribution of R5007 against the wing velocity in outliers sources with a visible wing. RQNLS1s are red circles, RLNLS1s are blue squares.

jet is probably absent or very weak (see Sect. 4.5.4). The radio photons are likely thermal radiation originated via bremmsstrahlung and coming from corona and accretion disk, again with a starburst component and, in some cases, also a faint non-thermal radiation (Giroletti & Panessa 2009).

There is a larger intrinsic scatter in radio luminosities for radio-loud sources, proved by the absence of correlation between radio and [O III]. A plausible explanation is again an observational effect: flat-spectrum RLNLS1s are highly variable because of their beamed jet (Foschini et al. 2015). This might indeed significantly alter the radio luminosity of the sources, depending on its activity. It is also worth noting that some of the radio-loud sources are well overlapped with the RQNLS1s distribution. The latter, conversely, have a tight correlation between [O III] and radio luminosity, possibly because their radio emission is less variable. All this might be interpreted as a sign that part of the radio emission, in those radio-loud sources whose distance is small with respect to the radio-quiet best-fit line, might have the same origin as that of RQNLS1s. Ten of them in particular are distant less than 1σ from the best-fit line, and 8 of these 10 were investigated by Caccianiga et al. (2015). They found an intense star formation, above 20 $M_\odot$/yr, in 6 of them, and suggested that in such sources star formation might be responsible for a large fraction, or even all, of the radio photons.

4.5.2   [O III] lines properties

The blue wings distribution seems to be roughly the same in the two samples, with on average slightly bluer wings in radio-loud sources. This result is expected if the blue wings always originate in outflows, whose velocity is similar in radio-loud and in radio-quiet sources. In those sources harboring a relativistic jet, admitting that an energy transfer occurs between the jet and the NLR medium, the bulk of the gas is accelerated. In this way the two [O III] components, core and wing, are both blue-shifted but they mantain the same relative velocity. This acceleration process might also explain the significantly larger ($\sim$2 times larger) velocity

Table 4.3 Blue outliers and blue wings in γ-ray emitters from Foschini et al. (2015), calculated with respect to narrow Hβ. Columns: (1) Name of the source; (2) velocity of the [O III]$\lambda5007$ core component (km s^{-1}); (3) FWHM of the core component (km s^{-1}); (4) shift of the blue wing with respect to the core component (km s^{-1}); (5) FWHM of the blue wing (km s^{-1}).

Name	v_c	FWHM$_c$	v_w	FWHM$_w$
J0324+3410	-7.96$\pm$79.04	445.59$\pm$116.76	-123.73$\pm$565.83	1201.40$\pm$341.90
J0849+5108	264.47$\pm$10.78	231.26$\pm$8.98	-498.77$\pm$74.25	703.64$\pm$50.30
J0948+0022	-770.79$\pm$62.87	1438.29$\pm$55.69	–	–
J1102+2239	-565.41$\pm$21.56	879.90$\pm$11.38	-749.79$\pm$164.06	1319.85$\pm$83.23
J1246+0238	39.94$\pm$20.96	382.14$\pm$20.36	-503.49$\pm$136.52	1245.11$\pm$70.06
J1505+0326	-352.25$\pm$59.28	597.88$\pm$60.48	-326.51$\pm$317.35	1180.25$\pm$131.13
J1644+2619	-9.76$\pm$26.35	145.24$\pm$9.58	–	–

IQR in the radio-loud blue wings.

Blue outliers are instead more common in the radio-loud than in the radio-quiet sample. Their number is systematically larger regardless of the errors. The simplest explanation for this is that the gas in the NLR of RLNLS1s is often turbulent, possibly because of the interaction between the relativistic jet and the medium. Nonetheless, it must be underlined that the interaction with the NLR does not necessarily occur every time that the jet is present. Some worth examples are the three RLNLS1s investigated by Richards & Lister (2015). None of them is an outlier, even if they show alternatively very fast or turbulent blue wings. This interpretation is strengthened by the absence of correlation between radio luminosity and blue outliers in radio-loud sources. While blue outliers are more common among radio-loud sources, apparently a large radio luminosity does not automatically imply a shift in the [O III] core. An interesting possibility can involve the age of NLS1s: if some of these sources have really young jets, the NLR has been interacting with them for a short time, and therefore the influence over its kinematic might be still negligible.

4.5.3   Jet/NLR interaction

Another sign that interactions are effectively ongoing in RLNLS1s is the [O III]/Hβ ratio shown in Fig.4.11. A strong outflow can indeed reduce the equivalent width of the lines by reducing the covering factor of the NLR clouds (Ludwig et al. 2012). This decreases the [O III] flux. The Hβ line, coming mostly from the inner part of the BLR, remains instead roughly constant. The ratio should therefore be lower in those sources where the jet interacts with the NLR, forming several fast outflows which decrease the [O III] flux.

My data seem to reveal that the R5007 distribution in both samples is the same (A-D test p-value 0.09). I found that 10 out of 16 radio-loud outliers (63%), both blue and red, have a R5007 below the average of their sample. Among radio-quiet sources instead 2 out of 4 outliers are below the sample average (50%). Assuming that this difference is real, that is the mechanism reducing the covering factor is not the same in the two samples, this might suggest that the mechanism active in radio-quiet sources is slightly less efficient than the relativistic jet of RLNLS1s. Of course this result must be taken with care, since I are dealing with low numbers.

An evident example for the covering factor reduction is J0948+0022. This source was the first γ-ray NLS1 discovered (Abdo et al. 2009a), and it harbors a relativistic beamed jet. Its spectrum barely shows the $\lambda5007$ line, and therefore the ratio of [O III]/Hβ is only an upper limit. Anyway, as showed before, some RLNLS1s do not exhibit any significant [O III] flux

and equivalent width reduction. Interestingly I found that all these sources are those showing relatively slow wings in their line profile, while this statement is not true for the two radio-quiet outliers. I indeed tested the correlation between R5007 against the wing velocity, when the latter could be measured. The correlation is present only in RLNLS1s (see Fig. 4.12), and this might indicate that in RLNLS1s only sources with a fast outflowing gas show the [O III] covering factor reduction. The different behavior of RQNLS1s might be another hint that the origin of the gas turbulence within the NLR is different.

Hence the NLR of these objects is possibly slightly less perturbed than in other radio-loud blue outliers. This might be due to the lack of interaction processes between the jet and the medium. If NLS1s are young sources, it is indeed possible that the [O III] covering factor is not yet affected by the jet moving through the NLR. This possibility anyway opens a new question: how does the interaction occur?

An interesting hypothesis regarding the nature of the interaction can be found by Morganti et al. (2015), and also in the simulations ran by Wagner & Bicknell (2011) and Wagner et al. (2012). The jet strongly affects the behavior of the clumpy gas, by following the least resistance path through the clouds and accelerating them in many directions. Around the jet axis a dense and turbulent gas cocoon is formed, that later moves away from the axis and gets dispersed. This increases the turbulence and hence the width of the lines. Since in NLS1s the line of sight is close to the NLR axis, the gas acceleration toward the outer regions appears as a blueshift that should affect all the forbidden lines of the NLR. All these effects should be particularly evident in all the high ionization lines: according to the stratification model (Osterbrock 1991), the clouds where they form are the first to interact with the jet. This is particularly true in the [O III] lines case, being the strongest high ionization lines in the optical spectrum. Wagner et al. (2012) showed that the interaction is active only if the ratio between the jet power and the Eddington luminosity of the black hole is high enough ($\log(P_j/L_{Edd}) > -4$). The outliers in my sample whose jet power is known (see Foschini et al. 2015) always respect this condition. This is in agreement with the perturbed NLR I observe, and it seems to provide an observational confirmation of their results.

Nevertheless, this model still has some issues. Some flat-spectrum RLNLS1s are actually extremely compact, with a typical size below 1 pc. Such small sizes indicate that these sources have not developed radio-lobes, and then the chances for an ongoing interaction seem to reduce. Anyway, I speculate that there is a reasonable mechanism that might allow the jet/NLR feedback in absence of radio-lobes. As suggested by Cavaliere & D'Elia (2002) for blazars, the jet engine might be a combination of the Blandford-Znajek (BZ) and the Blandford-Payne (BP) mechanisms (Blandford & Znajek 1977; Blandford & Payne 1982). Also in the case of NLS1s, the BZ alone is not enough to explain the observed jet power (Foschini 2011a). Therefore, the BP is likely providing the required additional power. Since the BP, as mentioned in Sect. 1.4.5, is essentially a centrifugally driven wind that becomes more efficient when the accretion luminosity is high, it can significantly contribute to the acceleration of the gas in the NLR, even in absence of radio-lobes. The wind can be generated only if the poloidal component of the magnetic field forms an angle lower than $60°$ with the disk plane. If this condition is not matched, the jet is not launched and the source might appear as radio-quiet. Despite this, the disk is still able to produce strong winds, that in the most luminous sources can generate outliers.

In my radio-loud sample there are 7 γ-ray emitters (Foschini et al. 2015; D'Ammando et al. 2015), and four of them are outliers (three blue, one red). These results are shown in Tab. 4.3. In two of the remaining sources, J0324+3410 and J1246+0238, the [O III] lines are

not particularly shifted, but their blue wings have a high FWHM, indicating again a very strong internal turbulence. Therefore even if the numbers are still quite low, more than half of the γ-ray emitters are also outliers, and this might suggest a connection between these two phenomena.

4.5.4 Radio-quiet vs radio-loud

All my findings seem to point out that a relativistic jet has a strong influence on the NLR. The radio-loud sources, and particularly the γ-ray emitters, show indeed a strongly disturbed NLR kinematics. In radio-quiet sources the NLR is also perturbed, but the number of blue outliers among them is significantly lower. I speculate that a possible way to account for the differences I found between radio-quiet and radio-loud NLS1s is the BP mechanism. In NLS1s, without the decisive contribution of the BP, the jet is not launched (see Sect. 4.5.1). Nevertheless this mechanism can actually provide a contribution to the collimation only if the critical angle criterium is met. In RQNLS1s the poloidal component of the magnetic field might have a high inclination, and therefore the disk can only form a jet-base. Being a pressure driven structure, the jet-base cannot accelerate the plasma particles to relativistic speed, but only to moderate velocities. Therefore a non-relativistic wind is present, that only in the most luminous sources is powerful enough to affect the kinematic of the whole NLR. In general, instead, this outflowing wind might be the region where blue wings are formed. This mechanism is in agreement with the correlation I observe between outliers and radio luminosity. a high radio luminosity might indicate the presence of a strong jet-base, which might be more effective in perturbing the gas dynamics. The same mechanism can explain the presence of the wings in all Seyfert galaxies: both Seyfert 1 and 2 show indeed this feature in their [O III] lines.

In RLNLS1s, instead, the condition on the critical angle is typically met. Therefore the poloidal component of the magnetic field accelerates the particles, and it forms at the same time the relativistic jet and the surrounding wind. The accretion disk of NLS1s is luminous enough to be in the radiation pressure dominated regime in which radiative instability occurs (Moderski & Sikora 1996; Ghosh & Abramowicz 1997; Czerny et al. 2009; Wu 2009a; Foschini 2011a). This instability might translate into a change in angle, and then in an intermittent BP contribution to the jet. The strong winds are anyway always present, and being directed along the jet axis they influence the NLR kinematics even when the jet is not active, providing a large number of outliers.

4.5.5 Implications for the parent population

My results likely provide an important contribution to the search of flat-spectrum RLNLS1s parent population. The hypothesis of Foschini (2011b) was that in RQNLS1s the jet is highly collimated and, since its energy is not dissipated, it is invisible for present-day observatories. If this is true, the dichotomy between radio-quiet and radio-loud NLS1s might be due only to an orientation effect. This might explain why the NLR of RQNLS1s appears to be less perturbed: a possibility is that in RQNLS1s low power jets are present, that do not dissipate their energy for a long time. As previously mentioned, some traces of non thermal radio emission are actually present in some RQNLS1s. In particular Giroletti & Panessa (2009) found this emission in one of my sources, J1203+4431 (NGC 4051). Anyway its flux is quite weak, and it can be explained with a simple jet-base model (Falcke & Biermann 1999), without

invoking a fully developed relativistic jet.

Therefore, since RQNLS1s do not seem to harbor a fully relativistic jet, they may not be considered part of the parent population of radio-loud NLS1s. Of course there might be a few exceptions. Sources that, despite being radio-quiet, actually show a developed radio-jet, do actually exist (i.e. Mrk 1239, Doi et al. 2015). Nevertheless this might happen because, as shown by Ho & Peng (2001), radio-loudness can be a slightly misleading parameter, since it is strongly affected by the way of measuring both the radio and the optical flux. It is also possible that the source activity was relatively low at the time of observation, while the jets were formed in the past, when the BP was active. Therefore radio-quietness for some sources might be a simply temporary condition.

4.6 Summary

In this chapter I investigated the nature of the parent population of flat-spectrum RLNLS1s by means of the [O III] lines properties in two samples of NLS1s, one radio-loud and one radio-quiet. Such study can provide important information on the NLR kinematics and on the interactions between a relativistic jet and its environment. It can finally help me to understand whether a fully developed relativistic jet is present also in RQNLS1s, and therefore whether they belong to the parent population.

I decomposed each [O III] line into two components, one to represent the core and another to represent the wing. The first is dominated by the bulge gravitational potential, while the second is likely generated by outflows coming from the inner NLR. The wings have roughly the same relative velocity in both my samples, and it appears that faster outflows are typically associated with a large internal turbulence. The core component is also affected by the disturbed kinematics of the gas, and this is particularly evident in radio-loud sources, which harbor a relativistic jet. A large fraction of these are in fact blue outliers.

I interpret these results as a hint of an ongoing interaction between the NLR and the relativistic jets in RLNLS1s. The jet likely accelerates the gas in the NLR, generating a large number of blue and red outliers. These appear to be more common among RL than RQNLS1s. Another effect of the jet is the reduction of equivalent width of high ionization lines in blue outliers, that in some cases translates in a reduction of the [O III]/Hβ ratio. Moreover, I also found that there might be a connection between blue outliers and γ-ray emission. Out of seven γ-ray emitting NLS1s included in my sample, I indeed found four outliers.

Since not all RLNLS1s have developed radio-lobes to interact with the medium, I speculate that the interaction might occur also in a different way. The BP mechanism might provide a valid explanation both for the jet/NLR interaction in RLNLS1s, and also for the absence of a fully developed relativistic jet in RQNLS1s. The BP requires a critical angle between the poloidal component of the magnetic field and the disk surface to launch the jet. When this condition is met the source appears as radio-loud, otherwise it appears as radio-quiet. Nevertheless, being the central engine a continuously varying region, a radio-loud source can go through different states of activity, switching off the BP mechanism and producing an intermittent jet. This mechanism can produce strong winds even when the jet is off. In this way, the NLR kinematics can be perturbed even if radio-lobes are not present. Finally, it can also account for the outflows where blue wings are originated. In few cases, these outflows are powerful enough to produce blue outliers even without a jet.

If this hypothesis is correct, RQNLS1s do not harbor a fully developed relativistic jet,

but only a jet-base that can account for the faint non-thermal radio emission observed in these sources. Hence they might not be included in the parent population of flat-spectrum RLNLS1s. Future studies are needed to deeply investigate the innermost region of RQNLS1s, to confirm the absence of the relativistic jet. For this purpose, new generation instruments as JVLA or SKA can help to deeply investigate the matter (see Chapter 6).

Table 4.4: Summary of the sources intrinsic properties in RQNLS1s. Columns: (1) Short name; (2) right ascension; (3) declination; (4) redshift; (5) logarithm of the black hole mass; (6) Eddington ratio; (7) logarithm of the Hβ luminosity; (8) logarithm of the radio luminosity at 1.4 GHz.

Short Name	R.A.	Dec.	z	logM$_{BH}$	Edd	log L(Hβ)	log L_{rad}
J0306+0003	03h06m39.58s	+00d03m43.2	0.107	7.18	0.12	41.91	39.12
J0632+6340	06h32m47.16s	+63d40m52.1	0.013	6.48	0.02	40.52	37.78
J0736+3926	07h36m23.13s	+39d26m17.7	0.118	7.69	0.17	42.55	39.26
J0751+2914	07h51m01.42s	+29d14m19.1	0.121	7.38	0.17	42.23	38.91
J0752+2617	07h52m45.60s	+26d17m35.7	0.082	7.16	0.09	41.78	38.49
J0754+3920	07h54m00.05s	+39d20m29.1	0.096	8.04	0.20	42.93	39.58
J0804+3853	08h04m09.24s	+38d53m48.8	0.211	7.72	0.14	42.48	39.71
J0818+3834	08h18m49.26s	+38d34m16.1	0.160	6.98	0.12	41.71	39.31
J0836+1554	08h36m15.37s	+15d54m09.8	0.206	7.34	0.09	41.95	39.29
J0913+3658	09h13m13.72s	+36d58m17.2	0.107	7.01	0.06	41.49	38.54
J0925+5217	09h25m12.87s	+52d17m10.5	0.035	7.51	0.10	42.13	38.31
J0926+1244	09h26m03.25s	+12d44m04.1	0.029	7.31	0.04	41.56	38.30
J0936−0026	09h36m09.13s	−00d26m39.7	0.141	6.94	0.07	41.49	38.72
J0948+5029	09h48m42.67s	+50d29m31.4	0.056	7.02	0.07	41.52	38.79
J0957+2433	09h57m07.16s	+24d33m16.1	0.082	6.98	0.09	41.59	38.56
J0958+5602	09h58m33.94s	+56d02m24.4	0.216	7.42	0.05	41.74	39.18
J1016+4210	10h16m45.11s	+42d10m25.5	0.055	7.14	0.08	41.71	38.18
J1022+2022	10h22m58.20s	+20d22m37.9	0.130	7.41	0.03	41.62	38.70
J1025+5140	10h25m31.28s	+51d40m34.9	0.045	7.16	0.07	41.64	37.85
J1036+4125	10h36m04.66s	+41d25m17.8	0.120	7.05	0.05	41.46	38.79
J1050+1132	10h50m07.75s	+11d32m28.6	0.133	7.81	0.15	42.58	39.00
J1103+0834	11h03m33.00s	+08d34m49.0	0.163	7.10	0.06	41.55	39.24
J1112+4541	11h12m39.56s	+45d41m41.3	0.136	6.94	0.19	41.88	39.01
J1120+0633	11h20m14.85s	+06d33m41.1	0.316	7.36	0.22	42.33	39.90
J1121+5351	11h21m08.59s	+53d51m21.1	0.103	7.64	0.13	42.37	39.03
J1128+1023	11h28m13.02s	+10d23m08.3	0.050	6.91	0.07	41.43	37.98
J1136+3432	11h36m55.95s	+34d32m37.0	0.192	7.16	0.23	42.16	39.38
J1149+0448	11h49m54.98s	+04d48m12.8	0.270	7.94	0.10	42.54	39.74
J1155+1507	11h55m23.74s	+15d07m56.9	0.287	7.79	0.16	42.61	39.86
J1203+4431	12h03m09.69s	+44d31m52.5	0.002	6.30	0.01	39.97	36.18
J1207−0219	12h07m00.30s	−02d19m27.1	0.308	7.45	0.13	42.20	39.53
J1209+3217	12h09m45.20s	+32d17m01.1	0.144	7.48	0.10	42.13	39.26
J1215+5442	12h15m49.44s	+54d42m24.0	0.150	7.51	0.10	42.13	39.26
J1218+1834	12h18m30.84s	+18d34m58.2	0.197	7.77	0.11	42.43	39.04
J1218+2948	12h18m26.48s	+29d48m46.2	0.013	6.43	0.05	40.90	38.31
J1242+3317	12h42m10.61s	+33d17m02.6	0.044	7.06	0.06	41.52	38.57
J1246+0222	12h46m35.25s	+02d22m08.8	0.048	7.09	0.05	41.49	38.17
J1311+0648	13h11m56.15s	+06d48m58.3	0.128	7.11	0.11	41.82	39.07
J1315+4325	13h15m10.07s	+43d25m47.0	0.086	6.85	0.08	41.41	38.70
J1320+2108	13h20m46.67s	+21d08m46.4	0.090	7.06	0.05	41.44	38.65
J1322+0809	13h22m55.43s	+08d09m41.6	0.050	7.20	0.06	41.61	38.74

J1331+0131	13h31m38.03s	+01d31m51.6	0.080	6.82	0.05	41.20	38.83
J1332+3127	13h32m05.28s	+31d27m36.4	0.090	7.25	0.11	41.96	39.25
J1337+2423	13h37m18.72s	+24d23m03.4	0.108	8.04	0.22	42.97	39.90
J1342+0505	13h42m06.56s	+05d05m23.8	0.266	7.80	0.16	42.61	40.07
J1342+4642	13h42m43.57s	+46d42m24.0	0.086	6.90	0.07	41.45	38.52
J1355+5612	13h55m16.56s	+56d12m44.6	0.122	7.14	0.20	42.08	39.53
J1358+2511	13h58m52.00s	+25d11m40.2	0.089	7.29	0.06	41.74	38.88
J1402+1720	14h02m59.03s	+17d20m56.0	0.060	6.60	0.07	41.16	38.44
J1402+2159	14h02m34.44s	+21d59m51.5	0.066	7.15	0.11	41.84	38.11
J1406+2223	14h06m21.89s	+22d23m46.5	0.098	7.60	0.09	42.19	38.90
J1408+2409	14h08m27.82s	+24d09m24.6	0.130	7.15	0.16	41.99	39.28
J1439+3923	14h39m52.91s	+39d23m58.9	0.112	7.23	0.05	41.56	38.88
J1440+6156	14h40m12.74s	+61d56m33.0	0.275	7.93	0.21	42.84	39.98
J1441+1604	14h41m56.56s	+16d04m21.1	0.113	7.07	0.07	41.61	38.89
J1442+2623	14h42m40.79s	+26d23m32.5	0.107	7.10	1.22	41.66	39.15
J1444+1536	14h44m31.62s	+15d36m43.2	0.050	6.89	0.05	41.27	38.54
J1448+3559	14h48m25.09s	+35d59m46.6	0.113	7.57	0.07	42.05	38.84
J1451+2709	14h51m08.76s	+27d09m26.9	0.065	7.32	0.15	42.13	38.72
J1536+5433	15h36m38.39s	+54d33m33.2	0.039	7.34	0.09	41.96	37.79
J1537+4942	15h37m32.62s	+49d42m47.7	0.280	7.36	0.12	42.07	39.75
J1555+1911	15h55m07.92s	+19d11m32.4	0.035	6.50	0.03	40.80	37.85
J1559+3501	15h59m09.63s	+35d01m47.5	0.031	6.86	0.06	41.33	38.02
J1605+3239	16h05m08.87s	+32d39m21.4	0.091	7.13	0.02	41.15	38.49
J1627+4736	16h27m50.54s	+47d36m23.5	0.262	8.03	0.12	42.73	40.08
J2140+0025	21h40m54.55s	+00d25m38.1	0.084	7.16	0.12	41.88	38.27
J2219+1207	22h19m18.53s	+12d07m53.1	0.081	6.92	0.06	41.38	38.54
J2254+0046	22h54m52.22s	+00d46m31.3	0.091	7.06	0.06	41.51	38.28

Table 4.5: Summary of the sources intrinsic properties in RLNLS1s. Columns as in Table 4.4.

Short Name	R.A.	Dec.	z	$\log M_{BH}$	Edd	$\log L(\mathrm{H}\beta)$	$\log L_{rad}$
J0138+1321	01h38m59.33s	+13d21m08.2	0.243	7.49	0.09	42.11	40.27
J0146−0040	01h46m44.82s	-00d40m43.1	0.083	7.32	0.07	41.79	39.03
J0251−0702	02h51m05.28s	-07d02m30.1	0.327	7.54	0.12	42.25	40.47
J0324+3410	03h24m41.16s	+34d10m45.8	0.061	7.67	0.03	41.73	40.89
J0706+3901	07h06m25.15s	+39d01m51.6	0.086	7.04	0.04	41.34	39.16
J0713+3820	07h13m40.29s	+38d20m40.1	0.123	8.20	0.17	43.02	39.76
J0804+3853	08h04m09.24s	+38d53m48.8	0.211	8.00	0.09	42.57	39.71
J0806+7248	08h06m38.96s	+72d48m20.4	0.098	6.94	0.08	41.52	40.23
J0814+5609	08h14m32.11s	+56d09m56.6	0.509	8.44	0.11	43.09	41.99
J0849+5108	08h49m57.97s	+51d08m29.0	0.584	7.37	0.13	42.12	42.83
J0850+4626	08h50m01.17s	+46d26m00.5	0.524	7.83	0.09	42.41	41.50
J0902+0443	09h02m27.16s	+04d43m09.5	0.532	7.70	0.12	42.39	42.38
J0937+3615	09h37m09.02s	+36d15m37.1	0.179	7.58	0.05	41.96	39.66
J0948+0022	09h48m57.31s	+00d22m25.4	0.585	7.82	0.15	42.62	42.32
J0952−0136	09h52m19.17s	-01d36m44.1	0.020	7.13	0.05	41.37	38.87
J0953+2836	09h53m17.09s	+28d36m01.5	0.658	8.51	0.04	42.72	42.07
J1031+4234	10h31m23.73s	+42d34m39.3	0.379	8.46	0.02	42.43	41.06
J1034+3938	10h34m38.60s	+39d38m27.8	0.043	6.03	0.17	40.97	39.20
J1037+0036	10h37m27.45s	+00d36m35.6	0.595	7.48	0.14	42.25	41.75
J1038+4227	10h38m59.58s	+42d27m42.2	0.220	7.88	0.08	42.42	40.15
J1047+4725	10h47m32.68s	+47d25m32.0	0.798	8.39	0.08	42.90	43.49
J1048+2222	10h48m16.58s	+22d22m39.0	0.330	7.53	0.11	42.20	39.77
J1102+2239	11h02m23.39s	+22d39m20.7	0.453	8.17	0.06	42.59	40.34
J1110+3653	11h10m05.03s	+36d53m36.3	0.630	7.09	0.23	42.10	41.64
J1133+0432	11h33m20.91s	+04d32m55.1	0.248	7.28	0.12	42.04	40.12
J1138+3653	11h38m24.54s	+36d53m27.1	0.356	7.61	0.09	42.20	40.88
J1146+3236	11h46m54.28s	+32d36m52.3	0.465	8.18	0.07	42.60	41.22
J1200−0046	12h00m14.08s	-00d46m38.7	0.210	7.81	0.08	42.33	40.85
J1227+3214	12h27m49.14s	+32d14m58.9	0.137	6.84	0.16	41.71	39.66
J1238+3942	12h38m52.12s	+39d42m27.8	0.623	6.82	0.44	42.10	41.37
J1246+0238	12h46m34.65s	+02d38m09.0	0.363	7.94	0.06	42.35	41.37
J1302+1624	13h02m58.77s	+16d24m27.6	0.067	7.36	0.12	42.08	39.45
J1305+5116	13h05m22.74s	+51d16m40.2	0.788	8.20	0.67	43.58	42.53
J1333+4141	13h33m45.47s	+41d41m27.7	0.225	7.92	0.05	42.23	39.71
J1337+6005	13h37m24.32s	+60d05m41.7	0.234	6.67	0.28	41.78	40.02
J1346+3121	13h46m34.97s	+31d21m33.7	0.246	7.20	0.10	41.86	39.50
J1358+2658	13h58m45.38s	+26d58m08.5	0.331	7.84	0.12	42.52	39.77
J1409+5656	14h09m14.35s	+56d56m25.7	0.239	7.78	0.03	41.89	39.83
J1432+3014	14h32m44.91s	+30d14m35.3	0.355	7.48	0.21	42.43	41.47
J1435+3131	14h35m09.49s	+31d31m47.8	0.502	7.56	0.12	42.28	41.73
J1443+4725	14h43m18.56s	+47d25m56.7	0.706	7.93	0.12	42.62	42.71
J1450+5919	14h50m41.93s	+59d19m36.9	0.202	7.04	0.11	41.74	39.73

J1505+0326	15h05m06.47s	+03d26m30.8	0.409	7.26	0.06	41.70	42.48
J1507+4453	15h07m40.92s	+44d53m31.5	0.314	7.45	0.16	42.28	40.01
J1358+2658	13h58m45.38s	+26d58m08.4	0.331	7.62	0.19	42.52	39.77
J1548+3511	15h48m17.92s	+35d11m28.0	0.479	7.96	0.13	42.69	42.23
J1608+0708	16h08m31.56s	+07d08m18.2	0.153	7.62	0.02	41.49	39.17
J1612+4219	16h12m59.83s	+42d19m40.3	0.234	6.68	0.41	41.97	39.91
J1629+4007	16h29m01.30s	+40d07m59.9	0.272	7.83	0.13	42.55	40.59
J1633+4718	16h33m23.58s	+47d18m58.9	0.116	6.91	0.11	41.61	40.49
J1634+4809	16h34m01.94s	+48d09m40.2	0.495	7.86	0.08	42.38	40.99
J1644+2619	16h44m42.53s	+26d19m13.2	0.145	6.95	0.11	41.68	40.84
J1703+4540	17h03m30.38s	+45d40m47.1	0.060	7.73	0.01	41.44	40.14
J1709+2348	17h09m07.80s	+23d48m37.6	0.254	7.57	0.06	42.03	39.64
J1713+3523	17h13m04.46s	+35d23m33.5	0.084	6.69	0.06	41.20	39.44
J1722+5654	17h22m06.03s	+56d54m51.6	0.426	7.89	0.09	42.44	41.53
J2314+2243	23h14m55.89s	+22d43m25.7	0.169	8.00	0.17	42.82	40.29

Table 4.6: Summary of the [O III] line properties for RQNLS1s. Columns: (1) Short name of the source; (2) logarithm of the [O III] luminosity (erg s^{-1}); (3) wavelength of the [O III] core component (Å); (4) shift of the [O III] core with respect to the restframe wavelength (km s^{-1}); (5) FWHM of the [O III] core component (km s^{-1}); (6) wavelength of the [O III] wing component (Å); (6) velocity of the [O III] wing component with respect to the core (km s^{-1}); FWHM of the wing component (km s^{-1}). Sources marked with an asterisk are those where the redshift is calculated with respect to Hβ narrow.

Short Name	$\log L_{[OIII]}$	λ_c	v$_c$	FWHM$_c$	λ_w	v$_w$	FWHM$_w$
J0306+0003	41.69	5007.32±0.08	28.56±4.79	382.14±4.79	5003.32±0.43	-239.25±28.74	926.43±13.77
J0632+6340*	40.28	5007.03±0.22	11.20±13.17	547.12±4.19	5002.18±3.92	-290.47±242.50	999.76±115.56
J0736+3926	42.12	5008.11±0.09	75.86±5.39	423.03±2.40	5002.51±0.26	-335.12±19.76	633.13±5.39
J0751+2914	41.68	5005.53±0.09	-78.62±5.39	283.43±4.79	4999.94±0.27	-334.93±19.76	987.06±15.57
J0752+2617	41.00	5006.13±0.06	-42.69±3.59	227.02±2.40	5001.64±0.31	-268.66±20.36	720.56±8.98
J0754+3920	42.67	5005.40±0.07	-86.40±4.19	644.41±2.99	4993.81±0.40	-694.39±26.35	468.15±17.96
J0804+3853	42.19	5007.01±0.04	10.00±2.40	157.93±1.20	5000.52±0.15	-388.22±9.58	760.04±3.59
J0818+3834	41.49	5006.04±0.08	-48.08±4.79	289.07±4.19	5000.76±0.61	-316.14±39.52	820.67±14.97
J0836+1554	41.47	5006.07±0.16	-46.28±9.58	353.93±9.58	4999.59±0.59	-388.32±43.11	795.29±11.38
J0913+3658	41.43	5005.90±0.08	-56.46±4.79	329.96±5.39	5000.78±0.32	-306.62±22.15	799.52±7.78
J0925+5217	41.99	5007.78±0.53	56.10±31.73	215.74±1.80	−	−	−
J0926+1244*	41.14	5006.32±0.61	-31.32±36.52	337.01±31.73	5005.00±0.96	-79.02±92.21	846.06±32.93
J0936−0026	41.21	5006.35±0.16	-29.52±9.58	258.05±16.77	5001.99±0.32	-261.29±26.94	1050.52±10.78
J0948+5029	41.48	5006.74±0.05	-6.17±2.99	337.01±1.80	5001.76±0.17	-298.60±11.38	868.62±5.39
J0957+2433	41.36	5005.64±0.06	-72.03±3.59	327.14±2.40	5001.11±0.27	-271.66±17.96	958.86±9.58
J0958+5602	41.74	5007.96±0.07	66.88±4.19	329.96±6.59	5005.26±0.71	-161.79±44.91	1026.55±62.87
J1016+4210	40.97	5005.04±0.06	-107.96±3.59	201.64±2.99	5002.30±0.59	-164.08±37.72	813.62±28.14
J1022+2022	41.27	5006.25±0.19	-35.51±11.38	245.36±20.36	5004.56±0.80	-101.08±57.48	592.24±55.69
J1025+5140	40.88	5006.28±0.10	-33.71±5.99	236.90±6.59	5003.10±0.85	-190.64±55.09	760.04±56.88
J1036+4125	41.28	5006.52±0.06	-19.34±3.59	331.37±4.19	5002.57±0.75	-236.81±46.70	1033.60±22.15
J1050+1132	42.14	5005.46±0.10	-82.81±5.99	353.93±4.19	5000.81±0.27	-278.44±19.76	717.74±8.38
J1103+0834	41.49	5005.64±0.15	-72.03±8.98	358.16±13.77	5000.82±0.52	-289.04±38.32	886.95±16.17
J1112+4541	41.62	5004.17±0.06	-160.05±3.59	274.97±1.80	5000.96±0.14	-192.49±9.58	981.42±5.99
J1120+0633	42.44	5006.81±0.04	-1.98±2.40	190.36±1.20	5006.32±0.07	-29.64±4.19	678.25±4.19

J1121+5351	42.01	5007.09±0.06	14.79±3.59	305.99±2.99	5003.61±0.15	-208.07±10.78	734.66±4.79
J1128+1023	41.24	5006.97±0.04	7.60±2.40	143.83±1.20	5001.36±0.08	-335.46±5.39	679.66±2.40
J1136+3432	42.07	5006.01±0.04	-49.88±2.40	242.54±1.20	5004.29±0.09	-102.62±6.59	781.19±5.39
J1149+0448*	41.77	5018.45±0.17	694.99±10.18	166.39±70.06	5001.02±0.24	-1041.24±22.75	1191.53±5.39
J1155+1507	42.31	5007.11±0.08	15.99±4.79	180.49±4.79	5000.46±0.14	-398.26±11.38	943.35±4.79
J1203+4431	39.94	5006.94±0.45	5.81±26.94	318.68±5.99	5002.02±0.91	-294.61±59.88	606.34±81.43
J1209+3217*	41.74	5006.17±0.19	-40.30±11.38	410.34±6.59	5002.46±0.24	-221.92±23.95	1405.86±12.57
J1207−0219	42.02	5006.13±0.10	-42.69±5.99	279.20±5.39	4999.33±0.21	-407.22±16.77	1125.25±7.19
J1215+5442	41.78	5005.69±0.16	-69.04±9.58	384.96±7.19	4997.34±0.58	-500.47±42.51	661.33±15.57
J1218+1834	41.97	5006.93±0.07	5.21±4.19	320.09±7.78	5003.66±0.33	-195.68±22.15	853.11±11.38
J1218+2948	41.26	5007.70±0.38	51.31±22.75	341.24±2.40	5005.81±0.47	-113.22±50.90	774.14±6.59
J1242+3317	41.65	5006.86±0.04	1.02±2.40	307.40±1.20	5003.30±0.10	-213.29±6.59	888.36±2.99
J1246+0222	41.12	5006.03±0.07	-48.68±4.19	310.22±3.59	5002.24±0.49	-227.11±31.73	738.89±13.77
J1311+0648	41.49	5005.42±0.07	-85.20±4.19	221.38±4.19	5003.40±0.21	-121.05±14.37	671.20±10.78
J1315+4325	40.65	5005.79±0.82	-63.05±49.10	509.04±59.28	4995.20±3.12	-633.88±234.12	619.03±144.90
J1320+2108	40.95	5006.66±0.24	-10.96±14.37	335.60±31.14	5002.50±1.16	-249.42±82.03	934.89±24.55
J1322+0809	40.84	5006.10±0.15	-44.49±8.98	228.44±9.58	5002.08±0.50	-240.60±37.12	619.03±16.77
J1331+0131	41.24	5006.92±0.06	4.61±3.59	509.04±1.80	4994.90±0.53	-719.78±34.13	337.01±19.16
J1332+3127	41.31	5007.55±0.18	42.33±10.78	332.78±13.77	4999.67±0.68	-471.48±50.30	905.28±17.36
J1337+2423	42.24	5005.74±0.25	-66.04±14.97	352.52±16.17	4995.76±1.29	-597.81±90.41	2240.64±25.75
J1342+0505	42.17	4991.12±0.21	-941.44±12.57	652.87±14.37	4990.02±0.30	-66.05±28.74	2322.42±19.16
J1342+4642	41.13	5005.79±0.14	-63.05±8.38	249.59±9.58	5001.91±0.93	-232.37±61.67	644.41±27.54
J1355+5612	42.22	5007.64±0.04	47.72±2.40	407.52±1.20	5003.83±0.10	-228.43±7.19	1013.86±3.59
J1358+2511	41.48	5007.41±0.07	33.95±4.19	279.20±3.59	5002.30±0.14	-306.09±10.78	884.13±4.19
J1402+1720	40.96	5006.00±0.05	-50.48±2.99	200.23±2.40	5003.49±0.20	-150.30±13.17	844.65±10.78
J1402+2159	41.49	5006.18±0.05	-39.70±2.99	291.89±1.80	5003.45±0.13	-163.17±8.98	762.86±5.39
J1406+2223	41.50	5004.95±0.24	-113.35±14.37	480.84±29.94	4996.79±0.52	-488.83±43.71	822.08±20.36
J1408+2409	41.76	5002.06±0.11	-286.39±6.59	658.51±5.99	4990.45±0.60	-695.89±41.31	1448.17±19.16
J1439+3923	41.38	5006.23±0.07	-36.70±4.19	352.52±3.59	4997.06±0.27	-549.34±18.56	1035.01±7.19
J1440+6156	42.40	5006.83±0.07	-0.78±4.19	369.44±4.79	4995.38±0.26	-685.51±17.96	1081.54±7.78
J1441+1604	41.59	5007.63±0.05	47.12±2.99	298.94±2.40	5005.45±0.12	-130.65±7.78	772.73±4.79
J1442+2623	41.18	5004.69±0.33	-128.91±19.76	332.78±24.55	4999.82±0.98	-291.43±76.64	864.39±28.74

J1444+1536	41.23	5007.79±0.08	56.70±4.79	300.35±4.19	5005.54±0.14	-134.24±11.38	611.98±5.39
J1448+3559	41.62	5006.80±0.09	-2.57±5.39	324.32±4.19	5000.94±0.28	-350.60±19.76	731.84±8.38
J1451+2709	41.83	5007.01±0.04	10.00±2.40	162.16±0.60	5003.58±0.10	-205.65±6.59	894.00±3.59
J1536+5433*	41.06	5007.23±0.75	23.17±44.91	455.46±16.17	–	–	–
J1537+4942	41.67	5006.48±0.08	-21.74±4.79	153.70±6.59	5000.77±0.37	-341.82±25.15	837.60±16.17
J1555+1911	40.82	5005.91±0.43	-55.86±25.75	349.70±4.79	–	–	–
J1559+3501	40.58	5005.48±0.07	-81.61±4.19	293.30±3.59	4999.65±0.38	-349.15±25.15	806.57±14.97
J1605+3239	40.89	5007.17±0.55	19.58±32.93	211.51±68.86	5004.47±1.31	-161.39±109.57	651.46±59.28
J1627+4736	42.31	5007.18±0.07	20.18±4.19	401.88±2.40	5001.68±0.19	-329.20±13.77	812.21±4.79
J2140+0025	41.19	5007.25±0.15	24.37±8.98	184.72±11.98	5004.55±0.28	-162.15±23.95	638.77±16.17
J2219+1207	40.89	5007.24±0.08	23.77±4.79	225.61±3.59	5001.95±0.84	-316.71±53.29	547.12±24.55
J2254+0046	41.03	5007.81±0.25	57.90±14.97	370.85±10.18	5000.63±0.66	-429.52±52.69	737.48±25.75

Table 4.7: Summary of the [O III] line properties for RLNLS1s. Columns as in Table 4.6.

Short Name	$\log L_{[OIII]}$	λ_c	v_c	$FWHM_c$	λ_w	v_w	$FWHM_w$
J0138+1321	42.02	5007.26±0.10	24.97±5.99	407.52±5.39	5003.49±0.47	-226.10±32.33	943.35±14.97
J0146−0040	41.16	5006.67±0.05	-10.36±2.99	143.83±4.19	5005.78±0.22	-53.34±14.37	575.32±19.16
J0251−0702	42.53	5005.64±0.07	-72.03±4.19	404.70±5.39	5002.05±0.15	-214.87±11.38	1116.79±5.39
J0324+3410*	40.95	5006.71±1.32	-7.96±79.04	445.59±116.76	5004.64±8.16	-123.73±565.83	1201.40±341.90
J0706+3901	41.33	5003.61±0.07	-193.58±4.19	736.07±2.99	−	−	−
J0713+3820	42.39	5011.86±0.14	300.40±8.38	504.81±12.57	4999.46±0.58	-741.81±41.31	1494.70±17.96
J0804+3853	42.21	5006.67±0.04	-10.36±2.40	169.21±1.20	5001.29±0.20	-322.21±13.17	857.34±7.19
J0806+7248	41.81	5001.90±0.20	-295.97±11.98	375.08±8.98	4994.79±1.49	-426.03±99.40	733.25±61.67
J0814+5609*	41.73	4997.51±0.51	-558.83±30.54	740.30±14.97	−	−	−
J0849+5108	41.74	5011.26±0.18	264.47±10.78	231.26±8.98	5002.93±1.09	-498.77±74.25	703.64±50.30
J0850+4626	42.32	5008.52±0.16	100.41±9.58	248.18±14.97	5005.76±0.52	-164.70±38.92	1558.15±28.74
J0902+0443	42.20	5007.75±0.27	54.31±16.17	286.25±26.35	4999.03±0.66	-521.95±54.49	1231.01±20.36
J0937+3615	41.76	5006.98±0.14	8.20±8.38	404.70±11.98	5002.80±0.69	-249.94±48.50	999.76±25.15
J0948+0022	41.27	4993.97±1.05	-770.79±62.87	1438.29±55.69	−	−	−
J0952−0136	41.67	5005.96±0.08	-52.87±4.79	558.40±4.19	4994.51±0.52	-685.82±33.53	1583.53±13.77
J0953+2836	42.07	5006.25±0.23	-35.51±13.77	344.06±16.17	4995.81±1.38	-624.77±94.60	592.24±56.88
J1031+4234	41.83	5009.07±0.30	133.35±17.96	231.26±10.78	5005.45±0.92	-216.94±65.86	744.53±10.18
J1034+3938	41.03	5006.76±0.04	-4.97±2.40	228.44±1.80	5002.54±0.17	-253.01±10.78	901.05±4.79
J1037+0036*	41.60	5008.56±0.42	102.81±25.15	280.61±7.78	4999.72±0.58	-529.11±58.08	356.75±22.15
J1038+4227	41.62	5005.11±0.12	-103.77±7.19	314.45±7.78	4999.87±0.52	-313.96±36.52	1146.41±28.14
J1047+4725	42.89	5006.66±0.07	-10.96±4.19	280.61±4.79	5004.82±0.39	-110.43±25.75	844.65±24.55
J1048+2222	41.79	5003.35±0.31	-209.15±18.56	389.19±19.76	4994.49±0.75	-530.88±61.07	1238.06±16.77
J1102+2239	42.38	4997.40±0.36	-565.41±21.56	879.90±11.38	4984.90±2.41	-749.79±164.06	1319.85±83.23
J1110+3653	41.73	5007.53±0.22	41.14±13.17	400.47±16.77	−	−	−
J1133+0432	41.42	5008.83±0.04	118.97±2.40	235.49±8.38	−	−	−
J1138+3653	41.68	5005.39±0.17	-87.00±10.18	234.08±16.17	5004.59±0.43	-48.40±34.73	923.61±28.74
J1146+3236	42.00	5007.10±0.10	15.39±5.99	307.40±4.19	5001.47±0.40	-336.86±28.74	620.44±7.78
J1200−0046	41.87	5007.01±0.10	10.00±5.99	289.07±17.36	5008.26±0.22	74.89±17.36	757.22±26.35

J1227+3214	42.11	5007.84±0.05	59.70±2.99	242.54±1.80	5004.35±0.12	-209.05±8.38	592.24±3.59
J1238+3942	41.98	5005.75±0.15	-65.45±8.98	380.73±15.57	–	–	–
J1246+0238*	41.64	5007.51±0.35	39.94±20.96	382.14±20.36	4999.10±1.96	-503.49±136.52	1245.11±70.06
J1302+1624	42.31	5003.65±0.05	-191.19±2.99	408.93±1.20	–	–	–
J1305+5116	43.14	5003.62±1.36	-192.98±81.43	1012.45±77.84	4993.35±2.45	-615.00±226.33	1394.58±43.11
J1333+4141	42.34	5005.35±0.08	-89.40±4.79	521.73±3.59	5001.35±0.11	-239.37±10.18	1745.69±5.39
J1337+6005	41.75	5005.22±0.11	-97.18±6.59	355.34±6.59	4997.93±0.42	-436.74±29.94	1128.07±14.97
J1346+3121	41.39	5005.55±0.51	-77.42±30.54	248.18±55.09	5001.72±2.60	-229.05±184.42	920.79±102.39
J1358+2658	42.36	5007.86±0.05	60.89±2.99	448.41±3.59	5003.64±0.24	-252.57±16.17	1366.38±5.39
J1409+5656	41.26	5005.27±0.35	-94.19±20.96	569.68±21.56	–	–	–
J1432+3014	42.60	5007.06±0.04	12.99±2.40	346.88±1.80	5002.79±0.19	-255.70±11.98	1145.00±7.19
J1435+3131	42.16	5005.74±0.17	-66.04±10.18	294.71±15.57	5003.26±1.01	-148.30±69.46	1049.11±97.60
J1443+4725	42.32	4999.40±0.54	-445.66±32.33	1199.99±33.53	–	–	–
J1450+5919	41.55	5006.30±0.06	-32.51±3.59	265.10±3.59	5002.13±0.27	-249.65±18.56	971.55±9.58
J1505+0326	41.77	5000.96±0.99	-352.25±59.28	597.88±60.48	4995.52±4.34	-326.51±317.35	1180.25±131.13
J1507+4453	42.50	5007.29±0.04	26.76±2.40	298.94±1.80	5003.18±0.10	-245.96±6.59	1187.30±4.79
J1548+3511	42.40	5006.63±0.07	-12.75±4.19	265.10±2.40	4999.95±0.59	-400.03±37.72	971.55±27.54
J1608+0708	41.17	5006.31±0.14	-31.91±8.38	279.20±9.58	5000.14±0.60	-369.45±42.51	1016.68±21.56
J1612+4219	42.31	5004.23±0.14	-156.46±8.38	741.71±12.57	5005.96±0.36	103.66±28.14	1913.50±20.96
J1629+4007	42.06	5009.08±0.06	133.94±3.59	211.51±2.40	5004.52±0.34	-272.60±22.15	830.54±19.16
J1633+4718	41.65	5006.57±0.05	-16.35±2.99	255.23±1.80	5001.91±0.23	-278.77±14.97	1185.89±13.17
J1634+4809	41.96	5002.47±0.44	-261.84±26.35	389.19±24.55	4993.44±1.69	-541.39±125.14	1109.74±56.28
J1644+2619*	40.91	5006.68±0.44	-9.76±26.35	145.24±9.58	–	–	–
J1703+4540	41.55	5010.34±1.23	209.39±73.65	335.60±49.10	5004.73±3.96	-335.68±309.56	645.82±110.77
J1709+2348	42.14	5008.43±0.09	95.02±5.39	401.88±3.59	5003.06±0.39	-321.53±26.94	786.83±9.58
J1713+3523	40.98	4995.59±0.88	-673.79±52.69	1641.35±47.90	–	–	–
J1722+5654	42.19	5006.64±0.12	-12.15±7.19	321.50±5.99	4999.30±0.45	-439.04±32.33	716.33±21.56
J2314+2243*	42.31	5006.86±0.81	1.02±48.50	602.11±25.75	4989.64±2.20	-1031.42±178.43	1579.30±55.69

Chapter 5

Radio luminosity functions

5.1 Introduction

In this chapter I will consider another possibility for the parent population. RQNLS1s belong to the parent population if radio-lobes are lacking, otherwise they would be visible for present day observatories, and these sources would not be classified as radio-quiet. But lobes might instead be only developed on small scale. In this case, the source could appear as a compact steep-spectrum object (CSS). The investigation of this new class of candidates will be carried out again by means of black hole mass and Eddington ratio, but also with the radio luminosity function. The latter is in principle able to solve the parent population problem for each candidate sample, but it is not trivial to use, since it requires a few non-trivial calculations and, above all, statistically complete samples.

To fulfill this completeness condition, I tried to find in the literature some suitable samples for S-NLS1s, disk RGs and RQNLS1s. The currently known S-NLS1s are too few. In fact although several RLNLS1s can be extracted from SDSS, the vast majority of them have no measured spectral index yet. Disk RGs are also very rare. I tried to select sources with a spiral host galaxy from the Schawinski et al. (2010) sample of AGN with a morphological classification provided by the GalaxyZoo project (Lintott et al. 2008). Nevertheless, among 132 spiral galaxies, I found only one source with a nuclear radio-loudness larger than 10, which of course is not enought to derive a luminosity function. For RQNLS1s finally I managed to create a complete sample up to z = 0.35. Such sample is different from that selected by Cracco et al. (submitted) and described in 4.2.1, because it has no constrains on the S/N ratio. Anyway the redshift limit is likely too low to allow a direct comparison with F-NLS1s, so this RQNLS1s sample will be used in Chapter 6 for a different purpose.

In the present chapter instead I decided to focus only on CSS which, as mentioned in Section 1.2.5, might be interesting parent candidates. As previously explained, RQNLS1s can belong to the parent population if radio-lobes are lacking, but lobes might instead be only developed on small scale. In this case a RLNLS1 could appear as a compact steep spectrum object (CSS). CSS represent an important fraction of radio sources, showing a radio spectrum peaked at ~100 MHz and radio-jets entirely within the host galaxy (see the review by O'Dea 1998). Often they are thought to be closely connected with Gigahertz peaked-spectrum sources (GPS), and a widely diffuse theory to explain their nature is the youth scenario (Fanti et al. 1995). Their age was determined in several ways, and found to be less than 10^5 years (Owsianik & Conway 1998; Murgia et al. 1999). Their jets already developed

radio-lobes, and are typically still crossing the interstellar medium and interacting with it (e.g. Morganti et al. 2015, and references therein). As radio-galaxies, they can be classified as high-excitation or low-excitation radio-galaxies (HERG or LERG, respectively), according for example to the ratio [O III]/Hα (Laing et al. 1994). The main difference between these classes is likely the accretion mechanism onto the black hole, with HERGs showing typically a more efficient accretion process (Hardcastle et al. 2007).

I already mentioned that a link between NLS1s and CSS was suggested by many authors (Oshlack et al. 2001; Komossa et al. 2006; Gallo et al. 2006; Yuan et al. 2008; Caccianiga et al. 2014; Gu et al. 2015; Schulz et al. 2015). All the characteristics of NLS1s indeed closely recall those of CSS: they are often considered young sources and at the same time their jet, when present, appears to interact with the medium (Marziani et al. 2003; Komossa et al. 2006 and the previous chapter). RLNLS1s can be classified as HERG, having an efficient accretion mechanism and strong high-ionization lines. Therefore CSS/HERGs might be part of their parent population, under the assumption that radio-lobes are already developed, and I tried to understand whether this hypothesis is correct. This chapter was submitted as a paper to Astronomy & Astrophysics.

5.2   Samples

5.2.1   NLS1s

As stated before, complete samples are required to build the luminosity functions. The NLS1s sample must also have measured spectral indices, to select only flat-spectrum sources without including any S-NLS1. The largest sample in the literature that meets my requirements is that of Yuan et al. (2008), already used in Chapter 3. It includes 23 very radio-loud NLS1s, and 19 out of 23 spectral indices are known. Their sample was selected from SDSS DR5, looking only for those sources whose radio-loudness - calculated using the 1.4 GHz flux density - is above 100 at $z < 0.8$. The sample includes 13 flat-spectrum sources and 4 with unknown spectral index.

The Yuan sample should be statistically complete, being drawn from the already complete sample of Zhou et al. (2006). Anyway I independently tested its completeness. I first noticed that Foschini et al. (2015), whose sample was selected with an accurate search in the literature, found all the very radio-loud objects in DR5 already included in the Yuan sample. The cumulative distribution of sources as a function of redshift anyway shows a flattening close to the upper z limit. This flattening in the distribution is likely caused by the lack of classification. The S/N of the optical spectra worsen with increasing distance, and even if very radio-loud sources typically have bright optical lines (such as [O III], e.g. de Bruyn & Wilson 1978), a correct classification is quite difficult.

I tried to avoid this problem considering that the quasars distribution in SDSS appears to be complete up at 94.6% up to magnitude i<19.1 (Richards et al. 2002). In the Yuan sample, all the flat-spectrum sources but one match this magnitude criterium when $z < 0.6$. I therefore decided to use this threshold as upper redshift limit for my sample. This allows to have a good degree of completeness in my sample. Using these criteria, 12 F-NLS1s remain. I will also consider 2 more sources with undetermined spectral index which meet the redshift criterion, to test the stability of my results.

Table 5.1 HERGs parameters. Columns: (1) Object SDSS name; (2) logarithm of the black hole mass in $M_\odot$; (3) logarithm of the bolometric luminosity in erg s^{-1}; (4) logarithm of the Eddington ratio.

SDSS Name	$\log M_{BH}$	$\log L_{bol}$	logEdd
SDSS J002833.42+005510.9	8.94	44.1	-2.96
SDSS J075756.71+395936.0	7.13	43.77	-1.52
SDSS J084856.57+013647.8	7.05	44.41	-0.74
SDSS J092607.99+074526.6	7.28	44.93	-0.47
SDSS J094525.90+352103.5	7.23	44.48	-0.85
SDSS J114311.01+053516.1	8.84	45.08	-2.0
SDSS J115727.61+431806.3	7.68	44.67	-1.1
SDSS J140416.35+411748.7	7.96	43.88	-2.22
SDSS J140942.44+360415.8	8.24	43.82	-2.52
SDSS J164311.34+315618.4	7.44	45.39	-0.17

5.2.2 HERG

My aim was to find CSS sources classified as HERGs, so I searched again in the literature for a suitable sample. I decided to use that of Kunert-Bajraszewska et al. (2010), who selected a sample of 44 low-luminosity compact objects, with a radio luminosity at 1.4 GHz lower than 10^{26} W Hz^{-1} (in a cosmology with H$_0$ = 100 km s^{-1} Mpc^{-1} and q$_0$ = 0.5). In addition to this criterion, these sources have a flux density 70 mJy $\leq S_{1.4\,GHz} \leq$ 1 Jy, and a radio spectral index $\alpha_\nu > 0.7$ between 1.4 and 4.85 GHz. Their radio-selected sample was later cross-matched with the SDSS DR7 spectroscopic archive, finding 29 sources at z < 0.9 (Kunert-Bajraszewska & Labiano 2010). Ten of them were classified as LERG, 12 as HERG, and 7 remained unclassified because of a S/N $\lesssim$ 3. I tested the completeness of this sample as before. As in the F-NLS1s sample, the cumulative distribution finds a drop in the source counts above z $\sim$ 0.6. Below this threshold, only one source is above the SDSS completeness limit of 19.1 mag. Therefore I decided to use again the same limits, considering then only 10 sources. Since both samples have the same redshift limit, and they both have a lower limit in flux including only bright radio-sources, the comparison between them should be relatively unbiased.

5.2.3   Control sample

As a control sample for the luminosity function I decided to use the sample of 50 FSRQs used by Padovani & Urry (1992), which in turn are drawn from the work of Wall & Peacock (1985). The sources have a flux density above 2 Jy at 2.7 GHz, and Galactic latitude $|b| >$ 10°. They also have a spectral index $\alpha_\nu \leq 0.5$ between 2.7 and 5 GHz, and they were not classified as BL Lacs by Stickel et al. (1991). Padovani & Urry (1992) added one more source to the Wall & Peacock (1985) sample, because of its high optical polarization.

5.3   Black hole mass

An important step to understand the relation between CSS/HERGs and F-NLS1s is to compare their black hole masses and Eddington ratio. I already calculated both these values for all my F-NLS1s (Foschini et al. 2015), so I used those estimates also in the present work. For CSS/HERGs I obtained the optical spectra from SDSS DR12. All of them were of type 2
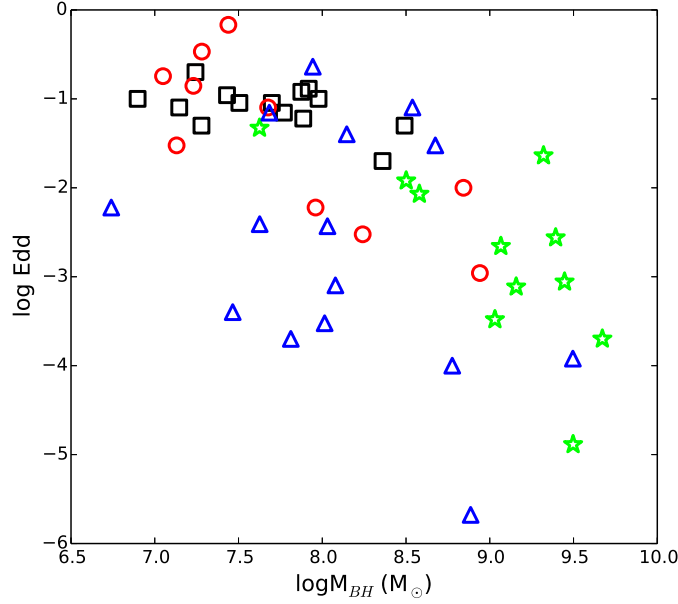
Figure 5.1 Logarithm of the BH mass vs. logarithm of the Eddington ratio. Black squares are F-NLS1s, red circles are CSS/HERGs, blue triangles are disk-hosted radio-galaxies and green stars are elliptical-hosted radio-galaxies. The points of these last two samples are derived from Chapter 3.

or intermediate type AGN, therefore I could not use permitted lines to derive the black hole mass because the BLR is obscured. I then followed the procedure described in Chapter 3 for type 2 and intermediate sources, deriving the stellar velocity dispersion σ_* from the width of the [O III] lines core component. Once removed the blue wing, the core component of [O III] should indeed be less affected by the jets/ISM interaction, and typically dominated by the gravitational potential of the bulge stars (Greene & Ho 2005a). This method provided good approximations for black hole mass both in elliptical- and disk-hosted radio-galaxies. To obtain the bolometric luminosity, I used Eq. 3.9.

The results are shown in Tab. 5.1. The logarithmic mean mass value for HERGs is 7.78 with a standard deviation of 0.66, while for F-NLS1s is 7.68 with a standard deviation of 0.44. The median values are 7.84 and 7.73, respectively. It is evident that the two distributions are very similar. I compared them by means of the K-S, finding that the null hypothesis of the two samples being drawn from the same population cannot be rejected, with a p-value of 0.95. To directly compare this result with those found for other parent candidates in Chapter 3, I also evaluated the product of Eq. 3.10. Such value is useful to test the distance between the samples. In this case the value is equal to 0.52, and the CSS/HERGs sample appears then to be the closest to F-NLS1s, even closer than S-NLS1s (see Tab. 3.8).

The Eddington ratio distributions are also quite close (K-S p-value 0.17). The median Eddington ratio is 0.06 for CSS/HERGs and 0.09 for F-NLS1s. These values are comparable to those of other NLS1s classes, but it is worth noting that the CSS/HERGs sample shows some outliers with lower accretion luminosities. All these values are shown in Fig. 5.1, along with disk-hosted and elliptical-hosted radio-galaxies from Chapter 3.

The good overlap in mass between F-NLS1s and CSS/HERGs is visible, and I also point

Table 5.2 Results of the V/V_{max} test. The results for F-NLS1s are showed in two different ways: with or without 2 sources with unknown spectral index. The former are indicated with an asterisk. Columns: (1) sample; (2) number of sources; (3) result of the test; (4) associated error to the test; (5) distance from uniform distribution in σ units; (6) K-S test p-value against uniform distribution.

Sample	N	V/V_{max}	σ	d	K-S
F-NLS1	12	0.52	0.08	0.25	0.95
F-NLS1*	14	0.58	0.08	1.00	0.26
HERG	10	0.54	0.09	0.44	0.72
FSRQ	50	0.70	0.04	5.00	2×10^{-9}

out that disk RGs have a similar mass distribution to CSS/HERGs (K-S p-value 0.15). On the contrary, the black hole mass of elliptical radio-galaxies is much larger. The K-S confirms this difference providing a p-value of 3×10^{-3}, which allows me to reject the null hypothesis.

5.4   V/V$_{max}$ test

Another step to understand the relation between these sources is to check whether evolution is present in my samples or not. An useful tool to test evolution is the so-called V/V$_{max}$ test (Schmidt 1968). By definition, V$_{max}$ is the volume within which a source of luminosity L can be detected, while V is the spherical volume associated with each source. The luminosity of a source of detected flux F is $L = 4\pi d^2 F$, where d is the luminosity distance. If the flux detection limit is F$_{min}$, the source can be detected up to

$$d_{max} = \sqrt{\frac{L}{4\pi F_{min}}} \qquad (5.1)$$

which corresponds to a redshift z_{max}. For a non-evolving population, the ratio between the spherical volume V corresponding to the object redshift and V$_{max}$ is expected to be uniformly distributed between 0 and 1, with an average value $\langle V/V_{max} \rangle = 0.5$. When $\langle V/V_{max} \rangle > 0.5$, the population is positively evolving, with more (or more luminous) sources located at larger distances. If conversely $\langle V/V_{max} \rangle < 0.5$, the sample is negatively evolving.

To evaluate V$_{max}$ for each object, I used as d_{max} the smaller value between those derived from the radio detection limit (1 mJy for F-NLS1s, 70 mJy for CSS/HERGs, 2 Jy for FRSQs), the spectroscopic limit for quasars in SDSS DR7 (19.1 mag), and the redshift upper limit of each sample, z = 0.6. The CSS/HERGs sample has also an upper flux limit, which translates into a lower redshift limit z$_{min}$. Therefore in this case I used the modified version of the test over the accessible volume V$_a$ (Avni & Bahcall 1980), defined as

$$\frac{V}{V_a} = \frac{V - V_{min}}{V_{max} - V_{min}} \ , \qquad (5.2)$$

where V$_{min}$ is the inaccessible inner part of the comoving volume due to z$_{min}$, and V is the comoving volume of each source. The associated error in the V/V$_{max}$ test is $\sigma = 1/\sqrt{12N}$, where N is the number of sources in each sample. To calculate both the luminosity distance from redshift and the comoving volume, I used the `Cosmolopy` tool developed for `Python`[1].

---

[1]http://roban.github.com/CosmoloPy/

The results are summarized in Tab. 5.2. The control sample of FSRQs is showing a strong positive evolution at 5σ. This result is in agreement with that found by Padovani & Urry (1992) and many other authors. FSRQs indeed are known for having a strong evolution with time. Conversely, the V/V_{max} result is consistent with the uniform distribution at 1σ for both F-NLS1s and CSS/HERGs. In particular the result for F-NLS1s does not change whether the two sources with undetermined spectral index are included or not. This is an indication that, at least up to $z = 0.6$, these sources do not have any strong evolution.

I performed a K-S test between the observed V/V_{max} distributions in my sample and the theoretical uniform distribution. The null hypothesis is that the observed distribution is drawn from a uniform distribution. As reported in Tab. 5.2, the test confirms all the previous results, showing that the only sample where the null hypothesis is rejected is the FSRQs sample. Therefore, while the luminosity function of FSRQs will be corrected for evolution and reported to z = 0, those of F-NLS1s and CSS/HERGs will not.

5.5   Luminosity functions

5.5.1   Method

The luminosity function (LF) describes the volumetric density of sources as a function of their luminosity. For flux-limited samples, the LF is computed as in Peterson (1997)

$$\Phi(L) = \frac{1}{\Delta L} \frac{4\pi}{A} \sum_{L_i \in (L \pm \Delta L/2)} \frac{1}{V_{max}(L)} \, , \qquad (5.3)$$

where ΔL is the width of the luminosity bin, and A is the area of sky covered by the samples. In my cases, the area covered both by the DR5 and FIRST is $\sim 1/7$ of the whole sky, while the common area between DR7 and FIRST is $\sim 1/6$.

To compute the LF I divided the sources in bins of luminosity (L$-\Delta$L/2, L$+\Delta$L/2). In those samples which have a lower redshift limit, instead of V_{max} I used the accessible volume V_a. I assume that the only source of uncertainty in the LF is the error on the number counts per bin, hence I assumed a Poissonian statistics. It is worth noting that the Poissonian statistics is not symmetric for small values (N $\lesssim$ 10): to evaluate the errors in the low statistic limit I used the values from Gehrels (1986).

My aim was to determine the radio LF for each sample. I then calculated the luminosity at 1.4 GHz for each source from the peak flux of the FIRST survey. I performed a K-correction, using all the spectral indices I found in the literature. For those two sources with no known spectral index, I assumed a flat spectrum ($\alpha_\nu = 0$). I divided the luminosities in bins of 0.25 dex for the control sample, since there were enough data to fill each bin. In the other two cases, I used a binning of 0.5 dex. The LFs were fitted with a single power-law

$$\Phi(L) = KL^\alpha \, , \qquad (5.4)$$

where K is a constant and α the slope of the power-law. In the case of FSRQs, in analogy with what done by Padovani & Urry (1992), I used a broken power-law in the form

$$\Phi(L) = \frac{\Phi_b}{(L/L_b)^\alpha + (L/L_b)^\beta} \, , \qquad (5.5)$$
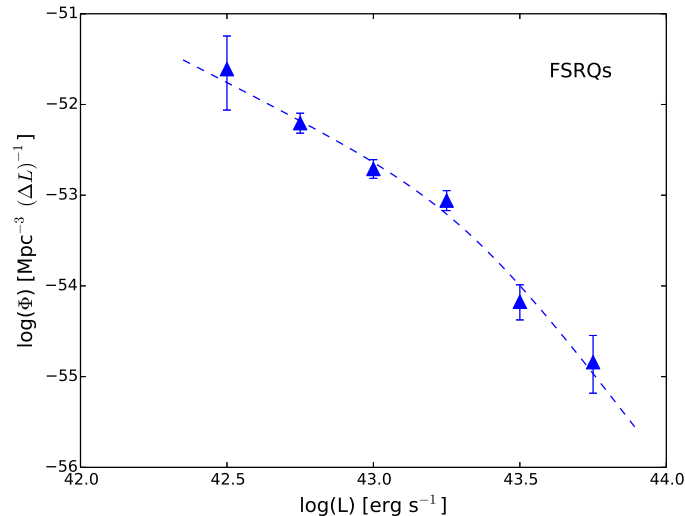
Figure 5.2 Monochromatic radio luminosity function of FSRQs control sample at 1.4 GHz. The dashed line is the best-fit with a broken power-law.

where Φ_b is the normalization factor, L_b is the break luminosity, and α and β are the two slopes. In the FSRQs sample I also applied a correction for luminosity evolution to bring each source to z = 0. For this purpose, I assumed the same cosmological evolution found by Padovani & Urry (1992), $\exp\left(-T/\tau\right)$, where T is the lookback time and $\tau = 0.23$ is the time-scale of evolution in units of Hubble time. Using the spectral indices I also derived the 1.4 GHz flux for each FSRQ, to allow a direct comparison with the other samples. All fits were performed using the generalized least squares method. The results are shown in Fig. 5.2 and 5.3, and summarized in Tab. 5.3.

My FSRQs LF is in agreement with that obtained by Padovani & Urry (1992) when the cosmology they adopted is used. In F-NLS1s, I note that the inclusion in the LF of the two sources with undetermined spectral index has a negligible impact, since neither the slope nor the coefficient of the LF are significantly affected (Tab. 5.3). In both cases, the scatter is quite high, likely because of the low statistic. The slope of HERGs is steeper than that of F-NLS1s, which indeed have a quite flat LF. In particular, the slope of F-NLS1s is close to that of FSRQs for luminosities below the break, even if the error on this slope is quite large. This result becomes more evident when the LFs of F-NLS1s and FSRQs are shown together, as in Fig. 5.4. The two LFs are quite close in the region of 10^{43} erg s^{-1}, and the LF of F-NLS1s appears to be an extension of that of FSRQs at lower luminosities.

5.5.2 Relativistic beaming

In order to compare the beamed sources with their parent population, I have to take into account the effect of beaming on the LF shape. I then added the relativistic beaming to the CSS/HERGs luminosity function. This cannot be done analitically, as explained by Urry & Shafer (1984) and Urry & Padovani (1991). I followed the procedure described by Urry & Shafer (1984) for a single power-law. In analogy with that work, I defined as $\mathcal{L}$ the intrinsic luminosity, and with L the observed luminosity. These two quantities are related via $L = \delta^p \mathcal{L}$,
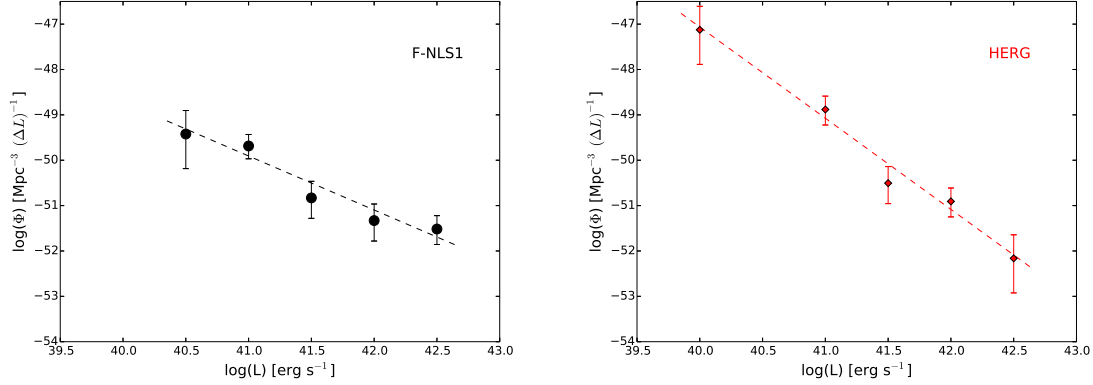
Figure 5.3 Monochromatic radio luminosity functions at 1.4 GHz. Top panel: F-NLS1s; bottom panel: HERGs. Dashed lines are the single power-law best-fit.

Table 5.3 Parameters of the luminosity functions. The LF of F-NLS1s is showed in two different ways: with or without 2 sources with unknown spectral index. The former is indicated with an asterisk. Columns: (1) Sample; (2) Function used for the best-fit. PL for power-law, BPL for broken power-law; (3) logarithm of minimum luminosity bin (erg s^{-1}); (4) logarithm of maximum luminosity bin (erg s^{-1}); (5) logarithm of luminosity break (erg s^{-1}); (6) logarithm of the luminosity function at the break (Mpc^{-3}); (7) coefficient of the power-law; (8) slope of the power-law (slope below the break for broken power-law); (9) slope above the break (for broken power-law only).

Sample	Mod.	log L$_1$	log L$_2$	log L$_b$	log Φ_b	log K	α	β
F-NLS1	PL	40.5	42.5	–	–	-2.15$\pm$5.96	-1.17$\pm$0.14	–
F-NLS1*	PL	40.5	42.5	–	–	-3.53$\pm$5.88	-1.13$\pm$0.14	–
HERG	PL	40.	42.5	–	–	33.32$\pm$5.96	-2.01$\pm$0.14	–
FSRQ	BPL	42.5	43.75	43.32$\pm$0.47	-53.10$\pm$1.34	–	1.61$\pm$0.98	4.33$\pm$2.00

where $\delta = [\Gamma(1 - \beta \cos \theta)]^{-1}$ is the kinematic Doppler factor of the jet and the exponent is $p = 3 + \alpha_\nu$, where α_ν is the intrinsic slope of the jet emission. The total flux emitted by the source is given by L $= (1 + f\delta^p)\mathcal{L}_u$, where $\mathcal{L}_u$ is the unbeamed luminosity and f the ratio between the jet luminosity and the unbeamed luminosity. The model is then evaluated numerically via

$$\Phi(L) = \int \frac{K}{\beta \gamma p} f^{1/p} \mathcal{L}^{\alpha-1} \left(\frac{L}{\mathcal{L}} - 1 \right)^{-(p+1)/p} d\mathcal{L} \ . \tag{5.6}$$

I used $p = 3.7$, because the typical slope of a syncrotron spectrum is $\alpha_\nu = 0.7$. I also performed my calculations for different values of f ($0.01 \leq f \leq 1$), and of bulk Lorentz factor, $8 \leq \Gamma \leq 15$, which are values already observed in γ-ray emitting NLS1s (Abdo et al. 2009b; D'Ammando et al. 2012). To evaluate the Doppler factor I assumed the angle to vary between $0° \leq \theta \leq \theta_c$, where θ_c is the critical angle for which $\delta(\Gamma, f, \theta_c) = 1$. Therefore all the sources with inclination θ appear as F-NLS1s. In the case of a simple power-law, the resulting beamed LF is a broken power-law.

From the error bars I derived the maximum and minimum values allowable for the data. The errors in the models of beamed LF are evaluated by refitting such maximum and minimum values. These new fits were performed using the same functions adopted for the previous
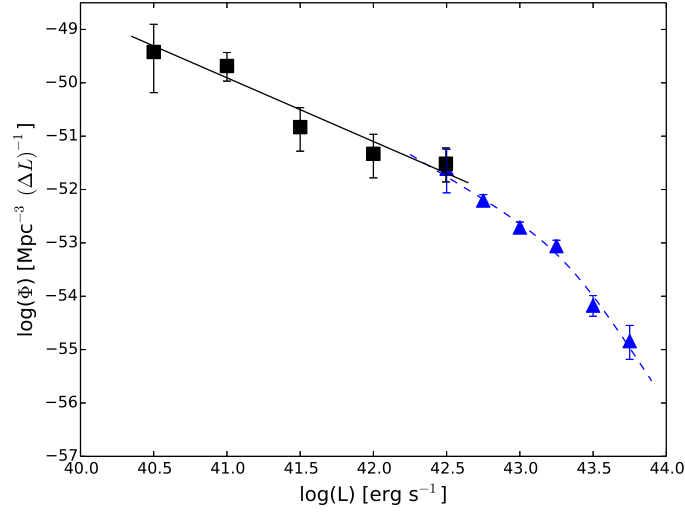
Figure 5.4 Monochromatic radio luminosity functions of F-NLS1s and FSRQs at 1.4 GHz. The black squares are the F-NLS1s data points, the blue triangles the FSRQs data points. The blue dashed line is the broken power-law best-fit for FSRQs, the black solid line is the single power-law best-fit for F-NLS1s.
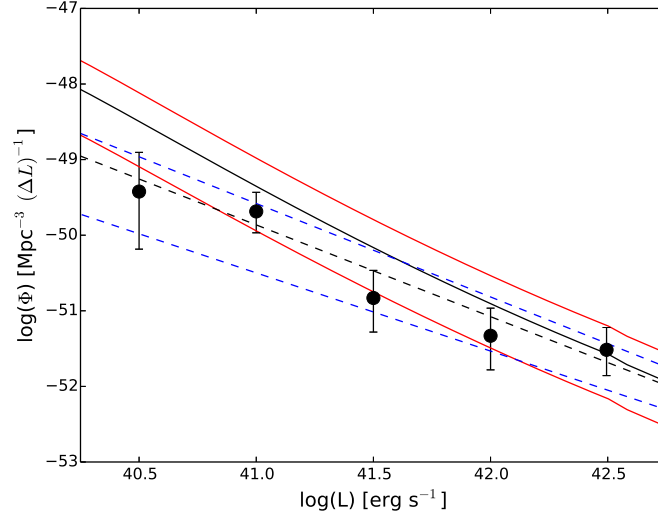
Figure 5.5 HERGs LF with relativistic beaming added, for bulk Lorentz factor $\Gamma = 10$ and ratio $f = 1$. Black solid line is the model, red solid lines are the maximum and minimum values for the model. Black circles are F-NLS1s data, black dashed line is the F-NLS1s LF best-fit, and blue dashed lines are the maximum and minimum values for F-NLS1s LF.

fitting of the data. I then added the relativistic beaming both to the best-fit, the minimum and the maximum fit. The resulting parent+beaming model is shown in Fig. 5.5.

In order to test my results, I evaluated the distance between the model and my data by means of the reduced chi-squared, χ_ν^2. The results are shown in Tab. 5.4. I report the χ_ν^2 of the model and the lowest χ_ν^2 considering also the maximum and minimum curve. In all cases, the χ_ν^2 has 4 degrees of freedom. I also evaluated the model for several values of bulk Lorentz

Table 5.4 χ^2_ν for the beaming model tested with different parameters. The star indicates that the F-NLS1s sample included also the two sources with unknown spectral index. Columns: (1) sample; (2) bulk Lorentz factor of the jet; (3) ratio between beamed and diffuse emission from the jet f; (4) χ^2_ν of the model; (5) χ^2_ν of the maximum model; (6) χ^2_ν of the minimum model.

Sample	Γ	f	χ^2_ν	χ^2_ν (max)	χ^2_ν (min)
HERG	10	1.0	1.95	5.74	1.37
HERG*	10	1.0	1.62	5.71	1.66
HERG	8	1.0	2.15	6.29	1.05
HERG*	8	1.0	1.83	6.34	1.23
HERG	15	1.0	1.97	5.41	1.89
HERG*	15	1.0	1.65	5.28	2.33
HERG	10	0.5	1.92	5.52	1.61
HERG*	10	0.5	1.59	5.44	1.98
HERG	10	0.1	2.38	5.95	2.02
HERG*	10	0.1	2.06	5.84	2.43
HERG	10	0.01	9.34	16.43	3.17
HERG*	10	0.01	9.53	17.55	2.89

factor, to understand up to which values the model was still acceptable.

As shown in Fig. 5.5, the best-fit power-law for F-NLS1s and the model prediction are in good agreement, but there is a deviation at lower luminosities. In particular, the slope of the model in the region occupied by F-NLS1s is -1.55, while the slope of the measured LF is -1.17. The values of χ^2_ν are not very close to 1, largely because of this deviation. I think that the latter is due to a selection effect. My F-NLS1s sample includes only very radio-loud NLS1s, therefore the resulting luminosity function might be underestimated in the low luminosity region. Keeping this in mind, the overlapping of the model with the observed function is quite satisfactory.

In Tab. 5.4 I report the values of χ^2_ν calculated with the different values of Γ and f. I highlight that the closest χ^2_ν between the model and the data is observed in the sample which includes the two sources with undetermined spectral index, for a ratio $f = 0.5$ and $\Gamma = 10$, which translates in a slope of the model of -1.59. This value of f is significantly higher than that observed in FSRQs, which is between $10^{-3} - 10^{-2}$ (Padovani & Urry 1992).

5.6   Discussion

5.6.1   Black hole mass

The first result that must be highlighted is that the black hole mass distribution of CSS/HERGs is quite similar to that of F-NLS1s, with typical values between 10^7 and 10^8 M$_\odot$. Also the Eddington ratio is quite high, comparable to that of typical NLS1s, both radio-loud and quiet. This is quite expected if NLS1s and CSS/HERGs have both a radiatively efficient accretion mechanism, similar to that of FSRQs.

The K-S test revealed that the distributions of these quantities, both mass and Eddington ratio, in F-NLS1s and CSS/HERGs might be drawn from the same population. The most obvious interpretation of this result is that CSS/HERGs might actually be misaligned F-NLS1s. Of course this result is obtained for very small samples, so it must be taken with some caution. In particular the masses of CSS/HERGs, being derived using forbidden lines, must be considered only as an upper limit. If the narrow-line region is perturbed because of

interaction with the relativistic jet, the FWHM is indeed higher, and leads to an overestimate of the mass. Nevertheless my findings are in good agreement with those of previous works, where the similarity between CSS/HERGs and NLS1s was already pointed out. For example Wu (2009b) found that a large number of CSS/GPS has a black hole mass between $10^{7.5}$ and 10^8 M$_\odot$, and the same conclusion was obtained by Son et al. (2012) again on CSS, both HERGs and LERGs. Moreover the sample by Foschini et al. (2015), of which my is a subset, revealed that on average F-NLS1s have also black hole mass between 10^7 and 10^8 M$_\odot$. All these results then seem to support my hypothesis.

5.6.2 Evolutionary picture

The V/V$_{max}$ test shows that both F-NLS1s and CSS/HERGs have no significant luminosity and/or density evolution up to z = 0.6. FSRQs instead show a strong luminosity evolution, but the sample is extended to much larger distances. An interesting result I found is shown in Fig. 5.4, and it might point out that FSRQs and F-NLS1s are strictly connected to each other. F-NLS1s were suggested to be the low-mass tail of γ-ray emitting AGN, and in particular of FSRQs (Foschini et al. 2015, and references therein). Since the black hole mass and the jet power are connected (Heinz & Sunyaev 2003), the lower radio-luminosity and jet power of F-NLS1s might be a consequence of the lower black hole mass. Therefore it is expected to find F-NLS1s being the low-luminosity tail of FSRQs LF, as I indeed observe. Of course, there might be some low luminosity FSRQs which cannot be classified as NLS1s. The criteria for NLS1s classification is indeed based mainly on the Hβ width, which is not just a function of the black hole mass. Therefore not all low mass FSRQs can be classified as NLS1s, even if their black hole mass and radio emission are comparable.

An explanation for the low mass is the young scenario of NLS1s. If this is true, F-NLS1s might be the young counterpart of FSRQs in which the nuclear activity started only recently, and in which the black hole (and possibly the host galaxy) is still (co-)evolving. A similar picture was already suggested for CSS sources years ago (Readhead et al. 1996; Fanti et al. 1995; O'Dea & Baum 1997). These likely young radio sources are thought to be an evolutionary phase that is going to evolve into the giant double sources. In particular, Kunert-Bajraszewska & Labiano (2010) took into account also the optical division into HERG and LERG, finding that the CSS/HERGs sources are likely going to evolve into FR$_{HERG}$. Recently, Giommi et al. (2012) suggested that the two blazar classes, and hence their parent population, should be divided according to their low or high ionization, and that all the other classifications are physically irrelevant. If this is true, FSRQs can be identified as beamed HERGs, and F-NLS1s, which might be young FSRQs, should be the beamed version of young HERGs, so CSS/HERGs. In summary, the evolutionary picture for beamed sources might be simply F-NLS1 $\rightarrow$ FSRQ, and for their parent population CSS/HERGs $\rightarrow$ FR$_{HERG}$. An evolutionary connection between F-NLS1s and FSRQs is then possible, where the formers are still growing to become the latters. This hypothesis finds further support in my Fig. 5.5. When the relativistic beaming is added using the typical bulk Lorentz factor of γ-ray emitting NLS1s, CSS/HERGs LF reproduces quite well the data. Even if at low luminosities the model predicts a larger number of F-NLS1s that I do not observe, I think that this discrepancy might only be due to the selection criterion of my NLS1s sample. Keeping this caveat in mind, the model seems then to indicate that CSS/HERGs might be good parent candidates.

In young radio-sources as CSS, the jet activity might be intermittent, and several outburst episodes might be induced by pressure radiation instabilities in the accretion disk, with a

timescale of 10^2-10^5 years (Czerny et al. 2009; Wu 2009a). A similar, strong variability is observed also in RLNLS1s (Foschini et al. 2012, 2015), providing further confirmation for this unified model. If CSS/HERGs are parent sources, the origin for these activity/inactivity phases in F-NLS1s might be the same. The radiation pressure instability is indeed one of the hypotheses that can account for the non-thermal emission and extended structures observed in some radio-quiet NLS1s (Doi et al. 2012), where the jet activity phase might have lasted for only a few years leaving then the observed structures (Ghisellini et al. 2004).

The inclusion of CSS/HERGs in the parent population of F-NLS1s might moreover definitively rule out the vast majority of RQNLS1s as parent candidates. In fact, since CSS/HERGs display lobes already developed (Orienti 2015), this means that the extended radio emission form even in very young ages, which in turn implies the rejection of the radio-quiet hypothesis. This conclusion is in agreement with the results of Chapter 4, where the observed differences in narrow-line region properties points in the same direction.

Another aspect to consider is the role that S-NLS1s can play in this scenario. As shown in Chapter 3, these sources are likely misaligned F-NLS1s, therefore for this picture to be coherent they should also be part of the larger class of CSS/HERGs. The sample I used in this work unfortunately does not include any type 1 AGN, so my data can reveal nothing on this issue. Anyway this topic has already been investigated in the literature, particularly in recent years. Several authors indeed found that at least some S-NLS1s can indeed be classified as CSS/HERGs (Caccianiga et al. 2014; Komossa et al. 2015; Schulz et al. 2015). In particular the extended survey by Gu et al. (2015) showed that the radio morphology of almost each one of their S-NLS1s closely recalls that of CSS. These results are therefore in agreement with my hypothesis, and seem to favor the scenario in which CSS/HERGs are the largest class of F-NLS1s parent sources. It is also reasonable that S-NLS1s are objects observed at intermediate angles between F-NLS1s and obscured (type 2) CSS/HERGs.

It is anyway not clear whether all type 1 CSS/HERGs are NLS1s. Few CSS/HERGs have indeed lines with a $\mathrm{FWHM(H\beta)} > 2000$ km s^{-1}, and cannot be classified as NLS1s. It is then possible that the unification between CSS/HERGs and NLS1s is only in a statistical sense, that is CSS/HERGs and NLS1s are on average the same population, but with few exceptions likely connected to the NLS1s definition. If a more physical classification was used, such as black hole mass or Eddington ratio, the unification between these sources would show less outliers.

Anyway, it is also possible that the BLR geometry has some impact on these outliers. If a flattened component in the BLR is present, sources with a large inclination should appear as broad-line AGN, not classifiable as NLS1s. The presence of some relatively high mass type 1 sources in a CSS/HERGs sample might then provide a clue to the BLR geometry. Anyway it is worth noting that in the sample of CSS by Son et al. (2012), the type 1 AGN have a BH mass always below 5×10^8 M$_\odot$, and an average value of 8.9×10^7 M$_\odot$. If these sources had a flattened BLR and were randomly oriented, some of them would show a much larger mass. Instead all the values are in good agreement with those of F-NLS1s, so they do not seem to have a flattened component in the BLR. In any case, a deeper study on a larger sample is necessary to better address this problem.

5.6.3   Host galaxy

A possible objection to the identification of CSS/HERGs as the parent population of F-NLS1s is that their host galaxy might be different. In particular CSS, as many radio-loud AGN, are

usually thought to be hosted by elliptical galaxies (Best et al. 2005; Orienti 2015) and triggered by merging activity (Holt 2009). NLS1s instead are generally believed to be hosted by spiral galaxies (Crenshaw et al. 2003) with a pseudobulge formed via secular evolution (Orban de Xivry et al. 2011; Mathur et al. 2012). Nevertheless, the K-S test I performed, along with other studies, seems to draw a more complicated picture.

CSS/HERGs have a black hole mass distribution closer to that of disk RGs than to that of elliptical RGs, showing typically lower black hole mass. This might be due to the young age of these sources, so perhaps the black hole is still growing to reach the mass value of typical elliptical. Anyway the black hole mass is directly connected with the bulge dynamics, particularly with its stellar velocity dispersion (Ferrarese & Merritt 2000). So in principle a relatively low mass black hole should be rather hosted in the small bulge of a disk galaxy, instead than in a more massive elliptical. Therefore it is possible that CSS/HERGs are also hosted in disk galaxies, as NLS1s. An example of disk-host for a powerful CSS was found by Morganti et al. (2011). Moreover in a very large sample of AGN Best & Heckman (2012) found that HERGs host-galaxies have different properties than those of LERGs, and in particular that they are bluer, with lower mass, lower 4000 Å break and a stronger star formation. Such characteristics are reminiscent of those of a disk or star-forming galaxy.

Finally, I must underline that not much is known even about the host galaxy of F-NLS1s, mainly because of their high redshift. Few studies were performed on the closest F-NLS1, 1H 0323+342, and seem to suggest the presence of a disk and possibly of a pseudobulge (Antón et al. 2008; Hamilton & Foschini 2012; León Tavares et al. 2014), but of course further studies are necessary to characterize them as a population.

5.7 Summary

In this chapter I investigated the relation that exists between CSS sources with an HERG optical spectrum and F-NLS1s. My aim was to understand whether the CSS/HERGs class can be part of the parent population of F-NLS1s. To do this, I analyzed the only two statistically complete samples of CSS/HERG and F-NLS1 available so far. First I calculated the black hole mass and Eddington ratio by means of the optical spectrum, and then I studied their radio luminosity functions along with that of a control sample of FSRQs.

The black hole masses are tipically between $10^{7.5}$ and 10^8 M$_\odot$ in both samples, and the Eddington ratio is around ∼0.1. I performed a K-S test on the samples to compare their black hole mass distributions. My results, in agreement with previous studies in the literature, seem to confirm that the two distributions might be drawn from the same population, and hence that CSS/HERGs are good candidates as parent sources.

The luminosity functions seem to support the same scenario. A first result is that F-NLS1s might be the low-luminosity (and low-mass) tail of FSRQs, confirming the results of Abdo et al. (2009a) and Foschini et al. (2015). The addition of relativistic beaming to CSS/HERGs luminosity function revealed that the latter might actually be F-NLS1s with the jet viewed at large angle, and thus belonging to the parent population. In this framework, RLNLS1s with a steep radio-spectrum are sources observed at intermediate angle between F-NLS1s and CSS/HERGs with a type 2 (absorbed) optical spectrum.

My results seem also to be consistent with an evolutionary picture in which F-NLS1s and CSS/HERGs are the young and still growing phase of FSRQs and FR$_{HERG}$, respectively. A more detailed study is required on larger samples of sources. In particular, new spectral

indices are necessary to effectively compare CSS/HERGs and F-NLS1s. New large surveys at different frequencies, such as VLASS, might be helpful to improve my knowledge on these sources. Also SKA, with its unprecedented sensitivity, will likely provide an incredible amount of information to largely deepen the understanding of RLNLS1s (Chapter 6).

Chapter 6

Future developments

I often mentioned in the previous chapters that one of the biggest obstacles in the study of radio-emitting NLS1s is the small number we are sistematically dealing with. NLS1s are not generally so common: it is significant that Zhou et al. (2006) found only ∼2000 NLS1s below z = 0.8. Radio-loud NLS1s appears to be even less common: 3.5% up to z = 0.35 (Cracco et al. in prep.) and 7% up to z = 0.8 (Komossa et al. 2006). The aim of this chapter is to investigate how next generation instrument, an in particular the Square Kilometer Array (SKA), will affect the search for this elusive class of AGN. This small study was presented as a poster at the conference *The many facets of extragalactic radio surveys: towards new scientific challenges*, which took place in Bologna between October 20-23, 2015, and it was later published in Proceedings of Science.

6.1 $\log N - \log S$ test

A useful tool to investigate the space density of sources is the logN-logS test, which does not require the knowledge of the distance of each source. The test assumes that the shape of the luminosity function is the same within the sample, an assumption that appears reasonable for samples limited to relatively low redshifts. The test evaluates the number of sources above each flux density S, and is thus the cumulative distribution of sources as a function of the flux.

The test in the Euclidean space is relatively simple. The total number of sources that will be found in a volume element $\mathrm{d}V$ is

$$\mathrm{d}\mathcal{N} = n(r)\mathrm{d}V = n(r)r^2\mathrm{d}r\mathrm{d}\Omega \, , \tag{6.1}$$

so the surface density of sources, or the number of sources per unit solid angle between r and $r + \mathrm{d}r$, is

$$\frac{\mathrm{d}\mathcal{N}}{\mathrm{d}\Omega} = n(r)r^2\mathrm{d}r \, . \tag{6.2}$$

The observed flux from a particular source at r is $F = L/4\pi r^2$. Now suppose that we detect all sources in a given field down to some limiting flux S, then all sources with $F \geq S$ are counted. This means that we detect sources out to some maximum distance

$$r_{max} = \left(\frac{L}{4\pi S}\right)^{1/2} \, . \tag{6.3}$$

The total number of sources per unit solid angle detected above the limiting flux S is thus

$$N(S) = \int \frac{\mathrm{d}\mathcal{N}}{\mathrm{d}\Omega}(F \geq S) = \int \frac{\mathrm{d}\mathcal{N}}{\mathrm{d}\Omega}(r \leq r_{max}) = \int_0^{r_{max}} n(r)r^2 \mathrm{d}r \ . \tag{6.4}$$

The quantity N(S) is thus the cumulative distribution of sources as a function of flux. For the case of a uniform density of objects $n(r) = n_0$, this becomes

$$N(S) = n_0 \frac{r_{max}^3}{3} = \frac{n_0}{3}\left(\frac{L}{4\pi S}\right)^{3/2} \ , \tag{6.5}$$

which in logarithmic form gives

$$\log N(S) = \log\left[\frac{n_0 L^{3/2}}{3(4\pi)^{3/2}}\right] - \frac{3}{2}\log S \ . \tag{6.6}$$

The number of sources brighter than some flux S should then be proportional to $S^{-3/2}$ for a constant density in the Euclidean space. The observational realization of this relationship is the logN-logS test, which can be used to test the hypothesis that the observed population has a constant space density. In this form, the test was developed to test the evolution of radio sources, so it is particularly well suited for our aim.

6.2   Square Kilometer Array

The Square Kilometer Array (SKA), with a collecting area of nearly 1 square kilometer, will be superior both in sensitivity and in observing speed to all present-day radio facilities. This instrument will be built in phases. The first (SKA 1) is expected to become fully operational by 2020, while the second (SKA 2) should become available around 2025, and it should increase the sensitivity of SKA 1 of about an order of magnitude[1].

The SKA will yield to a breakthrough in relativistic jets studies, allowing to image the full extent of jet radio emission, to characterize the polarization and to track the evolution of emission feature down the jet (Bicknell et al. 2004). Its longest baseline will be close to 3000 km, allowing a very high spatial resolution, even if not the highest. The Very Large Baseline Interferometer (VLBI), and also the Very Large Baseline Array (VLBA) have both a higher resolution, but the real strength of the SKA will be its incredible sensitivity, way higher than those of VLBI and VLBA.

SKA will ensure the possibility to unravel with high accuracy the global dynamics of jets. In particular it will allow us to probe the velocity field of the jet, through the tracking of moving knots and jet brightness profiles, and its changes along the flow, with important consequences on our understanding of jet dynamics. At the same time, the precise polarization measurements possible with SKA will permit to map the detailed structure of the magnetic fields in the jet (Murphy et al. 2013), allowing us to investigate the dynamical role of the magnetic field and its effects in the jet collimation. Finally, the coupling of high-resolution and high-sensitivity radio data with high-energy observations will allow us to deeply investigate all those topics related to the acceleration of relativistic particles in the jet. In particular, the radio data will provide accurate information on shock structure and dynamics which, coupled

---

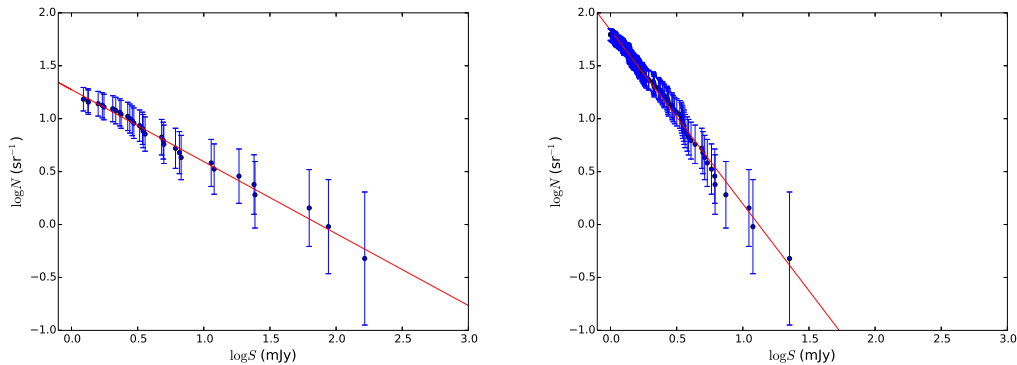[1]For further information, http://www.skatelescope.org

Figure 6.1 logN-logS test for radio-loud (top panel) and radio-quiet (medium panel) NLS1s and disk RGs (bottom panel).

to the information on the particle evolution, effectively probed by high-energy observations, will give us a clearer understanding of the mechanisms at the base of acceleration processes.

But what probably will be most relevant in the study of NLS1s is again its impressive sensitivity, which will allow us to map with unprecedented detail the structure of jets at large (> 1 pc) scales. Particularly important issues are the study of the global dynamics of jets (speed, stability) and the investigation of the extended structures (hot spots, lobes, knees in curved jets). These latter topics are also relevant for the study of the jet/environment interaction and the possible role in the AGN/galaxy and AGN/cluster feedback.

6.3   NLS1s samples

To better investigate the impact of SKA in the NLS1 study, I decided to use the samples of radio-emitting sources initially built for the luminosity functions. Although not adequate in that particular case, since I could not divide the radio-loud sample between flat- and steep-spectrum sources, they are helpful in this case.

I extracted from SDSS DR7 all the NLS1s at $z < 0.3$, using as classification criteria the FWHM(Hβ) < 2000 km s^{-1} and the ratio [O III]/H$\beta < 3$. Then I searched for a FIRST radio-source within a radius of 5 arcsec (Becker et al. 1995). Finally I calculated their radio-loudness in the usual way. The 5 GHz flux instead was obtained from the 1.4 GHz flux of FIRST assuming a spectral index $\alpha = 0.5$ (F$_\nu \propto \nu^{-\alpha}$, Yuan et al. 2008). Sources with RL > 10 were defined as radio-loud, otherwise they were considered radio-quiet. In this way I obtained 117 RQNLS1s, and 32 RLNLS1s.

I tested the samples by means of V/V$_{max}$ test as in Section 5.4 to investigate their completeness. The radio-quiet sample has $\langle$V/V$_{max}\rangle = 0.54\pm0.03$, while the radio-loud has $\langle$V/V$_{max}\rangle = 0.45\pm0.05$. Both the samples are then in agreement with the uniform distribution of sources, and they can be considered statistically complete.

6.4   Results

The results are shown in Fig. 6.1. The errors are Poissonian. The distribution of RQNLS1s is the closer one to the Euclidean distribution (slope $\beta = 1.64 \pm 0.01$), while RLNLS1s have

a flatter distribution ($\beta = 0.68 \pm 0.01$). The SKA 1 sensitivity at 1.4 GHz will be 0.082 mJy[2]. In our calculations we assume that the resulting slope is remaining the same at lower fluxes. This can be done in absence of evolutionary effects, that we do not expect to be particularly strong in our relatively low redshift domain. This simple extrapolation yields very large numbers: SKA might be able to identify ~1300 RLNLS1 and ~50000 RQNLS1s up to $z = 0.3$.

This important result, nevertheless, is only an upper limit, since there are a few caveats that must be kept in mind. In particular, regarding RLNLS1s, a decrease of one order of magnitude in radio flux must correspond to a similar decrease also in optical flux, otherwise the source would not be radio-loud anymore. It is then possible that SKA will not detect many more RLNLS1s, at least up to z = 0.3, although it will clearly allow a much deeper study of all currently known RLNLS1s. Conversely, at higher z, the number of new RLNLS1s can be largely increased, since there are many radio-loud sources with a flux density ~1 mJy that at larger distances are not visible for present-day observatories.

For RQNLS1s there are also a couple of caveats. First, it is unlikely that so many NLS1s exist up to $z = 0.3$, but this only means that SKA will be able to detect all the existing NLS1s. But whilst SKA will detect many more sources, it will be difficult to identify them as NLS1s without a deep optical observation. The radio luminosity is proportional to the [O III] line luminosity (de Bruyn & Wilson 1978), hence a low radio flux corresponds to an equally low [O III] flux. This makes the classification more and more difficult for weak sources.

Anyway, even with this optical limit, the knowledge increase on the nature of RQNLS1s will be very large. In particular, a deep radio investigation will provide helpful information on the dichotomy between radio-quiet and radio-loud sources. In turn it will also help us to unveil whether the origin of radio emission in RQNLS1s is due to the high star formation rate typical of NLS1s (Sani et al. 2010), or to some sort of weak activity that might be ongoing, such as an aborted or faint jet (Ghisellini et al. 2004; Doi et al. 2013). Nonetheless, it will also allow to study in detail the radio emission from RLNLS1s, investigating at very high resolution the morphology of the jets, and finally clarifying how strong the incidence of the starburst component is in these sources (Caccianiga et al. 2015). Last but not least, SKA will provide enough statistic to perform a detailed investigation on RLNLS1s by means of the radio luminosity function, allowing us to study their evolution through cosmic time.

---

[2]SKA-TEL-SKO-0000229 - Report and Options for Re-Baselining of SKA 1

Chapter 7

Conclusions

7.1 A unification of young AGN?

The aim of this thesis was to investigate the nature of the parent population of flat-spectrum radio-loud narrow-line Seyfert 1 galaxies, the third class of γ-ray emitting AGN harboring a relativistic beamed jet. In this work I faced the problem under different points of view, examining all the different parent candidates to find out which one was the best suited. The candidate sources were steep-spectrum radio-loud NLS1s, radio-quiet NLS1s and disk-hosted radio-galaxies, along with the high excitation radio-galaxies with a compact steep radio-spectrum.

S-NLS1s: the black hole mass and Eddington ratio distributions of these candidates revealed that they are very likely part of the parent population. This result of course was somewhat expected, since RLNLS1s with jets viewed at large angles are the natural candidates to be parent sources. Nevertheless, their number is very low, and it is not clear whether they represent the whole type 1 parent population, or if they are only a fraction of it.

Disk RGs: in this case the black hole mass distribution revealed that this class of quite rare sources are similar to a bridge connecting RLNLS1s with the giant elliptical RGs. Some of these sources, whose mass is relatively low, are suitable candidates as parent sources. This might indicate that the BLR in NLS1s actually has some flattened component, even if I could not determine how strong this component is. Nevertheless it is very likely that virtually all type 2 parent sources appear as disk-hosted radio-galaxies.

RQNLS1s: in this case the black hole mass study revealed that radio-quiet sources have a slightly different mass distribution with respect to F-NLS1s, even if their Eddington ratio is roughly the same. Nevertheless, such distributions are not very far from each other, therefore I decided to investigate them further, and to focus on their NLR. The detailed study on the [O III] lines profile revealed that there is a profound difference between the origin of gas perturbations in radio-quiet and radio-loud NLS1s. I conclude that the most likely origin for this difference is the presence of a relativistic jet interacting with the ISM in RLNLS1s, that is instead lacking in the vast majority of RQNLS1s. Therefore, I suggest that these sources can be excluded from the parent population.

CSS/HERGs: in the literature these sources were often suggested to be related with NLS1s. My work seem to confirm that they are not only relatives, but that they are the same kind of object observed under different inclinations. Both young sources with relativistic jets, CSS/HERGs have the same black hole mass distribution of NLS1s, a very high accretion

luminosity, and they might also be hosted in a disk-galaxy. But the most important thing is that the addition of relativistic beaming to their luminosity function indicates that they are a very good match for F-NLS1s parent population. This result is completely in agreement with the previously found parent sources. Several recent works confirmed that S-NLS1s can always be classified as CSS with a high-ionization spectrum. I suggest that many type 1 CSS can be likely classified as NLS1s. Those instead with larger permitted lines and rotational velocities might be those NLS1s with a flattened BLR, and hence might be part of the disk RGs class. The same is true for type 2 CSS/HERGs, which might be included among disk RGs as well.

7.2   Final remarks

The picture which emerges from these results has still several aspects that must be clarified. One of the most important points is the geometry of the BLR, which is very important to understand if disk RGs are part of the parent population. New generation instruments, such as EELT, will be definitely crucial to study the BLR in nearby NLS1s. But also numerical simulations can be helpful from this point of view, to understand whether the launching of a relativistic jet might have some impact on the BLR geometry. It was indeed observed that radio-loudness seems to have an effect on the BLR structure, which appears to be flatter in radio-loud sources (Kollatschny & Zetzl 2011).

Additional studies by means of spectropolarimetry can provide a large amount of information on the parent population. A large search for obscured RLNLS1s would help to characterize the parent sources, and to understand if they always appear as CSS/HERGs. Good candidates as obscured NLS1s already exist. One of them, NGC 5506, was included in this work, and its identification was done by means of infrared studies. New IR spectra from the new SDSS-BOSS survey (Ahn et al. 2014) have also allowed the discovery of another γ-NLS1s (Yao et al. 2015), and are the only way to find new RLNLS1s at high redshift.

I already discussed the huge impact that SKA will have on NLS1s study, and how it will likely allow to largely improve the number of known sources, giving us a chance to perform large statistical studies. Another radio survey, the VLASS (Myers et al. 2014), may be very helpful in this sense. It should consist in an all-sky survey at frequencies between 2-4 GHz, and this will lead to calculate the spectral indices for RLNLS1s without any specifically designed observation, allowing to separate steep- from flat-spectrum RLNLS1s.

Last but not least, one of the most important topic that must be faced is the host galaxy of high z NLS1s and, of course, of CSS/HERGs. Although the host galaxy of CSS/HERGs has been often investigated, a more detailed study should be carried out to understand whether these sources are actually hosted by disk or starburst galaxies. The same should be done for γ-ray emitting NLS1s, and at the same time their environment should be carefully examined. While NLS1s are tipically considered to be the product of secular evolution, CSS are instead often associated with mergers. Finally, the interaction of the relativistic jet with the ISM was studied several times in CSS, but an akin work on NLS1s should be carried out, for instance with new instruments such as MUSE/VLT, to understand how a relatively low power jet launched by a low mass black hole can affect the surrounding medium.

In conclusion, several works should be carried out in the open field of NLS1s, and all of them will help to shed light on the evolution of AGN with cosmic time and, in turn, on the evolution of our Universe.

Bibliography

Abazajian, K. N., Adelman-McCarthy, J. K., Agüeros, M. A., Allam, S. S., Allende Prieto, C., An, D., Anderson, K. S. J., Anderson, S. F., Annis, J., Bahcall, N. A., & et al. 2009, ApJS, 182, 543

Abdo, A. A., Ackermann, M., Ajello, M., Axelsson, M., Baldini, L., Ballet, J., Barbiellini, G., Bastieri, D., Battelino, M., & Baughman, B. M. e. a. 2009a, ApJ, 699, 976

Abdo, A. A., Ackermann, M., Ajello, M., Baldini, L., Ballet, J., Barbiellini, G., Bastieri, D., Bechtol, K., Bellazzini, R., & Berenji, B. e. a. 2009b, ApJ, 707, L142

Ahn, C. P., Alexandroff, R., Allende Prieto, C., Anders, F., Anderson, S. F., Anderton, T., Andrews, B. H., Aubourg, É., Bailey, S., Bastien, F. A., & et al. 2014, ApJS, 211, 17

Antón, S., Browne, I. W. A., & Marchã, M. J. 2008, A&A, 490, 583

Antonucci, R. 1993, ARA&A, 31, 473

Antonucci, R. R. J., & Miller, J. S. 1985, ApJ, 297, 621

Aoki, K., Kawaguchi, T., & Ohta, K. 2005, ApJ, 618, 601

Avni, Y., & Bahcall, J. N. 1980, ApJ, 235, 694

Axon, D. J., Capetti, A., Fanti, R., Morganti, R., Robinson, A., & Spencer, R. 2000, AJ, 120, 2284

Balbus, S. A., & Hawley, J. F. 1991, ApJ, 376, 214

Barvainis, R. 1987, ApJ, 320, 537

Barway, S., Mayya, Y. D., Kembhavi, A. K., & Pandey, S. K. 2005, AJ, 129, 630

Becker, R. H., White, R. L., & Helfand, D. J. 1995, ApJ, 450, 559

Beckmann, V., & Shrader, C. R. 2012, Active Galactic Nuclei

Bennert, N., Falcke, H., Shchekinov, Y., & Wilson, A. S. 2004, in IAU Symposium, Vol. 222, The Interplay Among Black Holes, Stars and ISM in Galactic Nuclei, ed. T. Storchi-Bergmann, L. C. Ho, & H. R. Schmitt, 307–308

Berton, M. 2010, Master's thesis, Università di Padova

Berton, M., Caccianiga, A., Foschini, L., Peterson, B. M., Mathur, S., Terreran, G., Ciroi, S., Congiu, E., Cracco, V., Frezzato, M., La Mura, G., & Rafanelli, P. 2016a, ArXiv e-prints

Berton, M., Foschini, L., Caccianiga, A., Richards, J. L., Ciroi, S., Congiu, E., Cracco, V., La Mura, G., Marafatto, L., & Rafanelli, P. 2016b, ArXiv e-prints

Berton, M., Foschini, L., Ciroi, S., Caccianiga, A., Cracco, V., La Mura, G., Di Mille, F., Lister, M. L., Mathur, S., Peterson, B. M., Richards, J. L., Congiu, E., Frezzato, M., & Rafanelli, P. 2015a, ArXiv e-prints

Berton, M., Foschini, L., Ciroi, S., Cracco, V., La Mura, G., Di Mille, F., & Rafanelli, P. 2015b, ArXiv e-prints

Berton, M., Foschini, L., Ciroi, S., Cracco, V., La Mura, G., Lister, M. L., Mathur, S., Peterson, B. M., Richards, J. L., & Rafanelli, P. 2015c, A&A, 578, A28

Best, P. N., & Heckman, T. M. 2012, MNRAS, 421, 1569

Best, P. N., Kauffmann, G., Heckman, T. M., Brinchmann, J., Charlot, S., Ivezić, Ž., & White, S. D. M. 2005, MNRAS, 362, 25

Bian, W., Yuan, Q., & Zhao, Y. 2005, MNRAS, 364, 187

Bicknell, G. V., Jones, D. L., & Lister, M. 2004, New Astron. Rev., 48, 1151

Blandford, R. D., & McKee, C. F. 1982, ApJ, 255, 419

Blandford, R. D., & Payne, D. G. 1982, MNRAS, 199, 883

Blandford, R. D., & Rees, M. J. 1978, in BL Lac Objects, ed. A. M. Wolfe, 328–341

Blandford, R. D., & Znajek, R. L. 1977, MNRAS, 179, 433

Boettcher, M., Harris, D. E., & Krawczynski, H. 2012, Relativistic Jets from Active Galactic Nuclei

Boller, T., Brandt, W. N., & Fink, H. 1996, A&A, 305, 53

Boroson, T. A., & Green, R. F. 1992, ApJS, 80, 109

Botte, V., Ciroi, S., di Mille, F., Rafanelli, P., & Romano, A. 2005, MNRAS, 356, 789

Botte, V., Ciroi, S., Rafanelli, P., & Di Mille, F. 2004, AJ, 127, 3168

Bridle, A. H. 1986, Canadian Journal of Physics, 64, 353

Brunthaler, A., Falcke, H., Bower, G. C., Aller, M. F., Aller, H. D., & Teräsranta, H. 2005, A&A, 435, 497

Brunthaler, A., Falcke, H., Bower, G. C., Aller, M. F., Aller, H. D., Teräsranta, H., Lobanov, A. P., Krichbaum, T. P., & Patnaik, A. R. 2000, A&A, 357, L45

Caccianiga, A., Antón, S., Ballo, L., Dallacasa, D., Della Ceca, R., Fanali, R., Foschini, L., Hamilton, T., Kraus, A., Maccacaro, T., Mack, K.-H., Marchã, M. J., Paulino-Afonso, A., Sani, E., & Severgnini, P. 2014, MNRAS, 441, 172

Caccianiga, A., Antón, S., Ballo, L., Foschini, L., Maccacaro, T., Della Ceca, R., Severgnini, P., Marchã, M. J., Mateos, S., & Sani, E. 2015, MNRAS, 451, 1795

Calderone, G., Ghisellini, G., Colpi, M., & Dotti, M. 2013, MNRAS, 431, 210

Capetti, A., de Ruiter, H. R., Fanti, R., Morganti, R., Parma, P., & Ulrich, M.-H. 2000, A&A, 362, 871

Cavaliere, A., & D'Elia, V. 2002, ApJ, 571, 226

Cherepashchuk, A. M., & Lyutyi, V. M. 1973, Astrophys. Lett., 13, 165

Cohen, M. H., Ogle, P. M., Tran, H. D., Goodrich, R. W., & Miller, J. S. 1999, AJ, 118, 1963

Collin, S., Kawaguchi, T., Peterson, B. M., & Vestergaard, M. 2006, A&A, 456, 75

Crenshaw, D. M., Kraemer, S. B., & Gabel, J. R. 2003, AJ, 126, 1690

Curtis, H. D. 1918, Publications of Lick Observatory, 13, 9

Czerny, B., Siemiginowska, A., Janiuk, A., Nikiel-Wroczyński, B., & Stawarz, Ł. 2009, ApJ, 698, 840

D'Ammando, F., Orienti, M., Finke, J., Raiteri, C. M., Angelakis, E., Fuhrmann, L., Giroletti, M., Hovatta, T., Max-Moerbeck, W., Perkins, J. S., Readhead, A. C. S., Richards, J. L., Stawarz, Ł., & Donato, D. 2012, MNRAS, 426, 317

D'Ammando, F., Orienti, M., Larsson, J., & Giroletti, M. 2015, MNRAS, 452, 520

Davidson, K., & Kinman, T. D. 1978, ApJ, 225, 776

de Bruyn, A. G., & Wilson, A. S. 1978, A&A, 64, 433

Decarli, R., Dotti, M., Fontana, M., & Haardt, F. 2008, MNRAS, 386, L15

Denney, K. D., De Rosa, G., Croxall, K., Gupta, A., Bentz, M. C., Fausnaugh, M. M., Grier, C. J., Martini, P., Mathur, S., Peterson, B. M., Pogge, R. W., & Shappee, B. J. 2014, ApJ, 796, 134

Deo, R. P., Crenshaw, D. M., & Kraemer, S. B. 2006, AJ, 132, 321

Doi, A., Asada, K., Fujisawa, K., Nagai, H., Hagiwara, Y., Wajima, K., & Inoue, M. 2013, ApJ, 765, 69

Doi, A., Asada, K., & Nagai, H. 2011, ApJ, 738, 126

Doi, A., Fujisawa, K., Inoue, M., Wajima, K., Nagai, H., Harada, K., Suematsu, K., Habe, A., Honma, M., Kawaguchi, N., Kawai, E., Kobayashi, H., Koyama, Y., Kuboki, H., Murata, Y., Omodaka, T., Sorai, K., Sudou, H., Takaba, H., Takashima, K., Takeda, K., Tamura, S., & Wakamatsu, K.-I. 2007, PASJ, 59, 703

Doi, A., Nagai, H., Asada, K., Kameno, S., Wajima, K., & Inoue, M. 2006, PASJ, 58, 829

Doi, A., Nagira, H., Kawakatu, N., Kino, M., Nagai, H., & Asada, K. 2012, ApJ, 760, 41

Doi, A., Wajima, K., Hagiwara, Y., & Inoue, M. 2015, ApJ, 798, L30

D'Onofrio, M., Marziani, P., & Sulentic, J. W. 2012, Fifty Years of Quasars: From Early Observations and Ideas to Future Research, 386

Elitzur, M. 2012, ApJ, 747, L33

Falcke, H., & Biermann, P. L. 1999, A&A, 342, 49

Fanaroff, B. L., & Riley, J. M. 1974, MNRAS, 167, 31P

Fanti, C., Fanti, R., Dallacasa, D., Schilizzi, R. T., Spencer, R. E., & Stanghellini, C. 1995, A&A, 302, 317

Ferland, G. J., & Mushotzky, R. F. 1982, ApJ, 262, 564

Ferrarese, L., & Merritt, D. 2000, ApJ, 539, L9

Floyd, D. J. E., Perlman, E., Leahy, J. P., Beswick, R. J., Jackson, N. J., Sparks, W. B., Axon, D. J., & O'Dea, C. P. 2006, ApJ, 639, 23

Foschini, L. 2011a, Research in Astronomy and Astrophysics, 11, 1266

Foschini, L. 2011b, in Narrow-Line Seyfert 1 Galaxies and their Place in the Universe, Vol. NLS1, id. 24

—. 2012a, Research in Astronomy and Astrophysics, 12, 359

Foschini, L. 2012b, in Proceedings of Nuclei of Seyfert galaxies and QSOs - Central engine & conditions of star formation (Seyfert 2012), 10

—. 2014, International Journal of Modern Physics Conference Series, 28, 1460188

Foschini, L., Angelakis, E., Fuhrmann, L., Ghisellini, G., Hovatta, T., Lahteenmaki, A., Lister, M. L., Braito, V., Gallo, L., Hamilton, T. S., Kino, M., Komossa, S., Pushkarev, A. B., Thompson, D. J., Tibolla, O., Tramacere, A., Carramiñana, A., Carrasco, L., Falcone, A., Giroletti, M., Grupe, D., Kovalev, Y. Y., Krichbaum, T. P., Max-Moerbeck, W., Nestoras, I., Pearson, T. J., Porras, A., Readhead, A. C. S., Recillas, E., Richards, J. L., Riquelme, D., Sievers, A., Tammi, J., Tornikoski, M., Ungerechts, H., Zensus, J. A., Celotti, A., Bonnoli, G., Doi, A., Maraschi, L., Tagliaferri, G., & Tavecchio, F. 2012, A&A, 548, A106

Foschini, L., Berton, M., Caccianiga, A., Ciroi, S., Cracco, V., Peterson, B. M., Angelakis, E., Braito, V., Fuhrmann, L., Gallo, L., Grupe, D., Järvelä, E., Kaufmann, S., Komossa, S., Kovalev, Y. Y., Lähteenmäki, A., Lisakov, M. M., Lister, M. L., Mathur, S., Richards, J. L., Romano, P., Sievers, A., Tagliaferri, G., Tammi, J., Tibolla, O., Tornikoski, M., Vercellone, S., La Mura, G., Maraschi, L., & Rafanelli, P. 2015, A&A, 575, A13

Foschini, L., Fermi/Lat Collaboration, Ghisellini, G., Maraschi, L., Tavecchio, F., & Angelakis, E. 2010, in Astronomical Society of the Pacific Conference Series, Vol. 427, Accretion and Ejection in AGN: a Global View, ed. L. Maraschi, G. Ghisellini, R. Della Ceca, & F. Tavecchio, 243–248

Fossati, G., Maraschi, L., Celotti, A., Comastri, A., & Ghisellini, G. 1998, MNRAS, 299, 433

Franceschini, A., Vercellone, S., & Fabian, A. C. 1998, MNRAS, 297, 817

Gallo, L. C. 2006, MNRAS, 368, 479

Gallo, L. C., Edwards, P. G., Ferrero, E., Kataoka, J., Lewis, D. R., Ellingsen, S. P., Misanovic, Z., Welsh, W. F., Whiting, M., Boller, T., Brinkmann, W., Greenhill, J., & Oshlack, A. 2006, MNRAS, 370, 245

Garofalo, D., Evans, D. A., & Sambruna, R. M. 2010, MNRAS, 406, 975

Gehrels, N. 1986, ApJ, 303, 336

Ghisellini, G., Celotti, A., Fossati, G., Maraschi, L., & Comastri, A. 1998, MNRAS, 301, 451

Ghisellini, G., Haardt, F., & Matt, G. 2004, A&A, 413, 535

Ghisellini, G., & Tavecchio, F. 2009, MNRAS, 397, 985

Ghisellini, G., Tavecchio, F., Foschini, L., Ghirlanda, G., Maraschi, L., & Celotti, A. 2010, MNRAS, 402, 497

Ghosh, P., & Abramowicz, M. A. 1997, MNRAS, 292, 887

Giommi, P., Padovani, P., Polenta, G., Turriziani, S., D'Elia, V., & Piranomonte, S. 2012, MNRAS, 420, 2899

Giroletti, M., & Panessa, F. 2009, ApJ, 706, L260

Giroletti, M., Pavlidou, V., Reimer, A., Taylor, G. B., Tosti, G., Giovannini, G., Casadio, C., Liuzzo, E., & Tamburri, S. 2012, Advances in Space Research, 49, 1320

Gliozzi, M., Papadakis, I. E., Grupe, D., Brinkmann, W. P., Raeth, C., & Kedziora-Chudczer, L. 2010, ApJ, 717, 1243

Goodlet, J. A., Kaiser, C. R., Best, P. N., & Dennett-Thorpe, J. 2004, MNRAS, 347, 508

Goodrich, R. W. 1989, ApJ, 342, 224

Greene, J. E., & Ho, L. C. 2005a, ApJ, 627, 721

—. 2005b, ApJ, 630, 122

Greene, J. E., Hood, C. E., Barth, A. J., Bennert, V. N., Bentz, M. C., Filippenko, A. V., Gates, E., Malkan, M. A., Treu, T., Walsh, J. L., & Woo, J.-H. 2010, ApJ, 723, 409

Grupe, D. 2000, New Astron. Rev., 44, 455

Gu, M., & Chen, Y. 2010, AJ, 139, 2612

Gu, M., Chen, Y., Komossa, S., Yuan, W., Shen, Z., Wajima, K., Zhou, H., & Zensus, J. A. 2015, ApJS, 221, 3

Hada, K., Doi, A., Nagai, H., Inoue, M., Honma, M., Giroletti, M., & Giovannini, G. 2013, ApJ, 779, 6

Hamilton, T. S., Casertano, S., & Turnshek, D. A. 2002, ApJ, 576, 61

Hamilton, T. S., & Foschini, L. 2012, AAS, 220

Hardcastle, M. J., Evans, D. A., & Croston, J. H. 2007, MNRAS, 376, 1849

Heckman, T. M. 1980, A&A, 87, 152

Heckman, T. M., Kauffmann, G., Brinchmann, J., Charlot, S., Tremonti, C., & White,
    S. D. M. 2004, ApJ, 613, 109

Heinz, S., & Sunyaev, R. A. 2003, MNRAS, 343, L59

Heisler, C. A., & Vader, J. P. 1995, AJ, 110, 87

Ho, L. C. 2002, ApJ, 564, 120

Ho, L. C., & Kim, M. 2014, ApJ, 789, 17

Ho, L. C., & Peng, C. Y. 2001, ApJ, 555, 650

Holt, J. 2009, Astronomische Nachrichten, 330, 226

Hota, A., Rey, S.-C., Kang, Y., Kim, S., Matsushita, S., & Chung, J. 2012, MNRAS, 422,
    L38

Hota, A., Sirothia, S. K., Ohyama, Y., Konar, C., Kim, S., Rey, S.-C., Saikia, D. J., Croston,
    J. H., & Matsushita, S. 2011, MNRAS, 417, L36

Hou, A., Parker, L. C., Harris, W. E., & Wilman, D. J. 2009, ApJ, 702, 1199

Inskip, K. J., Tadhunter, C. N., Morganti, R., Holt, J., Ramos Almeida, C., & Dicken, D.
    2010, MNRAS, 407, 1739

Jackson, N., Beswick, R., Pedlar, A., Cole, G. H., Sparks, W. B., Leahy, J. P., Axon, D. J.,
    & Holloway, A. J. 2003, MNRAS, 338, 643

Järvelä, E., Lähteenmäki, A., & León-Tavares, J. 2015, A&A, 573, A76

Kadler, M., Eisenacher, D., Ros, E., Mannheim, K., Elsässer, D., & Bach, U. 2012, A&A,
    538, L1

Kalberla, P. M. W., Burton, W. B., Hartmann, D., Arnal, E. M., Bajaja, E., Morras, R., &
    Pöppel, W. G. L. 2005, A&A, 440, 775

Kawaguchi, T., & Mori, M. 2010, ApJ, 724, L183

Keel, W. C. 1980, AJ, 85, 198

Kellermann, K. I., & Pauliny-Toth, I. I. K. 1969, ApJ, 155, L71

Kellermann, K. I., Sramek, R., Schmidt, M., Shaffer, D. B., & Green, R. 1989, AJ, 98, 1195

Khachikian, E. Y., & Weedman, D. W. 1974, ApJ, 192, 581

King, A. R., Pringle, J. E., & Livio, M. 2007, MNRAS, 376, 1740

Kinney, A. L., Calzetti, D., Bohlin, R. C., McQuade, K., Storchi-Bergmann, T., & Schmitt, H. R. 1996, ApJ, 467, 38

Kollatschny, W., & Zetzl, M. 2011, Nature, 470, 366

Komatsu, E., Smith, K. M., Dunkley, J., Bennett, C. L., Gold, B., Hinshaw, G., Jarosik, N., Larson, D., Nolta, M. R., Page, L., Spergel, D. N., Halpern, M., Hill, R. S., Kogut, A., Limon, M., Meyer, S. S., Odegard, N., Tucker, G. S., Weiland, J. L., Wollack, E., & Wright, E. L. 2011, ApJS, 192, 18

Komossa, S., & Meerschweinchen, J. 2000, A&A, 354, 411

Komossa, S., Voges, W., Xu, D., Mathur, S., Adorf, H.-M., Lemson, G., Duschl, W. J., & Grupe, D. 2006, AJ, 132, 531

Komossa, S., Xu, D., Fuhrmann, L., Grupe, D., Yao, S., Fan, Z., Myserlis, I., Angelakis, E., Karamanavis, V., Yuan, W., & Zensus, J. A. 2015, A&A, 574, A121

Komossa, S., Xu, D., Zhou, H., Storchi-Bergmann, T., & Binette, L. 2008, ApJ, 680, 926

Koratkar, A. P., & Gaskell, C. M. 1991, ApJ, 370, L61

Kovačević, J., Popović, L. Č., & Dimitrijević, M. S. 2010, ApJS, 189, 15

Kozieł-Wierzbowska, D., & Stasińska, G. 2011, MNRAS, 415, 1013

Krolik, J. H., & Begelman, M. C. 1988, ApJ, 329, 702

Kunert-Bajraszewska, M., Gawroński, M. P., Labiano, A., & Siemiginowska, A. 2010, MNRAS, 408, 2261

Kunert-Bajraszewska, M., & Labiano, A. 2010, MNRAS, 408, 2279

La Mura, G., Di Mille, F., Ciroi, S., Popović, L. Č., & Rafanelli, P. 2009, ApJ, 693, 1437

Laing, R. A., Jenkins, C. R., Wall, J. V., & Unger, S. W. 1994, in Astronomical Society of the Pacific Conference Series, Vol. 54, The Physics of Active Galaxies, ed. G. V. Bicknell, M. A. Dopita, & P. J. Quinn, 201

LaMassa, S. M., Schawinski, K., Parejko, J., Urry, C., Masters, K., Keel, W., & Lintott, C. 2012, in American Astronomical Society Meeting Abstracts, Vol. 220, American Astronomical Society Meeting Abstracts #220, #335.24

Lamastra, A., Bianchi, S., Matt, G., Perola, G. C., Barcons, X., & Carrera, F. J. 2009, A&A, 504, 73

Leahy, J. P. 1993, in Lecture Notes in Physics, Berlin Springer Verlag, Vol. 421, Jets in Extragalactic Radio Sources, ed. H.-J. Röser & K. Meisenheimer, 1

León Tavares, J., Kotilainen, J., Chavushyan, V., Añorve, C., Puerari, I., Cruz-González, I., Patiño-Alvarez, V., Antón, S., Carramiñana, A., Carrasco, L., Guichard, J., Karhunen, K., Olguín-Iglesias, A., Sanghvi, J., & Valdes, J. 2014, ApJ, 795, 58

Letawe, G., Magain, P., Courbin, F., Jablonka, P., Jahnke, K., Meylan, G., & Wisotzki, L. 2007, MNRAS, 378, 83

Liao, N.-H., Liang, Y.-F., Weng, S.-S., Gu, M.-F., & Fan, Y.-Z. 2015, ArXiv e-prints

Lintott, C. J., Schawinski, K., Slosar, A., Land, K., Bamford, S., Thomas, D., Raddick, M. J., Nichol, R. C., Szalay, A., Andreescu, D., Murray, P., & Vandenberg, J. 2008, MNRAS, 389, 1179

Ludwig, R. R., Greene, J. E., Barth, A. J., & Ho, L. C. 2012, ApJ, 756, 51

Lynden-Bell, D. 1969, Nature, 223, 690

Lyutyi, V. M., & Cherepashchuk, A. M. 1972, Astronomicheskij Tsirkulyar, 688

Markarian, B. E. 1963, Soobshcheniya Byurakanskoj Observatorii Akademiya Nauk Armyanskoj SSR Erevan, 34, 3

Marziani, P., Zamanov, R. K., Sulentic, J. W., & Calvani, M. 2003, MNRAS, 345, 1133

Mastichiadis, A., & Kirk, J. G. 1997, A&A, 320, 19

Mathur, S. 2000, MNRAS, 314, L17

Mathur, S., Fields, D., Peterson, B. M., & Grupe, D. 2012, ApJ, 754, 146

McKernan, B., Ford, K. E. S., & Reynolds, C. S. 2010, MNRAS, 407, 2399

Moderski, R., & Sikora, M. 1996, MNRAS, 283, 854

Moran, E. C. 2000, New Astron. Rev., 44, 527

Morganti, R., Holt, J., Tadhunter, C., Ramos Almeida, C., Dicken, D., Inskip, K., Oosterloo, T., & Tzioumis, T. 2011, A&A, 535, A97

Morganti, R., Oosterloo, T., Oonk, J. B. R., Frieswijk, W., & Tadhunter, C. 2015, A&A, 580, A1

Mortlock, D. J., Warren, S. J., Venemans, B. P., Patel, M., Hewett, P. C., McMahon, R. G., Simpson, C., Theuns, T., Gonzáles-Solares, E. A., Adamson, A., Dye, S., Hambly, N. C., Hirst, P., Irwin, M. J., Kuiper, E., Lawrence, A., & Röttgering, H. J. A. 2011, Nature, 474, 616

Mulchaey, J. S., Wilson, A. S., Bower, G. A., Heckman, T. M., Krolik, J. H., & Miley, G. K. 1994, ApJ, 433, 625

Mullaney, J. R., Alexander, D. M., Fine, S., Goulding, A. D., Harrison, C. M., & Hickox, R. C. 2013, MNRAS, 433, 622

Mundell, C. G., Ferruit, P., Nagar, N., & Wilson, A. S. 2009, ApJ, 703, 802

Mundell, C. G., Wilson, A. S., Ulvestad, J. S., & Roy, A. L. 2000, ApJ, 529, 816

Murgia, M., Fanti, C., Fanti, R., Gregorini, L., Klein, U., Mack, K.-H., & Vigotti, M. 1999, A&A, 345, 769

Murphy, E., Cawthorne, T. V., & Gabuzda, D. C. 2013, MNRAS, 430, 1504

Myers, S. T., Baum, S. A., & Chandler, C. J. 2014, in American Astronomical Society Meeting Abstracts, Vol. 223, American Astronomical Society Meeting Abstracts #223, 236.01

Nagar, N. M., Oliva, E., Marconi, A., & Maiolino, R. 2002, A&A, 391, L21

Nelson, C. H., & Whittle, M. 1996, ApJ, 465, 96

Nenkova, M., Sirocky, M. M., Ivezić, Ž., & Elitzur, M. 2008a, ApJ, 685, 147

Nenkova, M., Sirocky, M. M., Nikutta, R., Ivezić, Ž., & Elitzur, M. 2008b, ApJ, 685, 160

Neronov, A., Semikoz, D., & Vovk, I. 2010, A&A, 519, L6

Nesvadba, N. P. H., Lehnert, M. D., De Breuck, C., Gilbert, A. M., & van Breugel, W. 2008, A&A, 491, 407

Noel-Storr, J., Baum, S. A., Verdoes Kleijn, G., van der Marel, R. P., O'Dea, C. P., de Zeeuw, P. T., & Carollo, C. M. 2003, ApJS, 148, 419

Ochner, P., Berton, M., Pastorello, A., Benetti, S., Cappellaro, E., Elias-Rosa, N., Tartaglia, L., Terreran, G., Tomasella, L., & Turatto, M. 2015, The Astronomer's Telegram, 7909, 1

O'Dea, C. P. 1998, PASP, 110, 493

O'Dea, C. P., & Baum, S. A. 1997, AJ, 113, 148

Orban de Xivry, G., Davies, R., Schartmann, M., Komossa, S., Marconi, A., Hicks, E., Engel, H., & Tacconi, L. 2011, MNRAS, 417, 2721

Orienti, M. 2015, ArXiv e-prints

Oshlack, A. Y. K. N., Webster, R. L., & Whiting, M. T. 2001, ApJ, 558, 578

Osterbrock, D. E. 1981, ApJ, 249, 462

—. 1991, Reports on Progress in Physics, 54, 579

Osterbrock, D. E., & Pogge, R. W. 1985, ApJ, 297, 166

Owsianik, I., & Conway, J. E. 1998, A&A, 337, 69

Padovani, P., & Giommi, P. 1995, ApJ, 444, 567

Padovani, P., & Urry, C. M. 1992, ApJ, 387, 449

Paturel, G., Petit, C., Prugniel, P., Theureau, G., Rousseau, J., Brouty, M., Dubois, P., & Cambrésy, L. 2003, A&A, 412, 45

Pedlar, A., Unger, S. W., & Dyson, J. E. 1985, MNRAS, 214, 463

Peterson, B. M. 1997, An Introduction to Active Galactic Nuclei

—. 2008, New Astron. Rev., 52, 240

Peterson, B. M. 2011, in Narrow-Line Seyfert 1 Galaxies and their Place in the Universe, 32

Peterson, B. M., Ferrarese, L., Gilbert, K. M., Kaspi, S., Malkan, M. A., Maoz, D., Merritt, D., Netzer, H., Onken, C. A., Pogge, R. W., Vestergaard, M., & Wandel, A. 2004, ApJ, 613, 682

Peterson, B. M., McHardy, I. M., Wilkes, B. J., Berlind, P., Bertram, R., Calkins, M., Collier, S. J., Huchra, J. P., Mathur, S., Papadakis, I., Peters, J., Pogge, R. W., Romano, P., Tokarz, S., Uttley, P., Vestergaard, M., & Wagner, R. M. 2000, ApJ, 542, 161

Pogge, R. W. 1988, ApJ, 328, 519

Poutanen, J., & Stern, B. 2010, ApJ, 717, L118

Pozo Nuñez, F., Westhues, C., Ramolla, M., Bruckmann, C., Haas, M., Chini, R., Steenbrugge, K., Lemke, R., & Murphy, M. 2013, A&A, 552, A1

Proga, D., Stone, J. M., & Kallman, T. R. 2000, ApJ, 543, 686

Rawlings, S., & Saunders, R. 1991, Nature, 349, 138

Readhead, A. C. S., Taylor, G. B., Pearson, T. J., & Wilkinson, P. N. 1996, ApJ, 460, 634

Rector, T. A., Stocke, J. T., & Ellingson, E. 1995, AJ, 110, 1492

Rees, M. J. 1966, Nature, 211, 468

Remillard, R. A., Bradt, H. V., Buckley, D. A. H., Roberts, W., Schwartz, D. A., Tuohy, I. R., & Wood, K. 1986, ApJ, 301, 742

Richards, G. T., Fan, X., Newberg, H. J., Strauss, M. A., Vanden Berk, D. E., Schneider, D. P., Yanny, B., Boucher, A., Burles, S., Frieman, J. A., Gunn, J. E., Hall, P. B., Ivezić, Ž., Kent, S., Loveday, J., Lupton, R. H., Rockosi, C. M., Schlegel, D. J., Stoughton, C., SubbaRao, M., & York, D. G. 2002, AJ, 123, 2945

Richards, J. L., & Lister, M. L. 2015, ApJ, 800, L8

Risaliti, G., Salvati, M., & Marconi, A. 2011, MNRAS, 411, 2223

Robson, I. 1996, Active galactic nuclei

Salpeter, E. E. 1964, ApJ, 140, 796

Sambruna, R. M., Maraschi, L., & Urry, C. M. 1996, ApJ, 463, 444

Sani, E., Lutz, D., Risaliti, G., Netzer, H., Gallo, L. C., Trakhtenbrot, B., Sturm, E., & Boller, T. 2010, MNRAS, 403, 1246

Schawinski, K., Urry, C. M., Virani, S., Coppi, P., Bamford, S. P., Treister, E., Lintott, C. J., Sarzi, M., Keel, W. C., Kaviraj, S., Cardamone, C. N., Masters, K. L., Ross, N. P., Andreescu, D., Murray, P., Nichol, R. C., Raddick, M. J., Slosar, A., Szalay, A. S., Thomas, D., & Vandenberg, J. 2010, ApJ, 711, 284

Schmidt, M. 1963, Nature, 197, 1040

—. 1968, ApJ, 151, 393

Schmidt, M., & Green, R. F. 1983, ApJ, 269, 352

Schönell, A. J., Riffel, R. A., Storchi-Bergmann, T., & Winge, C. 2014, MNRAS, 445, 414

Schulz, R., Kreikenbohm, A., Kadler, M., Ojha, R., Ros, E., Stevens, J., Edwards, P. G.,
   Carpenter, B., Elsässer, D., Gehrels, N., Großberger, C., Hase, H., Horiuchi, S., Lovell,
   J. E. J., Mannheim, K., Markowitz, A., Müller, C., Phillips, C., Plötz, C., Quick, J.,
   Trüstedt, J., Tzioumis, A. K., & Wilms, J. 2015, ArXiv e-prints

Seyfert, C. K. 1943, ApJ, 97, 28

Shakura, N. I., & Sunyaev, R. A. 1973, A&A, 24, 337

Shapovalova, A. I., Popović, L. Č., Burenkov, A. N., Chavushyan, V. H., Ilić, D., Kovačević,
   A., Kollatschny, W., Kovačević, J., Bochkarev, N. G., Valdes, J. R., Torrealba, J., León-
   Tavares, J., Mercado, A., Benítez, E., Carrasco, L., Dultzin, D., & de la Fuente, E. 2012,
   ApJS, 202, 10

Shappee, B. J., Prieto, J. L., Nugent, J., Kochanek, C. S., Stanek, K. Z., Jencson, J., Talabere,
   A., Beacom, J. F., Szczygiel, D., Pojmanski, G., Dubberley, M., Elphick, M., Foale, S.,
   Hawkins, E., Mullens, D., Rosing, W., Ross, R., & Walker, Z. 2013, The Astronomer's
   Telegram, 5010, 1

Shen, Y., & Ho, L. C. 2014, Nature, 513, 210

Shlosman, I., Frank, J., & Begelman, M. C. 1989, Nature, 338, 45

Soldi, S., Beckmann, V., Gehrels, N., de Jong, S., & Lubiński, P. 2011, in Narrow-Line Seyfert
   1 Galaxies and their Place in the Universe, 63

Son, D., Woo, J.-H., Kim, S. C., Fu, H., Kawakatu, N., Bennert, V. N., Nagao, T., & Park,
   D. 2012, ApJ, 757, 140

Stickel, M., Padovani, P., Urry, C. M., Fried, J. W., & Kuehr, H. 1991, ApJ, 374, 431

Stocke, J. T., Danforth, C. W., & Perlman, E. S. 2011, ApJ, 732, 113

Su, M., Slatyer, T. R., & Finkbeiner, D. P. 2010, ApJ, 724, 1044

Surace, J. A., Sanders, D. B., & Evans, A. S. 2001, AJ, 122, 2791

Tadhunter, C., Wills, K., Morganti, R., Oosterloo, T., & Dickson, R. 2001, MNRAS, 327, 227

Tarchi, A., Castangia, P., Columbano, A., Panessa, F., & Braatz, J. A. 2011, A&A, 532, A125

Terlevich, R., & Melnick, J. 1985, MNRAS, 213, 841

Thean, A., Pedlar, A., Kukula, M. J., Baum, S. A., & O'Dea, C. P. 2000, MNRAS, 314, 573

Thorne, K. S. 1974, ApJ, 191, 507

Tsang, O., & Kirk, J. G. 2007, A&A, 463, 145

Ulvestad, J. S., Wong, D. S., Taylor, G. B., Gallimore, J. F., & Mundell, C. G. 2005, AJ, 130, 936

Urry, C. M., & Padovani, P. 1991, ApJ, 371, 60

—. 1995, PASP, 107, 803

Urry, C. M., & Shafer, R. A. 1984, ApJ, 280, 569

van Paradijs, J., & Bleeker, J. A. M., eds. 1999, Lecture Notes in Physics, Berlin Springer Verlag, Vol. 520, X-Ray Spectroscopy in Astrophysics

Vaona, L., Ciroi, S., Di Mille, F., Cracco, V., La Mura, G., & Rafanelli, P. 2012, MNRAS, 427, 1266

Véron-Cetty, M.-P., Véron, P., & Gonçalves, A. C. 2001, A&A, 372, 730

Vestergaard, M., Wilkes, B. J., & Barthel, P. D. 2000, ApJ, 538, L103

Wadadekar, Y. 2004, A&A, 416, 35

Wagner, A. Y., & Bicknell, G. V. 2011, ApJ, 728, 29

Wagner, A. Y., Bicknell, G. V., & Umemura, M. 2012, ApJ, 757, 136

Walker, R. C., Benson, J. M., & Unwin, S. C. 1987, ApJ, 316, 546

Wall, J. V., & Peacock, J. A. 1985, MNRAS, 216, 173

Wang, J.-M., & Zhang, E.-P. 2007, ApJ, 660, 1072

Wang, T., Brinkmann, W., & Bergeron, J. 1996, A&A, 309, 81

Whalen, D. J., Laurent-Muehleisen, S. A., Moran, E. C., & Becker, R. H. 2006, AJ, 131, 1948

Whittle, M. 1985, MNRAS, 213, 1

Wills, B. J., & Browne, I. W. A. 1986, ApJ, 302, 56

Woltjer, L. 1959, ApJ, 130, 38

Wu, Q. 2009a, ApJ, 701, L95

—. 2009b, MNRAS, 398, 1905

Xiao, T., Barth, A. J., Greene, J. E., Ho, L. C., Bentz, M. C., Ludwig, R. R., & Jiang, Y. 2011, ApJ, 739, 28

Yao, S., Yuan, W., Zhou, H., Komossa, S., Zhang, J., Qiao, E., & Liu, B. 2015, MNRAS, 454, L16

Yuan, W., Zhou, H. Y., Komossa, S., Dong, X. B., Wang, T. G., Lu, H. L., & Bai, J. M. 2008, ApJ, 685, 801

Zamanov, R., Marziani, P., Sulentic, J. W., Calvani, M., Dultzin-Hacyan, D., & Bachev, R. 2002, ApJ, 576, L9

Zel'dovich, Y. B. 1964, Soviet Physics Doklady, 9, 195

Zhou, H., Wang, T., Yuan, W., Lu, H., Dong, X., Wang, J., & Lu, Y. 2006, ApJS, 166, 128

Zhou, H.-Y., & Wang, T.-G. 2002, Ch.J. A&A, 2, 501

Appendix

In this appendix I show the spectra of the sources studied in this thesis which I observed with the Asiago 1.22m telescope. The sole UGC 3478 was observed with Telescopio Nazionale Galileo.